Finite Element Modelling of Ultra-High Performance Fibre Reinforced Concrete

by

Zhongyue Zhang

A thesis submitted in conformity with the requirements
for the degree of Master of Applied Science

Graduate Department of Civil & Mineral Engineering
University of Toronto

Finite Element Modelling of Ultra-High Performance Fibre Reinforced Concrete

Zhongyue Zhang

Master of Applied Science
Graduate Department of Civil & Mining Engineering
University of Toronto

2020

Abstract

Ultra-high performance fibre reinforced concrete (UHPFRC) is a relatively new material showing increased use for practical engineering problems. Although significant research has been undertaken in the development of constitutive models for the finite element modelling of steel fibre reinforced concrete (SFRC), the reliability of these models in analyzing UHPFRC remains unassessed. This thesis outlines the investigation of these models in finite element software VecTor2 for their applicability in analyzing UHPFRC. Localized behaviour at cracks was investigated, leading to improvements in current crack spacing formulations through the inclusion of an effective aggregate size for UHPFRC. An embedded steel reinforcement rupture formulation for specimens subjected to tension was also implemented to predict reinforcement rupture strains of reinforced concrete specimens. Finally, studies were conducted to validate these models for structures subjected to various loading effects by comparing the finite element simulations with experimental results found in the literature.

Acknowledgements

Contents

List of Tables

List of Figures

Chapter 1

Introduction

1.1 Background and Motivation

Ultra-high performance fibre reinforced concrete (UHPFRC) is a new generation of cementitious composite with superior mechanical properties. With compressive strengths in excess of 200 MPa and advanced durability characteristics, this material lends itself to innovative and efficient solutions to many practical design problems. For example, its low permeability characteristic results in the ability to resist aggressive environments, an essential property for the rehabilitation of deteriorating structures. Other advantages of UHPFRC include increased speed of construction, improved aesthetics, and impermeability to corrosion. The first structural application of UHPFRC was in the construction of the Sherbrooke footbridge in 1997 in Quebec, Canada. In 2002, the first fully UHPFRC footbridge in the world spanning 120 m was constructed in Seoul, South Korea. Subsequently, in the United States in 2006, the Mars Hill Bridge in Wapello County, Iowa, was the first highway transportation bridge constructed entirely of UHPFRC. Since then, UHPFRC has been considered worldwide in numerous other applications, particularly in high-performance structures such as bridges and blast or impact-resistant structures.

(a) Sherbrooke pedestrian bridge, QC, Canada.   (b) Mars Hill bridge, Wapello County, Iowa.

Figure 1.1: Applications of UHPFRC.

Although applications of UHPFRC have been successfully demonstrated in several countries, widespread use is still limited. Several obstacles are known, including the lack of understanding of its mechanical properties as well as the absence of proven analysis methods and unified design procedures. For example, design guidelines for UHPFRC are available in several countries,

including Canada, Germany, Switzerland, Spain, Australia and Japan. However, each of these guidelines approaches the design process differently and has different requirements for material characterization (Larsen and Thorstensen, 2020). In addition, there is especially limited knowledge on the development of rational constitutive models and a lack of easily employed finite element models for predicting UHPFRC flexural and shear behaviour. As such, this research program aims to investigate constitutive models in the finite element analysis program VecTor2 and provide a reliable analytical tool for the safe design of UHPFRC structures.

VecTor2 is a nonlinear finite element analysis program developed at the University of Toronto for the analysis of two-dimensional membrane structures (Vecchio, 1990). The program combines a variety of nonlinear constitutive models with the analytical capabilities of finite element analysis to model the response of various materials, such as concrete, fibre reinforced concrete, and masonry. For reinforced concrete elements subjected to in-plane stresses, VecTor2 calculates the response using a smeared, rotating crack formulation based on the Modified Compression Field Theory (MCFT) (Vecchio and Collins, 1986) and the Disturbed Stress Field Model (DSFM) (Vecchio, 2000). The program uses a total load iterative procedure based on a secant stiffness formulation, allowing for numerically robust and stable performance with good convergence characteristics.

1.2 Project Objectives and Research Significance

Much research has been undertaken in the development of constitutive models for conventional reinforced concrete (RC) and steel fibre reinforced concrete (SFRC). However, the reliability of these models in analyzing UHPFRC remains unassessed. As such, the main objective of this research project is to assess and modify where necessary existing finite element analysis models in VecTor2 to extend and improve its capabilities in modelling and analyzing UHPFRC members.

Using data from five large-scale UHPFRC pure shear tests previously conducted at the University of Toronto (Yap, 2020), a finite element model was developed for the analysis of UHPFRC shear-critical elements. Although UHPFRC exhibits different mechanical behaviour from both RC and FRC, existing constitutive models in VecTor2 for these materials are compared and investigated for their applicability in modelling UHPFRC. Localized behaviour at cracks is also investigated, resulting in improvements to current crack width formulations. In addition, a steel reinforcement rupture model is formulated to capture the potential for reinforcement rupture in highly ductile members, characteristic of UHPFRC structures. Finally, validations studies using

experimental results found in the literature are conducted to verify these models and recommendations to modelling techniques are given.

The development of an accurate finite element model and a corresponding modelling technique will provide valuable insight into UHPFRC behaviour when large full-scale experimental tests are costly and time-consuming. In addition, the improvements and modifications made through this research project can contribute to the development of improved design methodologies for the safe and efficient design of UHPFRC.

1.3   Thesis Outline

This section summarizes the content of this thesis and outlines the order in which they are presented.

Chapter 2 provides a summary of relevant literature and background information required for this thesis. A review of basic mechanical properties and previous experimental tests conducted on UHPFRC is presented. Current constitutive models used for SFRC, as well as available finite element modelling methods for UHPFRC are discussed. A summary of relevant research on reinforcement rupture in reinforced concrete and other various high-performance concrete is also presented.

Chapter 3 provides the preliminary studies conducted to determine the parameters affecting UHPFRC modelled behaviour in VecTor2.

Chapter 4 summarizes the various improvements and modifications made to current aggregate modelling, tension softening, and crack width formulations in VecTor2. This chapter also verifies the accuracy of the implemented fibre reinforced concrete models.

Chapter 5 presents a new reinforcement rupture model implemented in VecTor2.

Chapter 6 provides the verification studies conducted for the implemented modifications using experimental programs of SFRC and UHPFRC found in the literature.

Lastly, Chapter 7 presents the main conclusions drawn from the analytical studies. Recommendations for future investigations are also presented.

Chapter 2

Literature Review

2.1 Ultra-High Performance Fibre Reinforced Concrete

In the 1990s, ultra-high performance fibre reinforced concrete (UHPFRC), originally known as reactive powder concrete, was first developed as a result of the quest to further increase the mechanical strength of concrete. This highly homogeneous cementitious composite is characterized by high Portland cement content, small aggregate sizes, and low water-to-cement ratios. These characteristics produce a dense, smooth matrix, resulting in a material with enhanced performance, durability, strength, and toughness compared to normal and high strength concrete. It was well established that the use of small, discrete fibres as reinforcement for brittle materials significantly improves the ductility and tensile strength of concrete. Thus, ultra-high performance concrete generally contains a high dosage of steel fibres to achieve ductile behaviour.

In general, fibre reinforced concrete can be classified according to the characteristic of its stress-strain response in tension. The properties of the cementitious matrix dominate the behaviour up to cracking. As shown in Figure 2.1, after cracking, fibres bridging the cracks engage and begin to carry load, resulting in either a strain-softening or strain-hardening behaviour (Naaman, 2008). In strain-softening materials, the tensile response is characterized by localization immediately after cracking; increasing elongation after the cracking strength of the material is reached immediately results in the gradual reduction of tensile stress to zero. In contrast, the high fibre dosage in UHPFRC combined with its enhanced mechanical properties often results in a strain-hardening response. The stress continues to increase after cracking through the formation of finely distributed micro-cracks. The fibres prevent the propagation of these micro-cracks by absorbing tensile stresses, resulting in a ductile post-cracking behaviour. Localization occurs at the maximum post-cracking stress when the fibres bridging any individual crack pull out. After localization, the material behaves like the strain-softening material as a result of gradual fibre debonding.
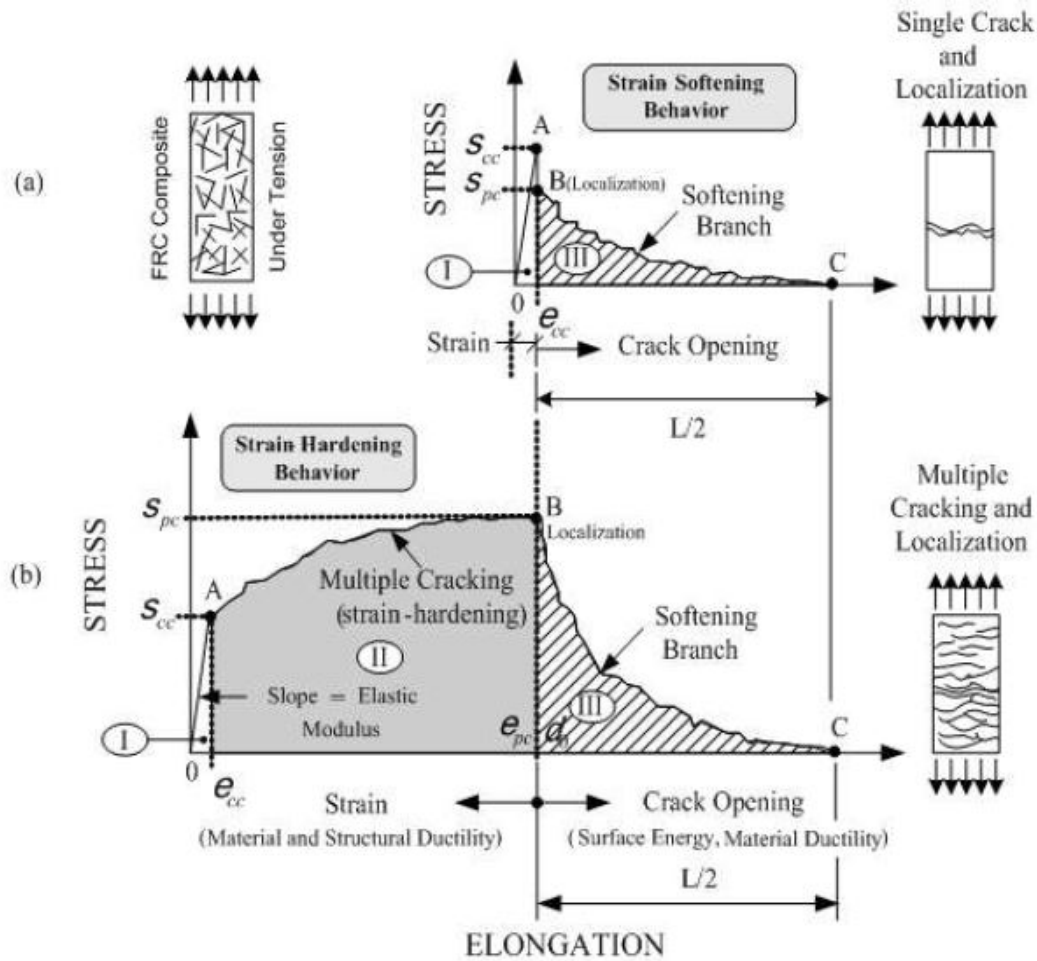
Figure 2.1: Typical tensile behaviour of fibre reinforced composites: (a) strain-softening behaviour and (b) strain-hardening behaviour (Naaman, 2008).

Its strength and durability characteristics make UHPFRC advantageous in a variety of high-performance applications, such as offshore platforms and nuclear power structures, precast elements, components exposed to marine or aggressive environments, and as strengthening material for rehabilitation of deteriorated reinforced concrete structures. For example, it can be applied as concrete cover for bridge superstructure elements subjected to severe environmental and mechanical loads, serving as a waterproofing and protective layer to allow for reduced maintenance costs and a longer structural life span. Its strength characteristics and enhanced mechanical properties permit the use of smaller and lighter section sizes and thus, lending itself to innovative, efficient, and more economical design solutions. In addition, its enhanced strength and energy absorption capacity, and strain-hardening properties makes it a promising material for blast and impact resistant structures.

2.2   Recent Experimental Investigations

Since its introduction, the superior mechanical properties of UHPFRC have caught the attention of many researchers, government bodies, and structural designers. It has been determined that the mechanical properties of UHPFRC are influenced by a wide range of parameters such as curing conditions, packing density, and the characteristics of the added steel fibres. For example, the use of deformed fibres, such as end-hooked and twisted steel fibres, generally increases the tensile strength, strain capacity, and flexural strength of members. As such, continual research is required to understand the behaviour patterns of UHPFRC fully. To date, research programs have investigated UHPFRC under a variety of loading conditions, including static, impact, and blast. The following section summarizes the experimental programs along with their findings. These experimental investigations are critical to the development and verification of finite element models for the analysis of UHPFRC members.

Talleen et al. (2010)

Telleen et al. (2010) tested two I-shaped UHPFRC beams under three-point bending to characterize the shear behaviour and evaluate the effects of transverse reinforcement in UHPFRC. Both beams had identical properties except that one beam contained transverse reinforcement spaced at 150 mm in the web while the other did not. Both beams contained 3.0% by volume of 13 mm long, 0.16 mm diameter straight steel fibres. The tensile strength of the fibres was not reported. The web of the I-girders was 20 mm thick and in such thin elements, fibres will tend to orientate themselves parallel to the plane of the flange or web. Figure 2.2 shows the beam cross-sectional dimensions and reinforcement configuration. As shown in Figure 2.3, the beams were loaded in monotonically increasing deflection at midspan up to failure.

(a) Elevation view. (b) Cross section view.

Figure 2.2: Dimensions and Reinforcement configuration for beams tested by Telleen et al. (2010).
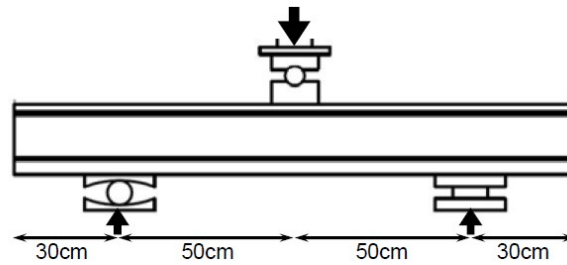
Figure 2.3: Loading condition for beams tested by Telleen et al. (2010).

The experimental results indicated that both beams exhibited primarily diagonal cracking in the web, characteristic of shear failure. Figure 2.4 shows the load-deflection curves for the two beams tested. This experimental program concluded that the addition of transverse reinforcement in the web of UHPFRC I-beams significantly improved both the shear and ductility capacity of the member.
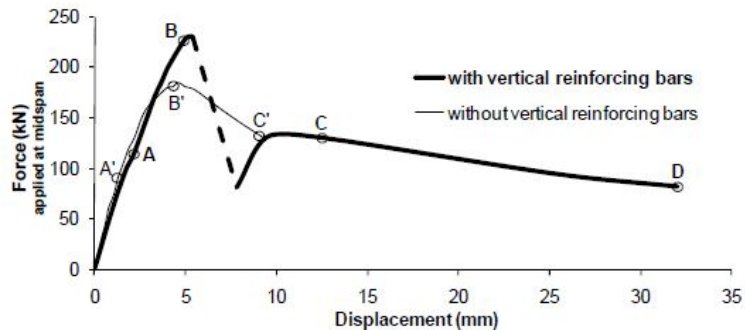
Figure 2.4: Load-deflection response for beams tested by Telleen et al. (2010).

From the experimental results, a simplified expression was developed to estimate the shear strength

of UHPFRC. This expression expressed the shear strength as a sum of the shear contribution from transverse bars and fibres. However, this model presented an oversimplification of the shear behaviour as it contained many assumptions. For example, the crack angle and tensile strength used in the model were assumed to be 45 degrees and 16 MPa, respectively. In reality, both of these values vary and are dependent on a variety of different factors. This expression also did not factor in the effect of fibre properties on shear strength and ductility. Thus, the authors recommended further testings to validate and enhance the model.

Yang et al. (2010)

Yang et al. (2010) studied the effect of longitudinal reinforcement ratio on the flexural behaviour of UHPFRC rectangular beams. Two sets of seven beams were tested under four-point bending to determine the post-cracking behaviour. All beam specimens had identical dimensions with a width of 180 mm, height of 270 mm, and length of 2900 mm. The beams contained one specimen without reinforcement (NR) and other specimens with varying reinforcement ratios and layouts. The longitudinal reinforcement had a nominal diameter of 13 mm (D13). The yield and ultimate strength of the longitudinal reinforcement were not reported. The specimens contained 2.0% by volume of 0.2 mm diameter, 13 mm long straight steel fibres. The fibres had a density of 7500 kg/m^3 and a tensile strength of 2500 MPa. Details of the cross section and reinforcement arrangement are shown in Figure 2.5.
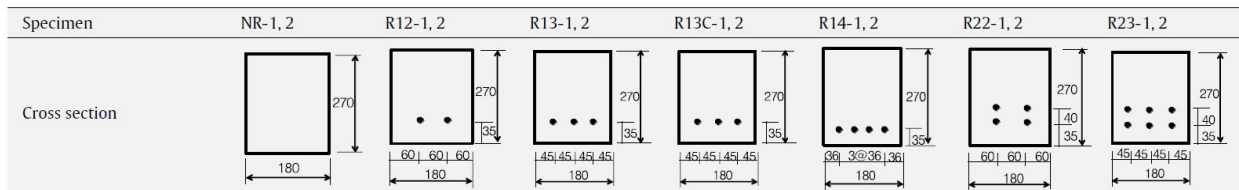
Figure 2.5: Cross-sectional dimensions and reinforcement configuration for beams tested by Yang et al. (2010).

The effect of two different concrete placement methods was also investigated. All beams except for R13C had concrete cast at one end and allowed to flow to the other end. Concrete for Beam 13C was placed midspan and allowed to flow to both ends. Beams R13 and R13C were identical to each other except for the placement method.

During testing, cracking, failure pattern, deflection, ductility and flexural capacity were measured for the beams. The load-deflection curves of the experimental results are shown in Figure 2.6. All beams experienced flexural failure, precipitated by local bond failure between the fibres and the

UHPC matrix, and by reinforcement yielding. The results indicated that UHPFRC can redistribute stresses through multiple cracks forming prior to fibre pullout. In addition, the test results showed that the addition of fibres enhanced the post-cracking ductility of the members. The authors recommended further testing to determine the influence of fibre content and fibre properties on ductility.
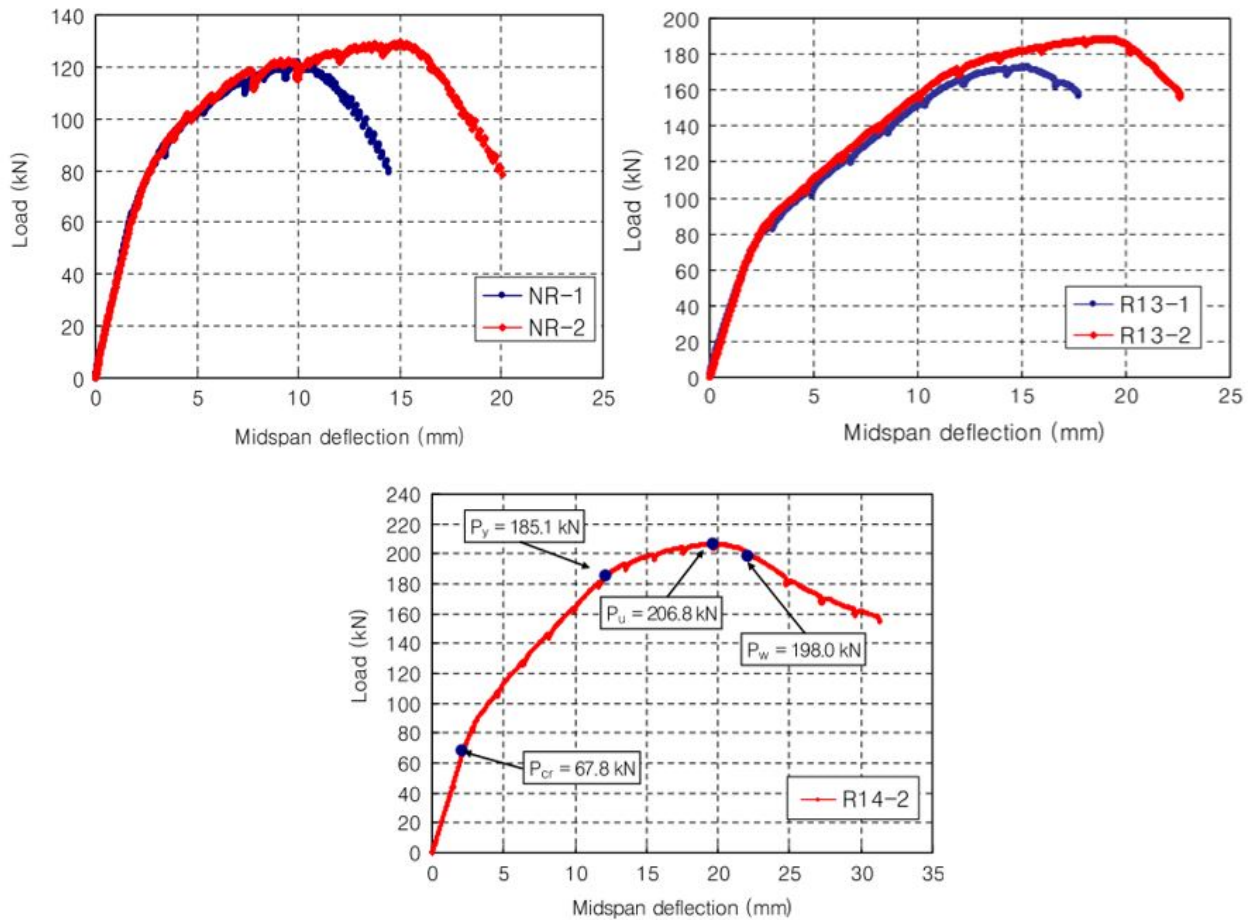
Figure 2.6: Load-deflection response for beams tested by Yang et al. (2010).

Voo et al. (2010)

Voo et al. (2010) tested eight prestressed UHPFRC beams to determine the effect of shear span-to-depth (a/d) ratio and steel fibre properties on shear behaviour. All beams were 8600 mm in length, 650 mm deep, and had a web thickness of 50 mm. The top and bottom flanges were both 500 mm wide and contained six 15.2 mm diameter high strength steel prestressing strands. Figure 2.7 shows the cross section geometry and prestressing strand configuration for the specimens. Figure 2.8 shows the different beam loading conditions.
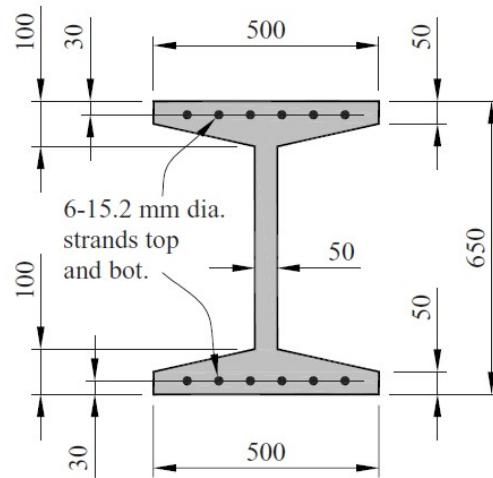
Figure 2.7: Cross section and reinforcement configuration for beams tested by Voo et al. (2010).
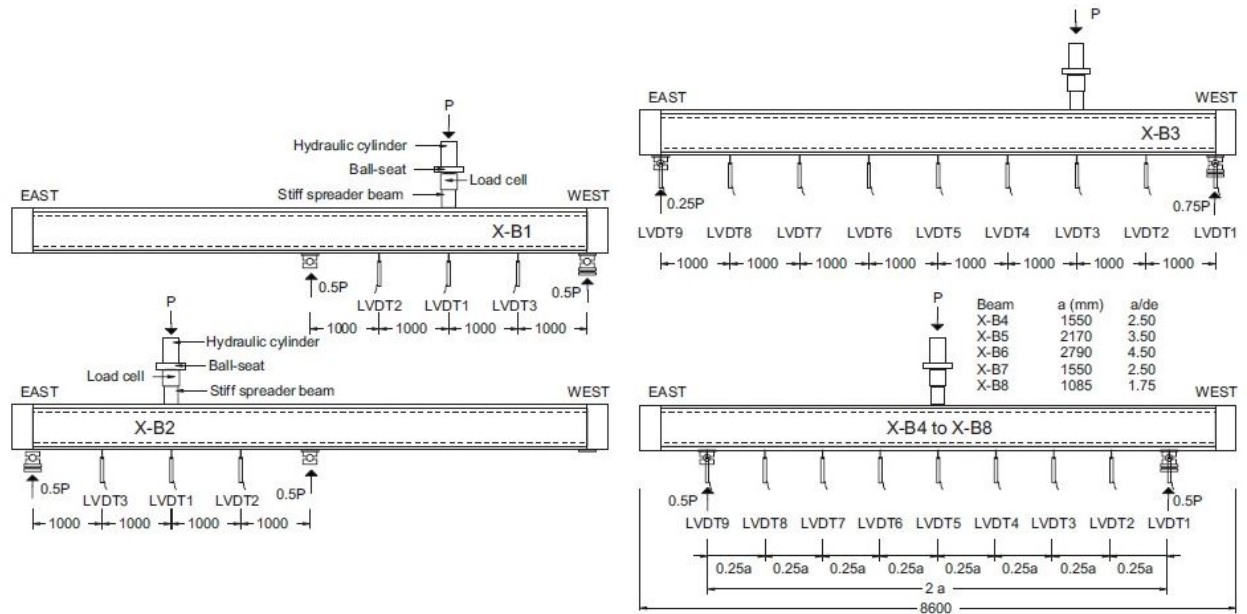
Figure 2.8: Loading conditions for beams tested by Voo et al. (2010).

The beams contained either 1.0% or 1.5% by volume of 0.2 mm diameter steel fibres. The lengths of the fibres were 15 mm, 20 mm, or 25 mm long. The fibres had a tensile strength of 2300 MPa. Two beams (X-B1 and X-B2) were air cured only while the other six were heat-treated at 90 degrees Celsius.

The shear force-deflection responses are shown in Figure 2.9. The results showed significant distribution of shear cracks in the web prior to the formation of a dominate failure crack, characteristic of strain-hardening materials.
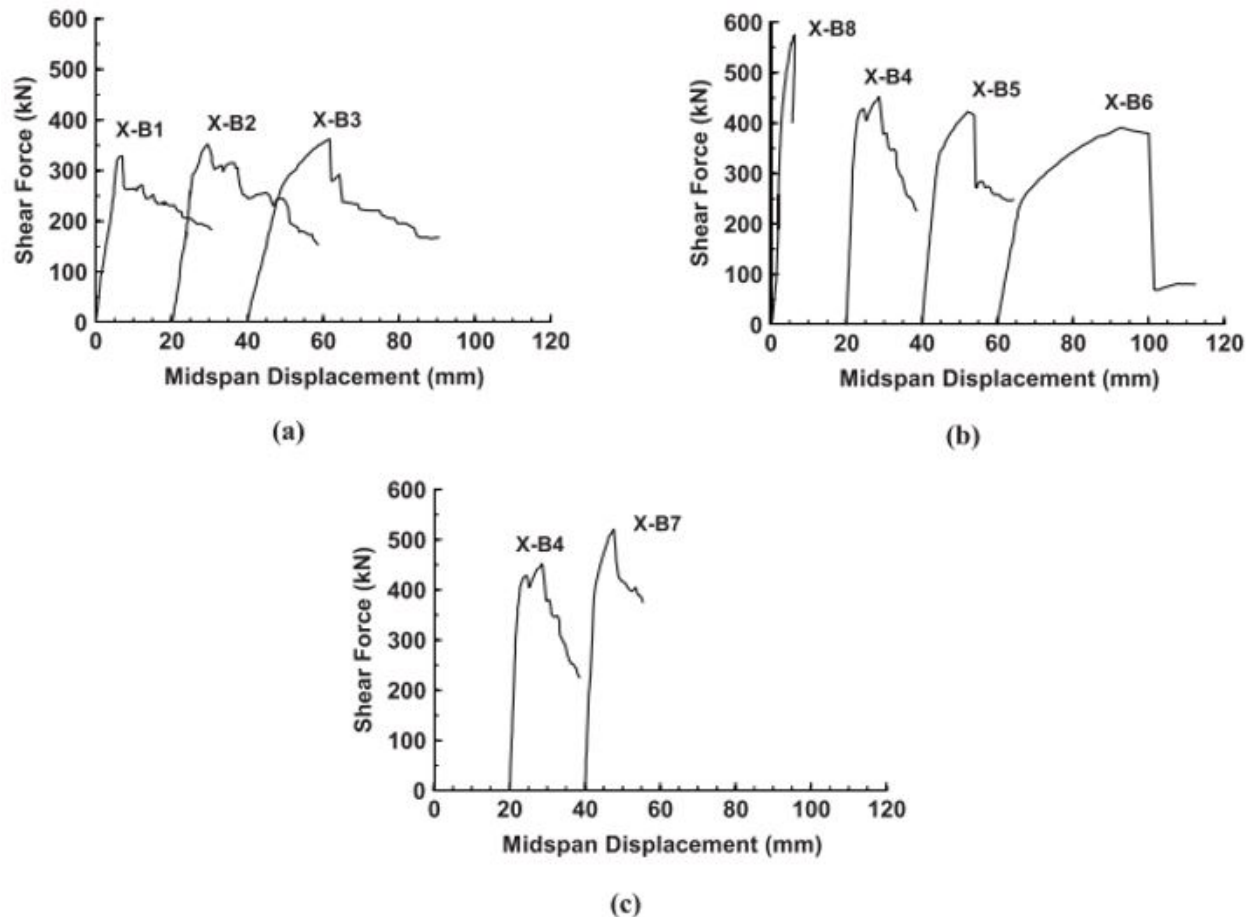
Figure 2.9: Shear load-deflection response for beams with (a) constant a/d ratio and fibre content; (b) constant fibre content and increasing a/d ratio; and (c) constant a/d and varying fibre content tested by Voo et al. (2010).

Yoo and Yoon (2015)

Yoo and Yoon (2015) investigated the flexural response of UHPFRC beams with different steel fibres by preparing and testing ten rectangular beams under four-point bending. All beam specimens had identical dimensions with a width of 150 mm, height of 220 mm, and length of 2500 mm. Five beams were reinforced with two 12.7 mm (D13) tension longitudinal reinforcement while the other five beams were reinforced with two 15.9 mm (D16) longitudinal bars, leading to two different reinforcement ratios (ρ=0.94% and ρ=1.50%). The D13 reinforcement had a yield strength of 495 MPa while the D16 reinforcement had a yield strength of 510 MPa. Shear reinforcement was also provided to ensure a flexural failure mode for all test specimens. The shear reinforcement consists of 9.53 mm closed stirrups with a yield strength of 491 mm at a spacing of 80 mm. Details of the cross section dimensions and reinforcement arrangement are shown in Figure 2.10a.The loads were applied monotonically in small increments (10 or 20 kN interval) under a static four-point loading

method, as shown in Figure 2.10b.

(a) Cross section view.   (b) Elevation view and loading condition.
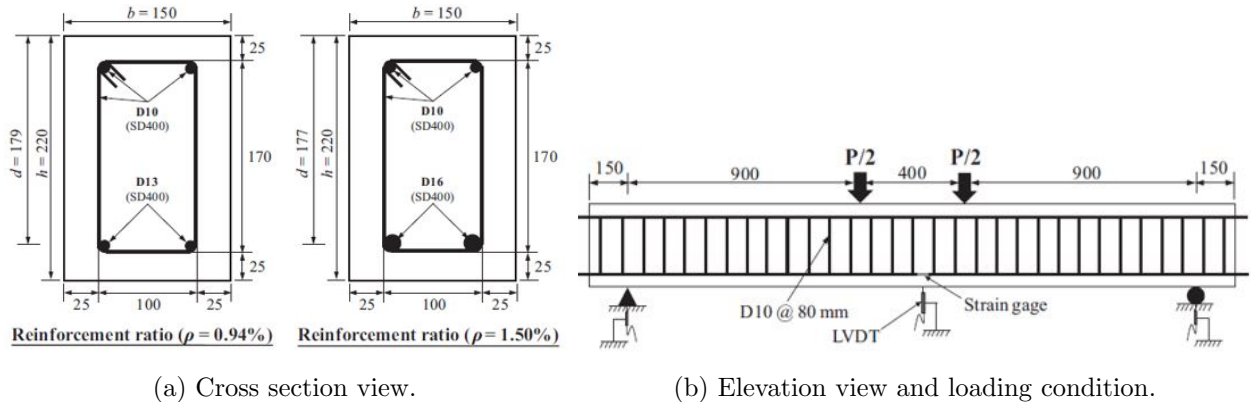
Figure 2.10: Dimensions, reinforcement configurations, and loading condition for beams tested by Yoo and Yoon (2015).

The load-deflection curves of the experimental results are shown in Figure 2.11. The authors concluded that increasing the reinforcement ratio increased the flexural load capacity of the beams. The length and type of fibre did not affect the load-carrying capacity or post-cracking stiffness. The results from the experiments were then used to validate the numerical results from a sectional analysis.
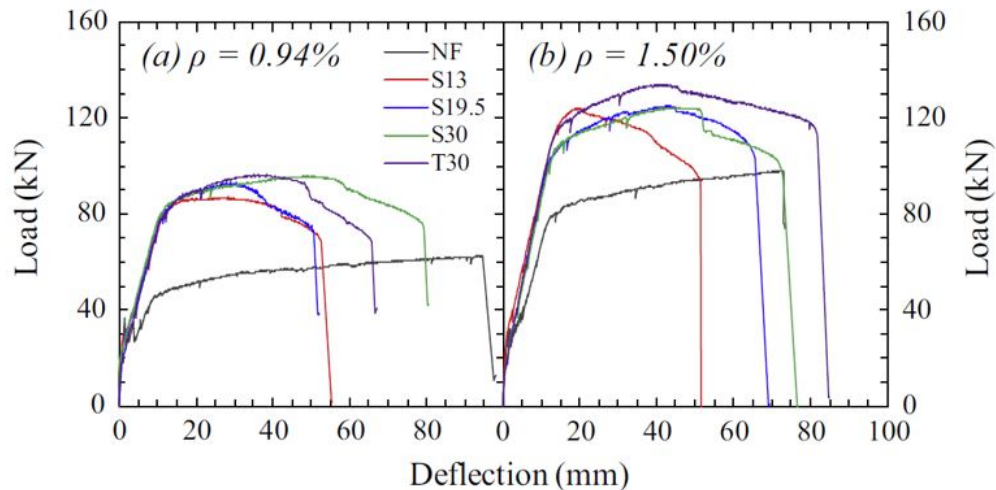
Figure 2.11: Load-deflection response for beams tested by Yoo and Yoon (2015).

Yoo et al. (2016)

Yoo et al. (2016a) also studied the effect of reinforcement ratio on the flexural behaviour of UHPFRC beams. Four UHPFRC beams with different reinforcement ratios (0-1.71%) were fabricated and tested under static four-point bending. The dimensions of the specimens were a width of 200 mm,

height of 270 mm, and length of 2900 mm. The longitudinal reinforcement used varied in ratios and placement locations, but all had a nominal diameter of 12.7 mm (D13) with a yield strength of 522.7 MPa and ultimate strength of 627.6 MPa. The specimens contained a fixed 2.0% by volume of 0.2 mm diameter, 13 mm long straight steel fibres. The fibres had a density of 7800 kg/m^3 and a tensile strength of 2500 MPa. Details of the cross-sectional dimensions and reinforcement arrangement are shown in Figure 2.12a. The loads were applied monotonically in small increments (20 kN intervals), as shown in Figure 2.12b.
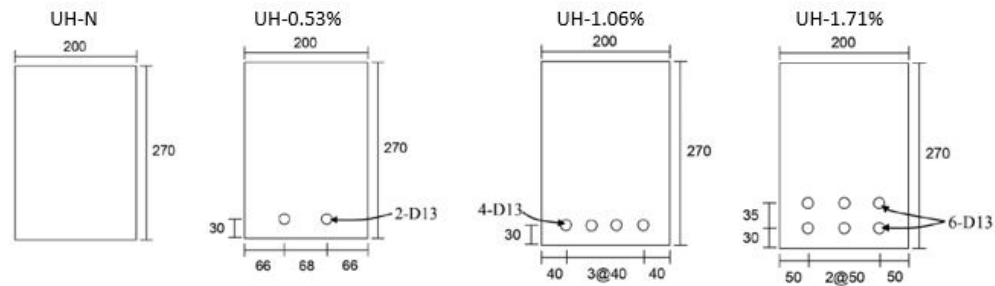
(a) Cross section view.
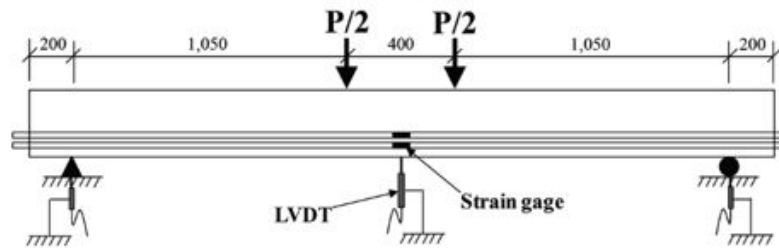
(b) Loading conditions.

Figure 2.12: Dimensions, reinforcement configuration, and loading conditions for beams tested by Yoo et al. (2016a).

The results indicated that an increase in reinforcement ratio produced an increase in post-cracking stiffness and strength capacity and a decrease in cracking strength. Figure 2.13 shows the load-deflection curves of the experimental results.
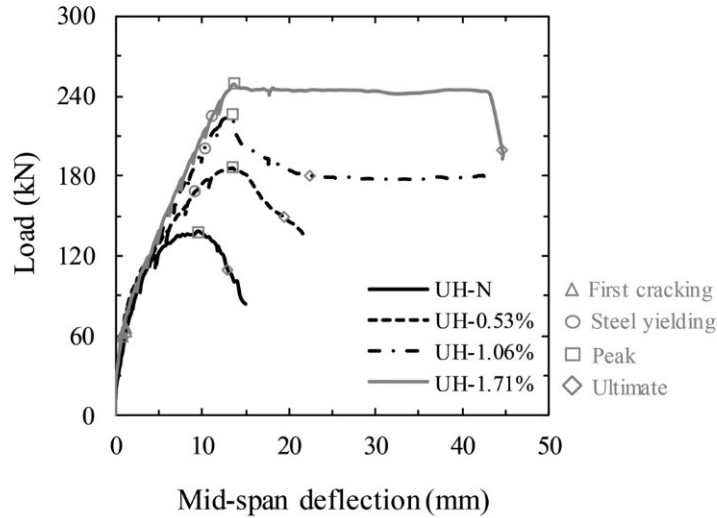
Figure 2.13: Load-deflection response for beams tested by Yoo et al. (2016a).

Kodur et al. (2018)

Kodur et al. (2018) tested UHPFRC beams containing coarse aggregates under flexural and shear loading. Four large-scale beams were fabricated using a new mix design containing coarse aggregate. Two large-scale beams with different reinforcement ratios were tested under flexural four-point bending, and two similar beams were tested under shear dominant loading. All four beams contained shear and compression reinforcement. All four beams had identical dimensions with a width of 180 mm, height of 270 mm, and length of 4000 mm. The longitudinal reinforcement used varied in ratios and placement but all had a nominal diameter of 12.7 mm (D13) with yield strength of 435 MPa and ultimate strength of 700 MPa. Details of the cross section dimensions and reinforcement arrangement are shown in Figure 2.14a. The loading conditions are shown in Figure 2.14b. Beams U-B3 and U-B5 were tested under pure bending and subjected to two point loads on the top face of the beam at a distance of 432 mm on either side of the midspan. Beams U-B4 and U-B6 were tested under shear and subjected to a single point load applied on the top face of the beams at a distance of 610 mm from the support.
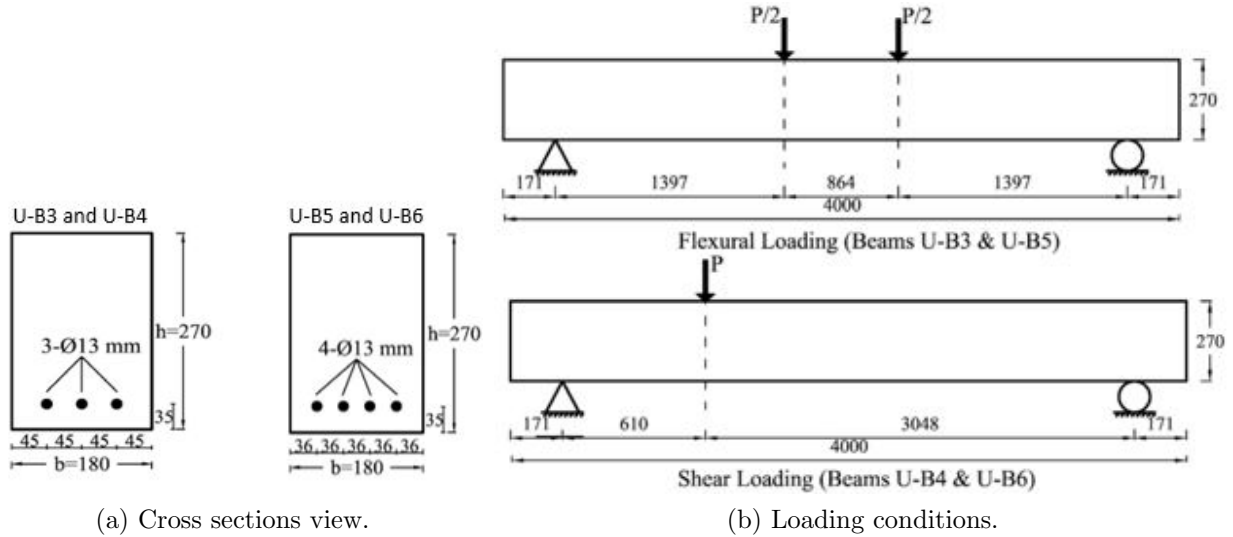
(a) Cross sections view. (b) Loading conditions.

Figure 2.14: Dimensions, reinforcement configuration, and loading conditions for beams tested by Kodur et al. (2018).

Figure 2.15 shows the experimental load-deflection response of the tested beams. All beams exhibited four distinct response stages: a linear elastic state until the first tensile crack in state OA, a post-cracking state with crack progression in zone AB until steel yielding at point B, plastic deformation in zone BC, post-peak response in zone CD, followed by failure at point D. This experimental program further confirmed the tendency for UHPFRC to form multiple microcracks, followed by the propagation of a single, dominant crack. The authors concluded that UHPFRC could attain 10-20% increase in load carry capacity after yielding of the longitudinal reinforcement as a result of the strain-hardening effect. In addition, the authors speculated that due to the high shear stiffness of UHPFRC, shear deformations were negligible and did not affect the overall deflection response.
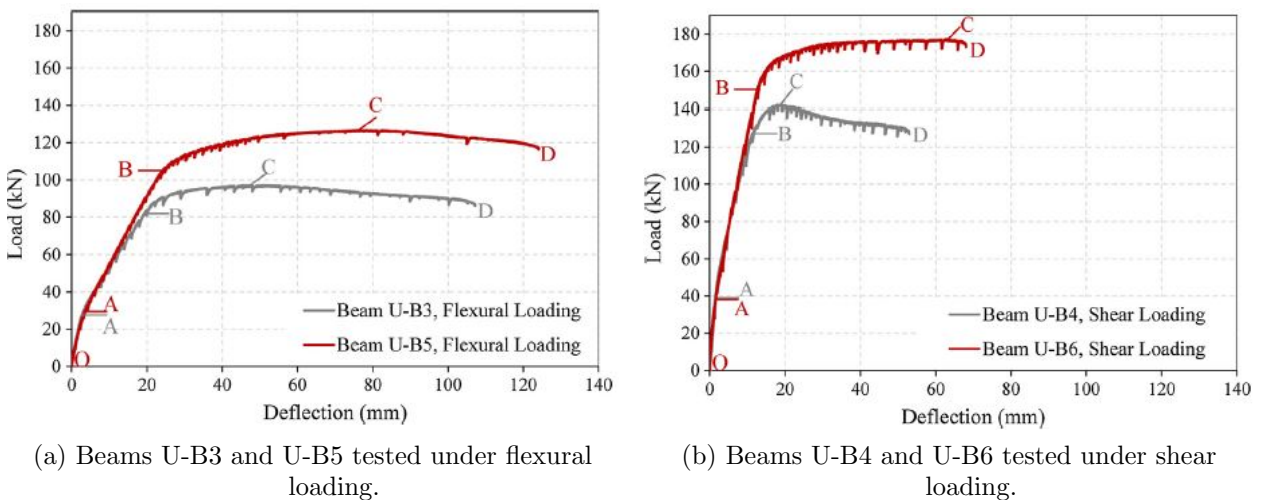
(a) Beams U-B3 and U-B5 tested under flexural loading. (b) Beams U-B4 and U-B6 tested under shear loading.

Figure 2.15: Load-deflection response for beams tested by Kodur et al. (2018).

Singh et al. (2017)

Singh et al. (2017) performed full-scale bending tests on four simply supported beams under different loading conditions. Members B25-1 and B25-2 contained 3-20 mm longitudinal tensile reinforcement with a nominal yield strength of 525 MPa and an ultimate strength of 625 MPa. Members B15-1 and B15-2 contains 2-16 mm tensile reinforcement with a nominal yield strength of 720 MPa and an ultimate strength of 705 MPa. The specimens also contained shear reinforcements consisting of 10 mm or 6 mm diameter stirrups at 90 mm spacing. The cross-sectional dimensions and reinforcement configurations are shown in Figure 2.16. The loading conditions are shown in Figure 2.17.
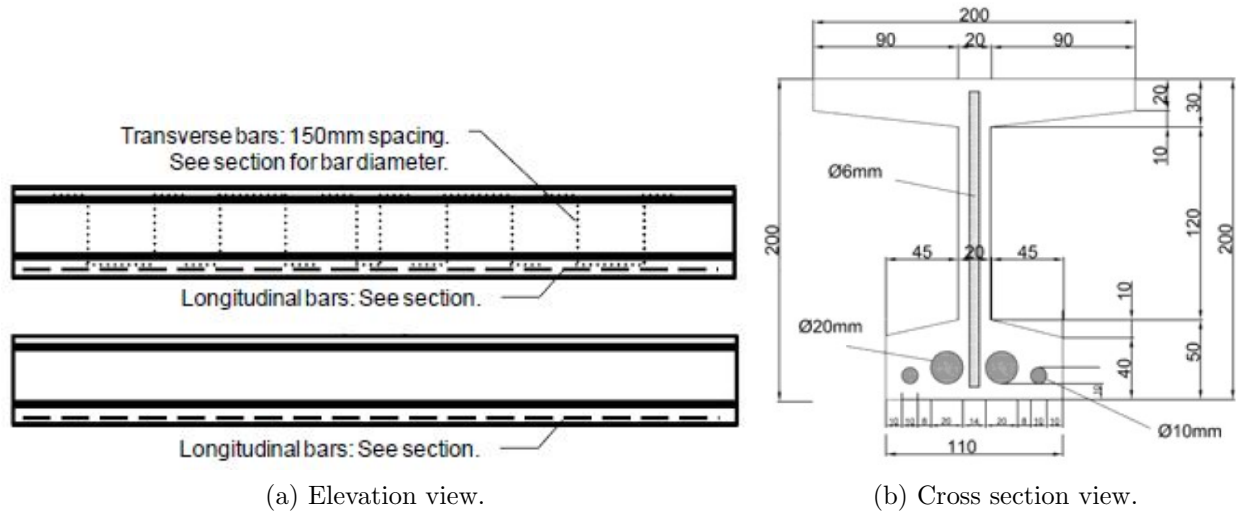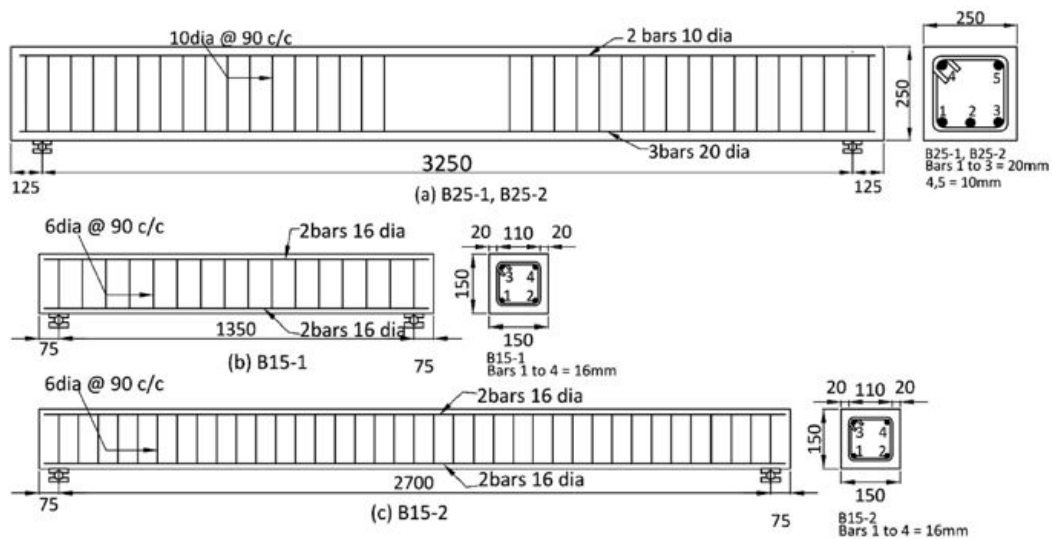

Figure 2.16: Cross sections and reinforcement configuration for beams tested by Singh et al. (2017).
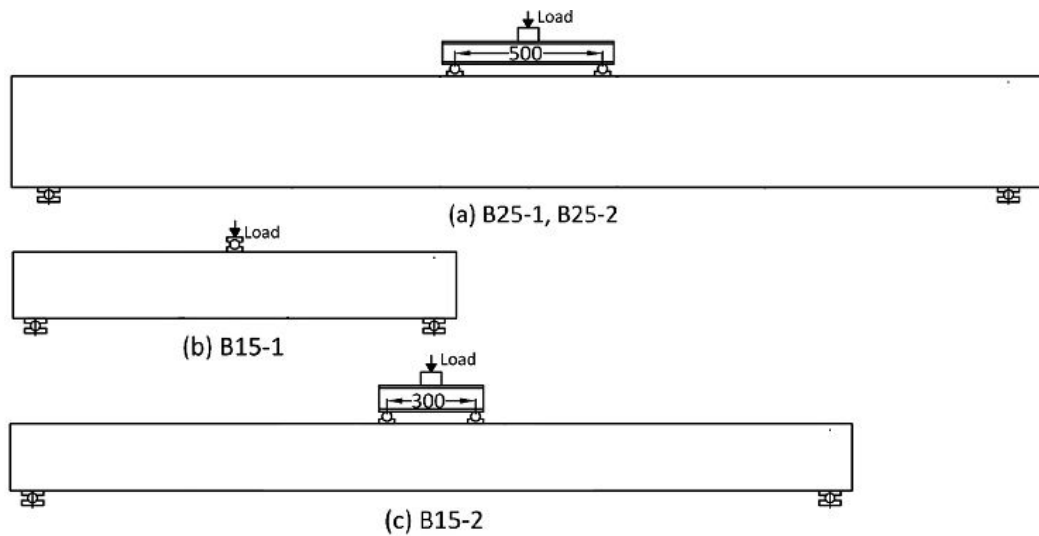
Figure 2.17: Loading conditions for beams tested by Singh et al. (2017).

The load-deflection curves of the experimental results are shown in Figure 2.18. The experimental results were used to validate the development of a finite element model discussed in Section 2.4.
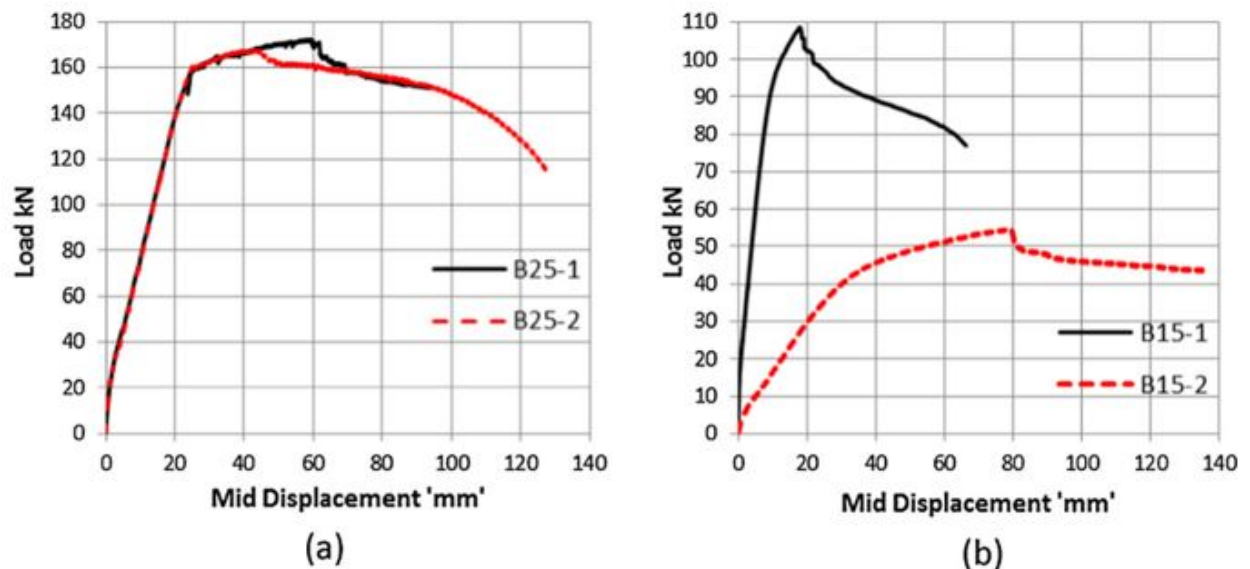
Figure 2.18: Load-displacement curves for beams (a) B25-1 & B25-2; (b) B15-1 & B15-2 tested by Singh et al. (2017).

Yap (2020)

Yap (2020) tested five large-scale UHPFRC panel elements under monotonic pure shear to investigate the effect of reinforcement conditions on shear strength. All five panels had a nominal dimension of 1625 mm x 1625 mm and a thickness of 200 mm. All panels contained 1.0% in volume of end-hooked fibres and 1.0% straight fibres. Three panels contained conventional reinforcement in only one direction to investigate the effect of the shear demand on the crack on the shear strength. One panel also contained no conventional reinforcement to investigate the shear capacity of the matrix. The panels were loaded using the Shell Element Tester at the University of Toronto. Equal principal stresses were applied to the panels in the vertical and horizontal directions to create a pure shear stress state at an x-y coordinate system orientated 45° to the principal stresses. Figure 2.19a shows an example reinforcement configuration using Panel YS1, which contained conventional reinforcement in both the x- and y-directions. Figure 2.19b shows the loading condition with the Shell Element Tester.
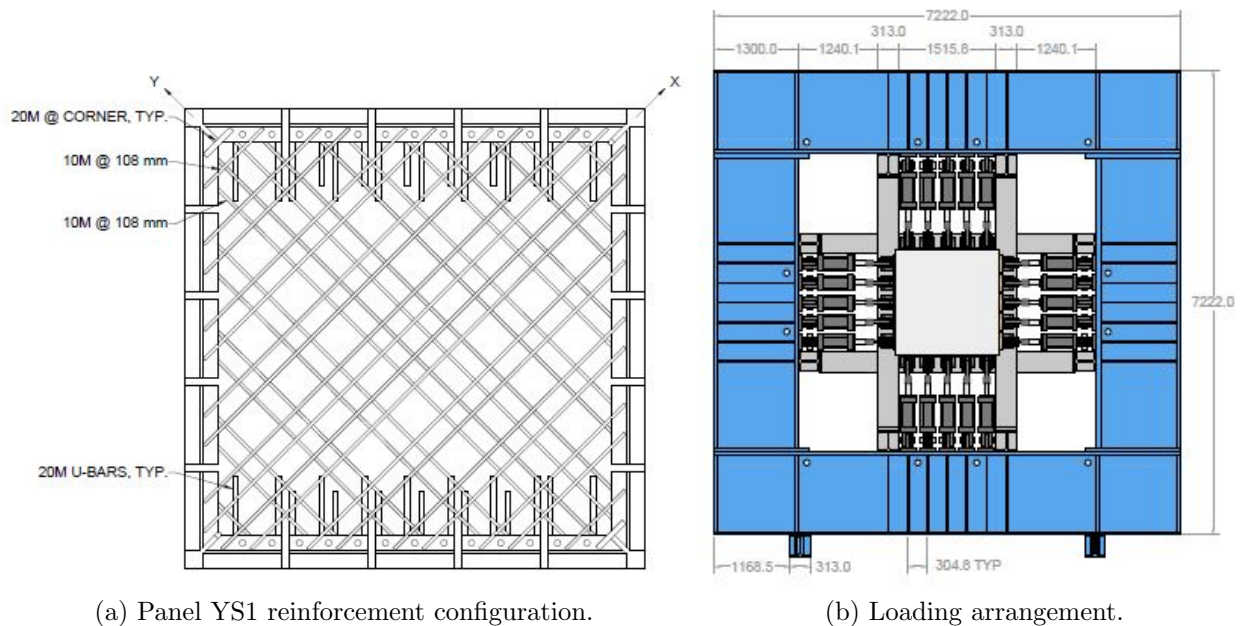
(a) Panel YS1 reinforcement configuration.　　　(b) Loading arrangement.
Figure 2.19: Reinforcement configuration and loading arrangement for panels tested by Yap (2020).

The experimental results indicated that UHPFRC has the potential to carry significant shear stress up to large strains. The addition of fibres has proven to add considerably to the tensile response of the panels and the tensile behaviour was significantly better than that of conventional reinforced concrete.

Using the experimental results, finite element models were also created using the Variable Engagement Model in finite element program VecTor2. It was concluded that these models require further development and validation to predict UHPFRC shear behaviour accurately.

2.3 Constitutive Models

Currently, limited research has been presented on the development of constitutive models specifically for ultra-high performance fibre reinforced concrete. However, several researchers have contributed to the development of constitutive models for steel fibre reinforced concrete, which can be adapted and extended to model UHPFRC. This section provides a summary of available constitutive models used to describe the behaviour of steel fibre reinforced concrete.

2.3.1 Marti et al., (1999)

Marti et al. (1999) first derived a simple relationship between the crack width and tensile stress of fibre reinforced concrete materials. By assuming constant bond stress, and that the number of fibres bridging a crack decreases linearly with increasing crack width, a parabolic relationship between crack width and tensile stress was developed. This model considered the effects of fibre length, diameter, and volumetric ratio of randomly oriented straight fibres on tensile stress. Pure fibre pullout was assumed to be on the side of the shorter embedment length, and the effect of fibre inclination was not considered.

2.3.2 Variable Engagement Model

The Variable Engagement Model (VEM) (Voo and Foster, 2003) describes the peak and post-peak behaviour of fibre reinforced concrete (FRC) composites subjected to uniaxial tension. This model's primary assumption is that the behaviour of a fibre reinforced composite can be expressed as a sum of the concrete contribution and fibre contribution. The effect of individual randomly orientated and discontinuous fibres can then be summed over 3D space to describe the overall behaviour of the composite. This was done by introducing a fibre engagement factor to consider the effect of fibre inclination on fibre pullout behaviour. The model was calibrated and validated against a wide range of data from FRC tests and obtained a good model-to-experimental correlation. Similar to Marti et al. (1999), however, this model assumed constant bond stress between the steel fibres and the concrete matrix. Moreover, it was assumed that fibre pullout occurred only on the shorter embedded length while the longer side remains rigidly embedded in the matrix. Thus, this model was not appropriate for FRC members containing end-hooked fibres.

2.3.3 Diverse Embedment Model

The Diverse Embedment Model (DEM) (Lee et al., 2011a) was later proposed to capture the tensile behaviour of FRC members with end-hooked fibres. Similar to the VEM, this model considers the randomness in fibre inclination angle and fibre embedment lengths. In contrast to the VEM, this model also considered the effect of unsymmetrical anchorage of end-hooked fibres on the constitutive relationship. The DEM separately evaluates the tensile stress due to frictional bond behaviour and the mechanical anchorage effects from the pullout behaviour of a single straight or end-hooked fibre. As a result, this model was more appropriate for modelling the tensile behaviour of fibre reinforced

concrete containing end-hooked fibres. The proposed model also allowed for the evaluation of tensile stresses developed in the fibres between cracks. The individual fibre stresses were used to derive the average tensile stresses at a crack. The model was validated against a wide range of test data performed by other researchers and obtained a good model-to-experimental correlation.

One advantage of the DEM is that this model uses a relatively limited number of input properties, which only requires performing a standard compression test. However, one disadvantage of the DEM is the requirement of double numerical integration for calculating the average tensile stress of the fibres at a crack. This often results in significant implementation difficulties for various finite element programs.

2.3.4 Simplified Diverse Embedment Model

The Simplified Diverse Embedment Model (SDEM) (Lee et al., 2013a) is a simplified version of the DEM for describing the FRC behaviour in tension. It eliminates numerical integration from the DEM, no longer considers the longer embedded side in the calculation of fibre tensile stress at a crack, and incorporates coefficients for frictional bond behaviour and mechanic anchorage effects to prevent overestimation of tensile stress attained by fibres. The SDEM first eliminated the double numerical integration by neglecting slip on the longer fibre embedded side, and assuming that the crack width is the same as the slip on the shorter embedded side. Two easily determined coefficients were introduced to consider the effect of fibre slip on the longer embedded side. Despite the simplifications, the model retained the accuracy of the DEM. (Lee et al., 2013a) showed that the SDEM could predict the behaviour of SFRC members with or without conventional reinforcement subjected to both uniaxial tension and flexure.

2.3.5 Reinforced Concrete Plasticity Models

Lastly, concrete plasticity models currently available in various commercial finite element software for the analysis of reinforced concrete have also been adapted to model SFRC behaviour. These include the Concrete Damage Plasticity (CDP) model available in ABAQUS and the concrete damage model available in LS-DYNA. Several researchers, such as Chen and Graybeal (2011a), Singh et al. (2017), and Yin et al. (2019), have successfully extended these models to predict the behaviour of UHPFRC members subjected to flexural loading.

The Concrete Damage Plasticity (CDP) model, available in finite element software ABAQUS, is

commonly used to model the behaviour of FRC and UHPFRC members. This model is based on the combination of damage mechanics and plasticity and provides a method of modelling the nonlinear behaviour of concrete and other quasi-brittle materials. Inelastic behaviour is represented by an internal scalar variable that characterizes damage in combination with the plasticity behaviour attributed to phenomenons such as strain-hardening and strain-softening, progressive deterioration, and volumetric expansion. The combination of these behaviours leads to a reduction of strength and stiffness of concrete. A disadvantage of the model is that the uniaxial behaviour in compression and tension of the material is required to evaluate its nonlinear response. Thus, the CDP model parameters often require precise calibration through experimental tests.

Similarly, the concrete damage model in LS-DYNA can be used to model UHPFRC behaviour. This model is a three-invariant plasticity model, where the failure surface is derived by interpolating between two of three independent strength surfaces using an internal damage function. Strain-hardening and strain-softening behaviours are modelled by internally scaling the hardening and softening variable using this damage function. Similar to the CDP model in ABAQUS, several parameters are required to express the model behaviour. These can be found through appropriate experimental tests or determined through the automatic parameter generation method within LS-DYNA.

2.4   Finite Element Modelling of UHPFRC

So far, finite element (FE) modelling for UHPFRC materials has been done in ABAQUS, LS-DYNA, and VecTor2 using methods and constitutive models discussed in the previous section.

Chen and Graybeal (2011a)

Chen and Graybeal (2011a) investigated the applicability of using the concrete damage plasticity model available in ABAQUS in modelling prestressed UHPFRC AASHTO Type II girders. Three-dimensional finite element models were created, assuming an elastic-perfectly plastic tensile stress-strain relationship. The inelastic behaviour was represented by isotropic damage combined with isotropic tensile and compressive plasticity. The formation of tensile micro-cracks in the concrete was represented by the softening stress-strain relationship. The various material properties required by the model, such as the maximum tensile stress and the ultimate plastic tensile strain in the concrete stiffening response, were obtained through calibrating the finite

element models to experimental results. The mesh sensitivity, tension stiffening response and compression hardening response, and the Young's modulus were also calibrated from a series of parametric studies using the experimental results. Another readily available concrete constitutive model, the concrete smeared cracking (CSC) model, was also investigated. It was determined that the CSC model predicted a stiffer response that significantly underestimated the tensile response, and was not appropriate for modelling these girders.

The models were validated against full scale testing of one Type II AASHTO I-girder in flexure and two shorter I-girders in shear. The results for the girder tested in flexure are shown in Figure 2.20. The finite element model of the beam in flexure replicated the experimental results for midspan deflection and strain responses of the girder in both the elastic and plastic regions. The finite element model of the girders in shear also produced similar results to the experiment. Chen and Graybeal (2011a) concluded that the CDP model could replicate the observed deflection and strain responses in the three full-scale I-girder tests and was consistent regardless of span lengths under flexure or shear.
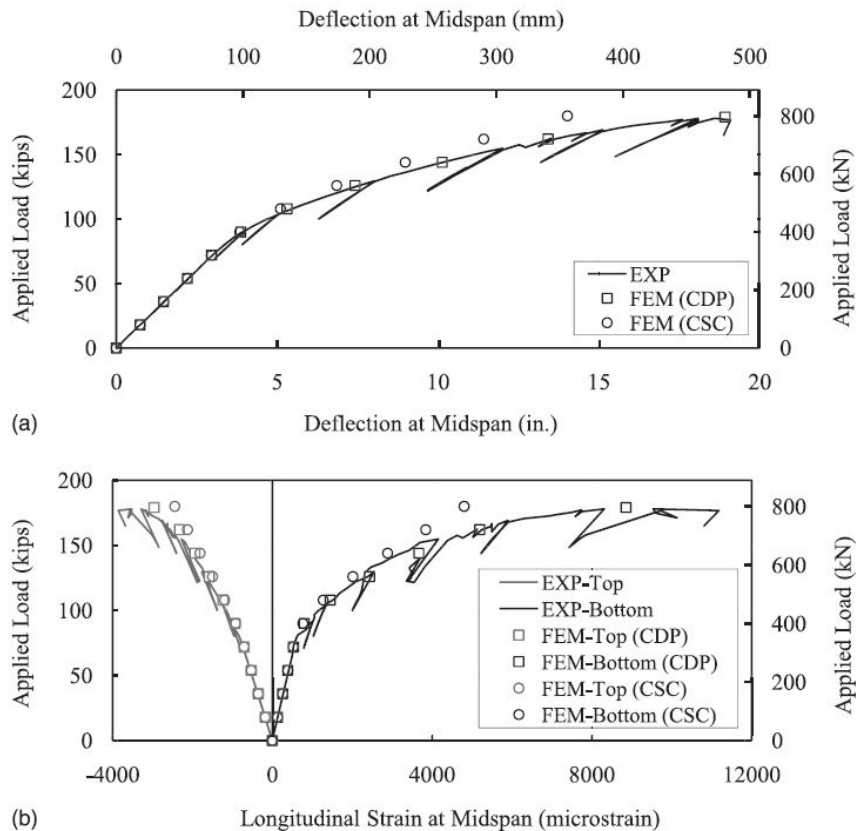
Figure 2.20: Experimental and finite element simulated load-deflection response for girders tested by (Chen and Graybeal, 2011a).

Chen and Graybeal (2011b)

Chen and Graybeal (2011b) also modelled the behaviour of prestressed second-generation UHPC pi-girder using the concrete damage plasticity model in ABAQUS. The second generation pi-girders were developed from a research program aimed at optimizing prestressed girders to efficiently utilize UHPC. The CDP model was reconfirmed to be consistent and reliable in replicating the behavioural response. Parametric studies on the effect of mesh size, Young's modulus, and use of diaphragms were also conducted.

Singh et al. (2017)

Singh et al. (2017) validated the applicability of using the CDP model in ABAQUS for simulating the behaviour of large-scale UHPFRC beams. The material properties required for the model were calibrated with the test data. The uniaxial tension and compression stress-strain responses were obtained from standard material tests. Eight-noded reduced integration brick elements were used to model the concrete. The steel reinforcement was modelled as 3D truss elements with axial deformation only. Perfect bond was assumed between the reinforcement and concrete.

The models were validated using the full-scaled UHPFRC beams tested by Singh et al. (2017), as discussed in Section 2.2. Figure 2.21 shows the comparison between the finite element results and experimental results for the four beams. The flexural capacities predicted by the model were within 5% of the experimental results, and the models captured both the pre- and post-peak load-displacement behaviour.
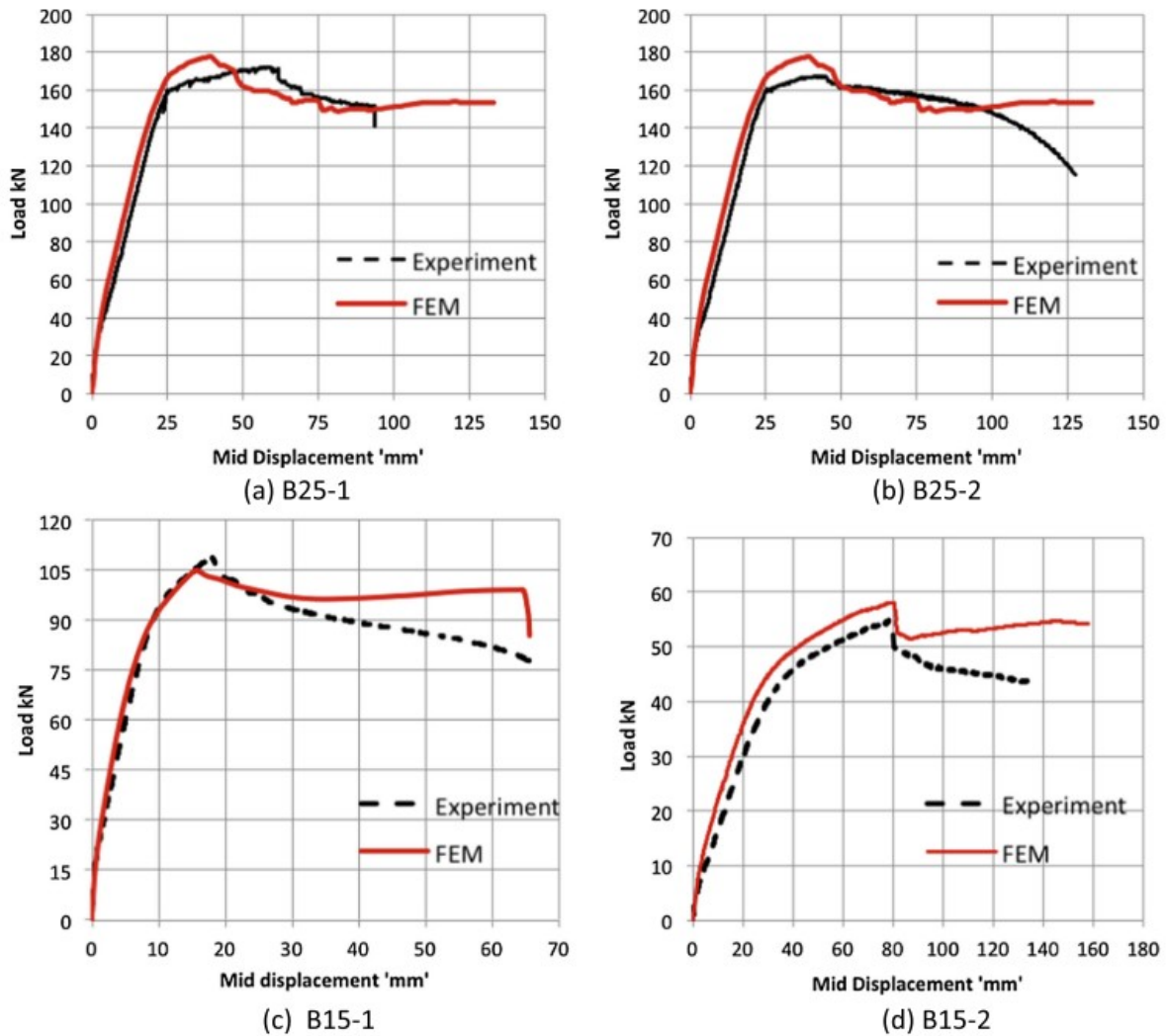
Figure 2.21: Experimental and finite element simulated load-deflection response for beams tested by (Singh et al., 2017).

Solhmirzaei and Kodur (2017)

A finite element based numerical model was also created in ABAQUS by Solhmirzaei and Kodur (2017) for UHPFRC beams under flexure and shear. The beams were discretized using eight-noded reduced integration brick elements for concrete and two-noded link elements for steel. The CDP model in ABAQUS was used to capture the nonlinear response of UHPFRC. A comprehensive set of material properties, such as compression hardening, tension stiffening, elastic modulus, poison's ratio and density, was required to define the CPD model for the analysis. A nonlinear tension damage parameter recommended by Chen and Graybeal (Chen and Graybeal, 2011a,b) was incorporated in the model to account for the reduction in stiffness after cracking. The compressive

strength, corresponding strain, and elastic modulus were derived from material tests. The post-peak strain-softening behaviour was modelled by the empirical equation proposed by Singh et al. (2017).

The model was validated using the full-scale tests on four UHPFRC beams under flexural and shear loading conducted by Kodur et al. (2018) discussed in Section 2.2. Figure 2.22 shows the comparison between the FE model and experimental results for beam U-B5 under flexure and beam U-B6 under shear. The model's predictions of the load-deflection response, load-strain response, and crack propagation of the UHPFRC were in good agreement with the experimental results.
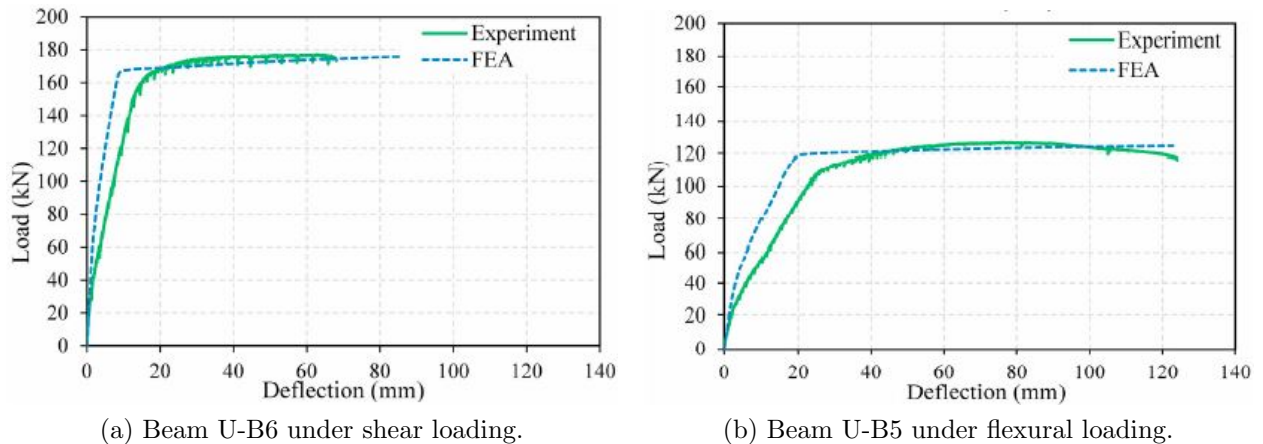
(a) Beam U-B6 under shear loading.   (b) Beam U-B5 under flexural loading.
Figure 2.22: Experimental and finite element simulated load-deflection response for beams tested by (Solhmirzaei and Kodur, 2017).

Franssen et al (2018)

Franssen et al. (2018) developed a new modelling approach in the nonlinear finite element software VecTor2 for UHPFRC-strengthened concrete members. Different strengthening layouts were considered: a layer of UHPFRC on the compressive side, on the tensile side, U-shaped layers, and layers with and without conventional steel reinforcement. This approach then adapted the DEM within the global framework of the Disturbed Stress Field Model (DSFM) in VecTor2. This study demonstrated that although the DSFM and the DEM were originally developed for reinforced concrete and fibre reinforced concrete, they can be easily extended to model UHPFRC-strengthened members. The advantage of this is the straight forward, relatively low number of input parameters required to define the behaviour of ultra-high performance concrete.

The DEM was first modified for UHPFRC by increasing the bond strength from $\tau_{f,max} = 0.396\sqrt{f'_c}$ (MPa) to $\tau_{f,max} = 0.75\sqrt{f'_c}$ (MPa), where f'_c is the concrete compressive strength in MPa. This is in response to the high density and high cement content of the UHPFRC matrix. In addition, this

model proposed a simplified expression for crack spacing: $s_{cr} = 0.75l_f$ (mm), where l_f is the fibre length in mm. A simplified expression for the relationship between crack width and average strains was adopted. The compression response was modelled on the same basis as for FRC. The modulus of elasticity was determined from tests or assumed to be 50 GPa. Finally, aggregate interlock was not considered due to the small aggregate size used in UHPFRC.

Eighteen UHPFRC-strengthened beams and three UHPFRC-strengthened columns from seven experimental studies from the literature were used to validate the modelling. Compared to the experimental tests, the results from these models showed good strength predictions for UHPFRC-strengthened beams and columns. In modelling UHPFRC-strengthened beams, the FE models produced an experimental-to-predicted ratio of 1.00 and a coefficient of variation (COV) of 11.12%. In modelling UHPFRC-strengthened columns, the FE models also captured the experimental results well; however, the displacement corresponding to steel rupture was overestimated. Figure 2.23 shows the strength prediction results for 21 specimens with UHPFRC layers. The horizontal axis shows the ratio of thickness of UHPFRC to total section depth, while the vertical axis shows the experimental-to-predicted failure load of each specimen.
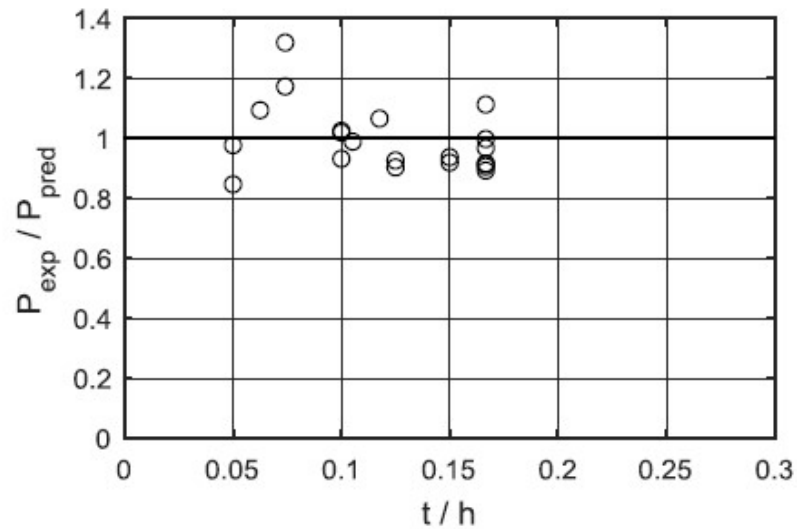
Figure 2.23: Stress to crack width response for FRC and UHPFRC as adapted from Franssen et al. (2018).

Yin et al. (2019)

Yin et al. (2019) performed finite element modelling of UHPC members under static flexural loading using the plasticity-based constitutive model in finite element analysis software LS-DYNA. The

concrete damage model available in LS-DYNA as material MAT_72R3 was used to model the behaviour. This concrete model employed two different simulation methods: a simplified method, where only the concrete compressive strength was required as an input, and a more detailed method, which required detailed input parameters from a variety of different laboratory tests. In this study, the authors used the simplified method to automatically generate the parameters required for the second method. These generated inputs were then adjusted based on the results of various parametric studies. The concrete damage model was calibrated through investigation of mesh size and a study of the strain rate effect on a single mesh element.

The authors used 21 UHPC specimens from multiple experimental programs to validate the FE model and modelling techniques. Included in the validation study were the experimental programs conducted by Yang et al. (2010) and Yoo and Yoon (2016), which were both discussed in Section 2.2. A total of 12 specimens contained no longitudinal reinforcement, while the 9 others were reinforced with longitudinal bars. All specimens had rectangular cross sections with varying dimensions ranging from model scales to full scale. Three specimens were fabricated and tested by the authors. The finite element model showed good agreement with the observed experimental results. Figure 2.24 shows the comparison between the finite element results and experimental results for the beams tested by the authors. Characteristics of the load-deformation responses such as ultimate strength, deflection at peak load, stiffness, hardening and softening behaviour, were in agreement with the experimental results. Post-peak responses showed less agreement with the experimental results. Although the finite element model presented good agreement with the experimental results, this method requires detailed calibration through experimental results, especially for specimens with different lengths of steel fibres. As such, further investigations are required to determine the effects of steel fibre length on the numerical results.
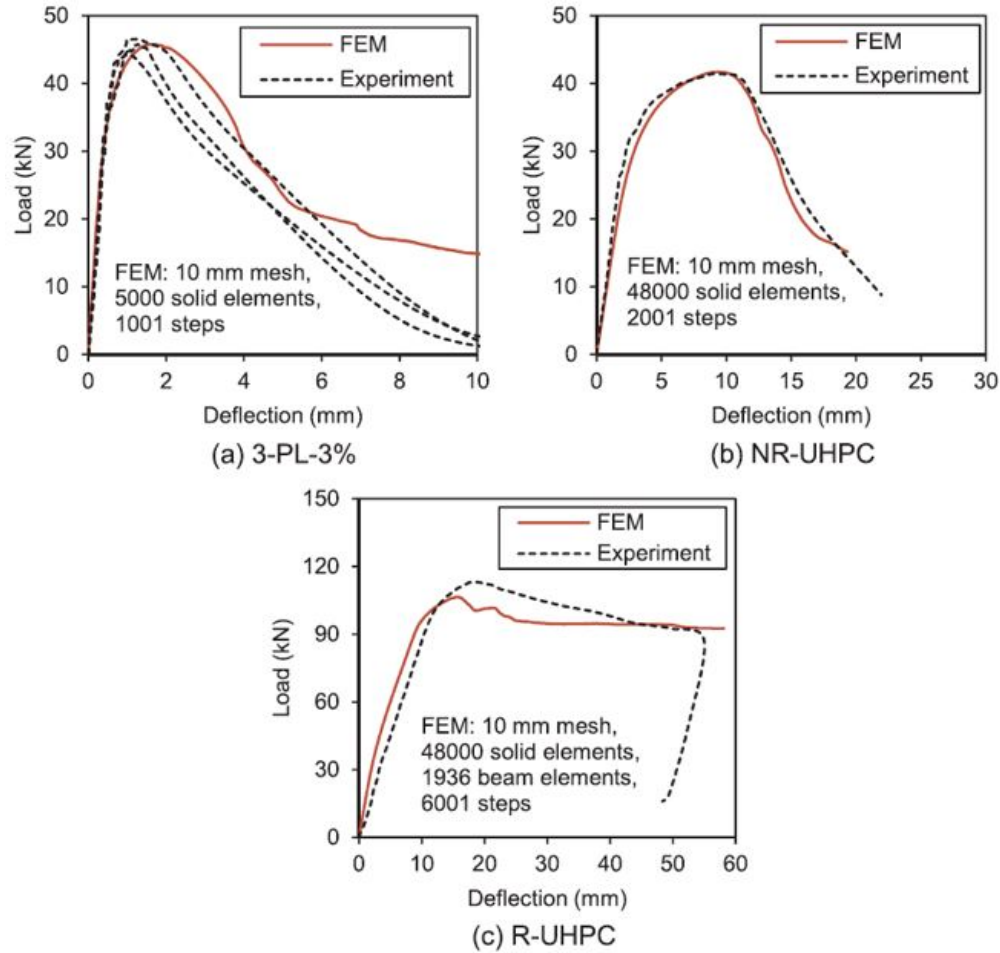
Figure 2.24: Experimental and finite element simulated load-deflection response for beams tested by Yin et al. (2019).

2.5 Reinforcement Rupture

In UHPFRC containing conventional steel reinforcement, the steel reinforcement can rupture at low strain values due to its cracking behaviour and high bond strength. As such, it is necessary to study the ductility of concrete elements that result in reinforcement rupture. As limited research is available in this area, the following section summarizes the work of researchers who have conducted experiments or developed numerical models related to the tensile behaviour of normal strength reinforced concrete without fibres and other reinforced cementitious composites. Special attention was given to research that captured the rupture strain of embedded steel reinforcement within these materials.

Mayer and Eligehausen (1998)

Mayer and Eligehausen (1998) performed 34 tests on reinforced concrete columns loaded in uniaxial tension up to reinforcement rupture to investigate bond behaviour beyond reinforcement yielding in normal reinforced concrete without fibres. The test results were used to verify a rational bond model to be implemented into a nonlinear finite element program NELIN2.

The test setup is shown in Figure 2.25. Uniaxial tensile load was applied using a displacement controlled loading rate of 0.01 mm per second up to steel yielding, and 0.02 mm per second up to rupture of the steel. The overall elongation was measured using four displacement meters (LVDT) with a gauge length of 2000 mm. The 34 tests varied in reinforcement ratio, ρ; bar diameter, d_s; steel ductility (ductility classes B, A, and S according to CEB-FIP Model Code 90); and concrete strength.
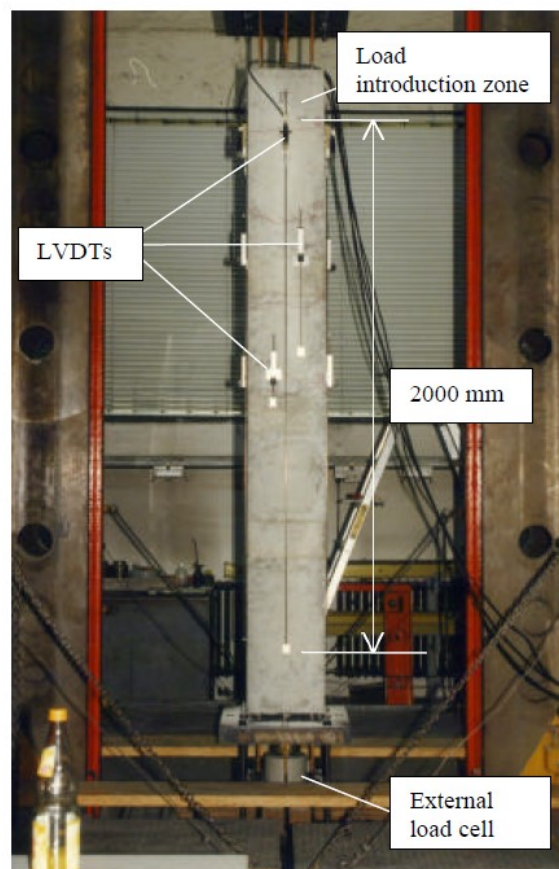
Figure 2.25: Test setup by Mayer and Eligehausen (1998).

Figure 2.26 shows the stress-strain response of the bare bar and embedded bar for specimen with ρ = 0.5%, d_s = 16 mm. The steel is class A (MC 90) and had a yield strength and ultimate strength of

519 MPa and 588 MPa, respectively. The concrete compressive strength was 28.4 MPa. The x-axis shows the overall elongation, and the y-axis shows the measured stresses. The average bare bar rupture strain was 85 millistrain while the same reinforcement within the tension member ruptured at an average strain of 45 millistrain. The authors concluded that the post-yielding behaviour of reinforced concrete elements was significantly influenced by steel ductility and reinforcement percentage.
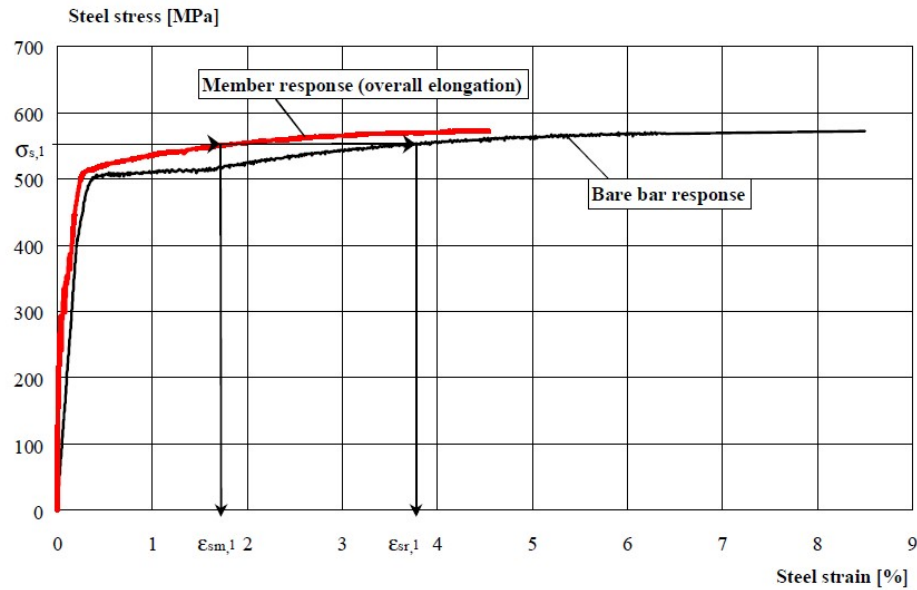
Figure 2.26: Stress-strain behavior of reinforced concrete member in tension ($\rho = 0.5\%$, bar diameter d_s=16 m, steel class A) tested by Mayer and Eligehausen (1998).

Lee et al. (2011)

Lee et al. (2011a) developed a tension stiffening model for reinforced concrete elements subjected to uniaxial tension, shear, or flexure. This model presented a better representation of reinforced concrete members' post-yielding stiffness, strength, and ductility. It allowed for the calculation of reinforcement stresses at crack locations after yielding and thus, allowed for the determination of average strain conditions resulting in reinforcement rupture. The model showed that contrary to what has been typically assumed, significant average tensile stresses still exist in concrete after yielding of reinforcement.

Figure 2.27 shows the algorithm used for the crack analysis procedure. This model employs a crack analysis approach that takes into account the bond mechanism between concrete and deformed reinforcing bars. Numerical analyses were conducted on reinforced concrete members subjected to

uniaxial tension, with particular emphasis on the post-yielding behaviour.
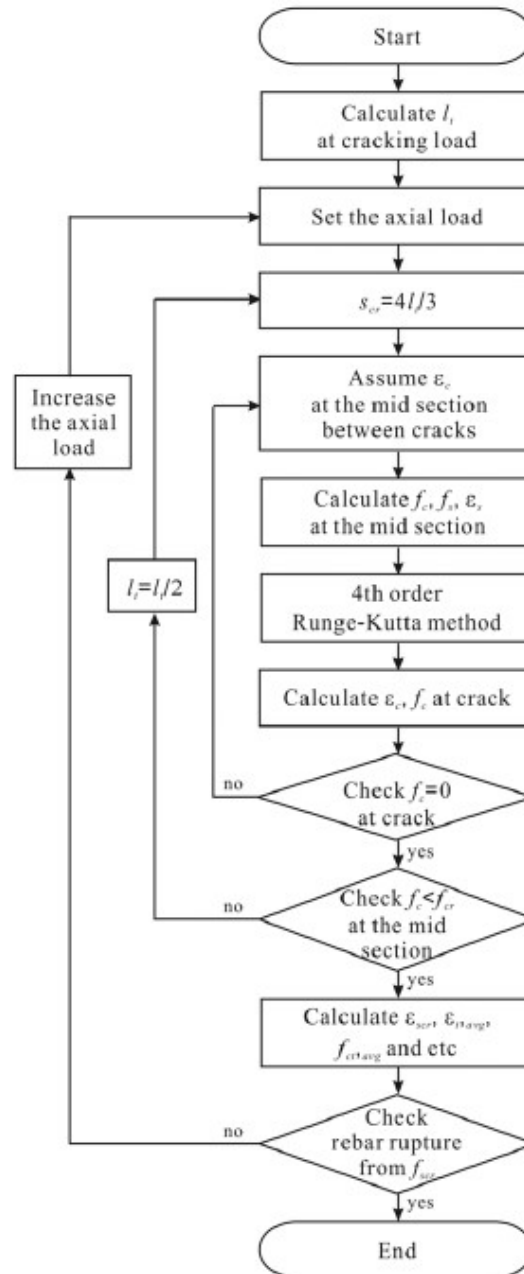
Figure 2.27: Algorithm for crack analysis procedure proposed by Lee et al. (2011).

Verification of this tension stiffening model was performed using uniaxial tension members tested by Mayer and Eligehausen (1998). These results were compared with the results of the CEB-FIP Model Code 90 (MC90) tension stiffening formulation, which does not check steel stress at a crack against the reinforcement yield strength limit. Figure 2.28 shows the comparison between different tension stiffening models and experimental results of specimens tested by Mayer and Eligehausen

(1998). The Lee 2011 model showed good agreement with experimental results, while the MC90 formulation produced less accurate predictions of the behaviour after yielding of the reinforcement.
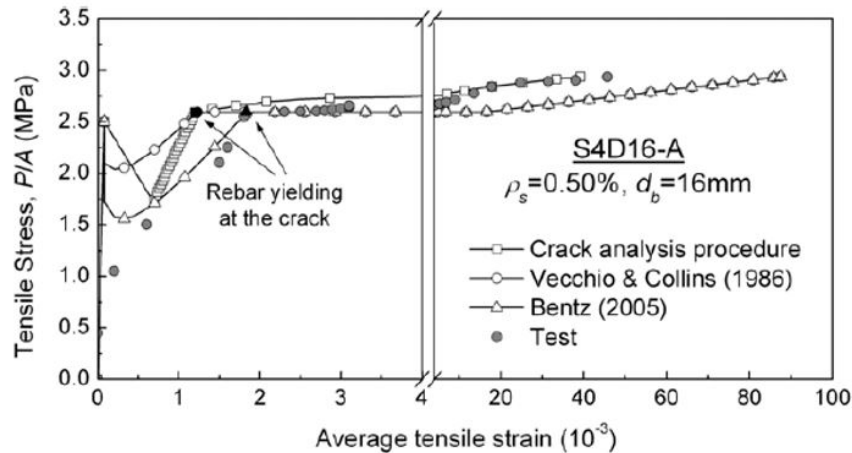
Figure 2.28: Analysis result for reinforced concrete member subjected to uniaxial tension. Lee et al. (2011).

Moreno et al. (2014)

Moreno et al. (2014) characterized the elastic and plastic response of reinforced high-performance fibre-reinforced cement-based composite (HPFRCC) materials containing polyvinyl alcohol (PVA) fibres. A total of 18 specimens with four cementitious materials were tested in uniaxial tension. The cementitious specimens included four normal weight concrete specimens, six engineered cementitious composite (ECC) specimens, four hybrid fibre reinforced concrete (HyFRC) specimens, and four self-consolidating hybrid fibre reinforced concrete (SC-HyFRC) specimens. It is important to note that the PVA fibres used in the HPFRCC specimens may result in different behaviour compared to steel fibres.

Figure 2.29 shows the specimen details and test setup. Displacement-controlled uniaxial tensile loading was applied until rupturing of the steel reinforcing bar. Nine strain gauges were placed along the embedded reinforcing bar in one of each material type. Elongation of the central region of each specimen was measured with two LVDTs.
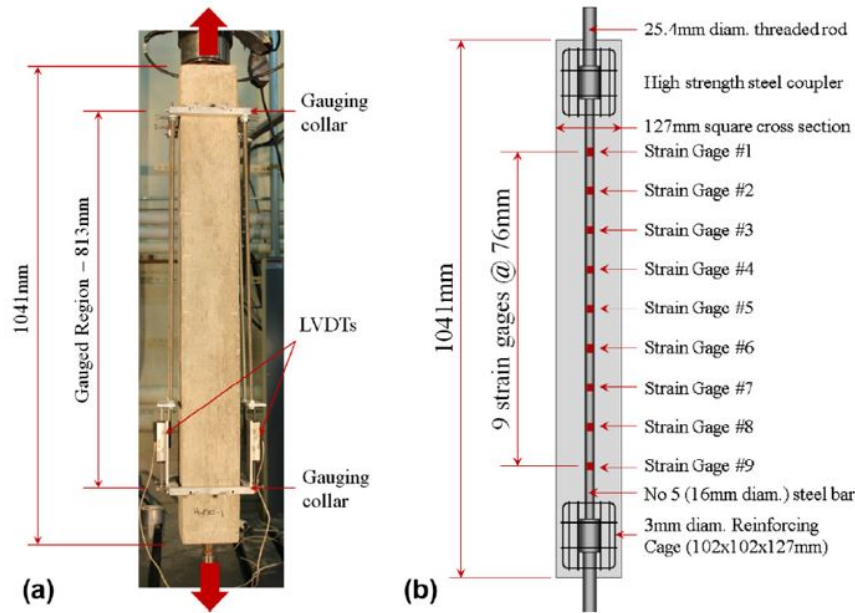
Figure 2.29: Prismatic specimen (a) test setup; (b) dimensions and strain-gauge placement. Moreno et al. (2014).

The specimens had square cross sections with side lengths of 127 mm and an 813 mm long region of interest. The total length of the specimens was 1040 mm. The reinforcement used was a United States number 5 (16 mm diameter) deformed steel bar ($\rho = 1.2\%$). The reinforced concrete specimens had a mean compressive strength of 44 MPa. The ECC specimens had a mean compressive strength of 54 MPa and contained 2.0% by volume of 12.7 mm long, 0.04 mm diameter polyvinyl alcohol (PVA) fibres. The HyFRC specimens had a mean compressive strength of 31 MPa and contained 0.2% by volume of 8 mm long, 0.04 mm diameter PVA fibres, 0.8% by volume of 60 mm long, 0.75 mm diameter steel end-hooked fibres, and 0.5% by volume of 30 mm long, 0.55 mm diameter steel end-hooked fibres. The SC-HyFRC specimens had a mean compressive strength of 40 MPa and contained 0.2% by volume of 8 mm long, 0.04 mm diameter PVA fibres, and 1.3% by volume of 30 mm long, 0.55 mm diameter steel end-hooked fibres.

Figure 2.30 shows the experimental results of all members tested. All HPFRCC specimens exhibited early reinforcement rupture compared to the concrete specimens. The authors speculated that this is attributed to the material's ability to resist splitting crack formation. In the reinforced concrete specimens, longitudinal splitting cracks were observed at low strain values, as shown by the red circles in Figure 2.30. In the HPFRCC specimens, the transverse cracks formed were bridged by fibres, which allowed the strains to spread along greater lengths of the reinforcing bar in the vicinity of the transverse cracks. If the formation of splitting cracks is prevented, strain will localize in the

first dominant transverse crack, leading to early fracture of the steel reinforcement. The ECC
specimens had the highest tensile strength compared to the other three materials, which prevented
the formation of splitting cracks and led to the lowest deformation capacity. In HyFRC and
SC-HyFRC specimens, the splitting crack formation was delayed relative to the concrete specimens,
which resulted in a lower deformation capacity compared to the reinforced concrete specimens.
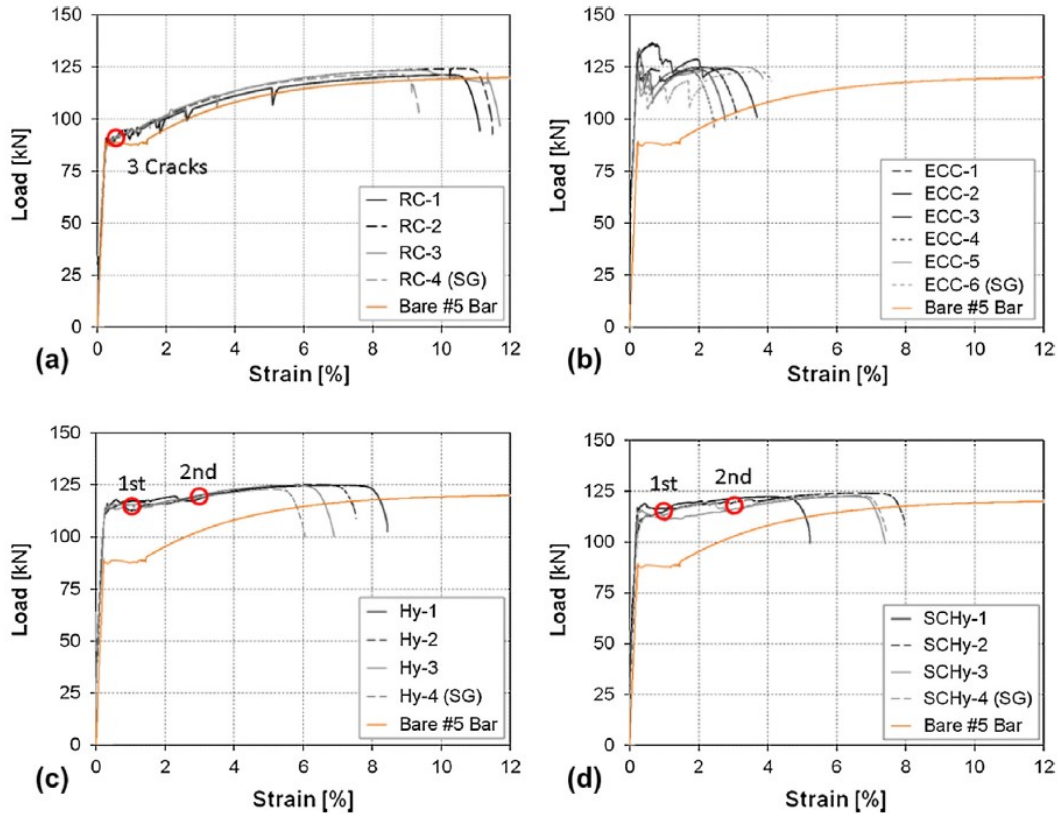
Figure 2.30: Complete load-average strain response for (a) concrete; (b) ECC; (c) HyFRC; (d)
SC-HyFRC specimens tested by Moreno et al. (2014). Red circles indicate splitting crack
formation.

The authors then used the experimental data to propose a modified approach for estimating
the flexural capacity of reinforced HPFRCC members. However, additional tension stiffening
experiments are needed to validate the proposed method for use in design. The authors also
concluded that further research is required to investigate the influences of reinforcement diameter
and ratio on reinforcement deformation capacity.

Kang et al. (2017)

Kang et al. (2017) studied the effect of reinforcement ratio on tension stiffening behaviour of

reinforced concrete and ECC members. A total of ten specimens with centrally embedded reinforcement were tested in uniaxial tension. The specimens had square cross sections with varying dimensions. The length of the specimens remained constant at 1000 mm. Figure 2.31 shows the test setup for reinforced ECC and concrete specimens. T-shaped steel brackets were connected to the longitudinal reinforcement through bolts and clamped by a testing machine to apply tension to the specimen. The average values of ECC and concrete compressive strengths were 51.7 MPa and 42.2 MPa, respectively. The ECC specimens contained 2% by volume of 12 mm long, 0.039 mm diameter PVA fibres.
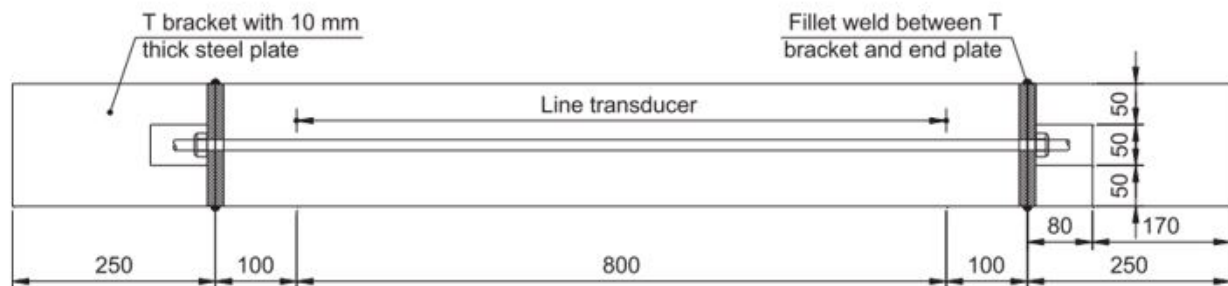
Figure 2.31: Test setup by Kang et al. (2017).

Figure 2.32 shows the load versus strain response for the specimens up to failure. The results from this experiment were similar to those reported by Moreno et al. (2014) in that the reinforced ECC specimens developed more significant tension stiffening, and the strain capacities were generally considerably smaller than that those of normal reinforced concrete specimens. Splitting cracks were prevented due to better confinement in ECC and resulted in premature failure compared to the normal concrete specimens. At low reinforcement ratios (0.59%), both the ECC and concrete specimens developed a major localized crack, which eventually caused local failure. However, splitting crack in the RC specimen was prevented by the adequate concrete cover. Thus, the ultimate strain of the normal concrete specimen was lower than that of the ECC specimen (see Figure 2.32c). The test results concluded that the ECC specimens were less sensitive to longitudinal reinforcement ratio than the reinforced concrete specimens.
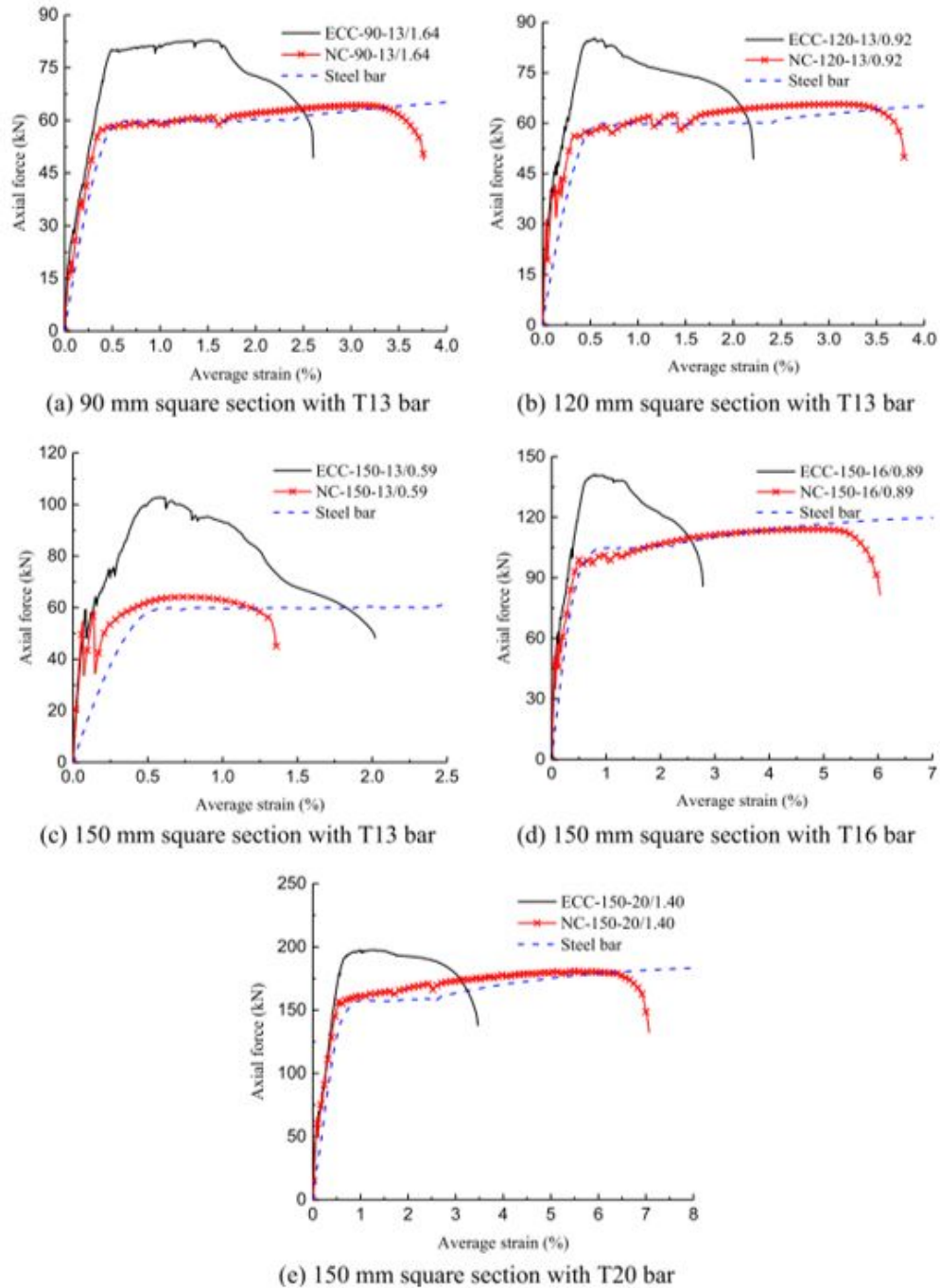
Figure 2.32: Complete load-average strain response for specimens tested by Kang et al. (2017).

Nguyen et al. (2019)

Nguyen et al. (2019) investigated the failure characteristics of reinforced hybrid fibre-reinforced concrete (HyFRC) under direct tension. Hybrid fibre-reinforced concrete is a class of fibre reinforced concrete that includes two or more fibre types. Under direct tension and with certain reinforcement ratio, reinforced HyFRC generally exhibits an overall hardening behaviour after

initial reinforcement yielding.

Four conventional reinforced concrete and three reinforced HyFRC prismatic samples, each with a centrally embedded reinforcing bar, were prepared for experimentation. Figure 2.33 shows the experimental details of the prismatic test specimens. Displacement controlled uniaxial tensile loading was applied until rupturing of the steel reinforcing bar.
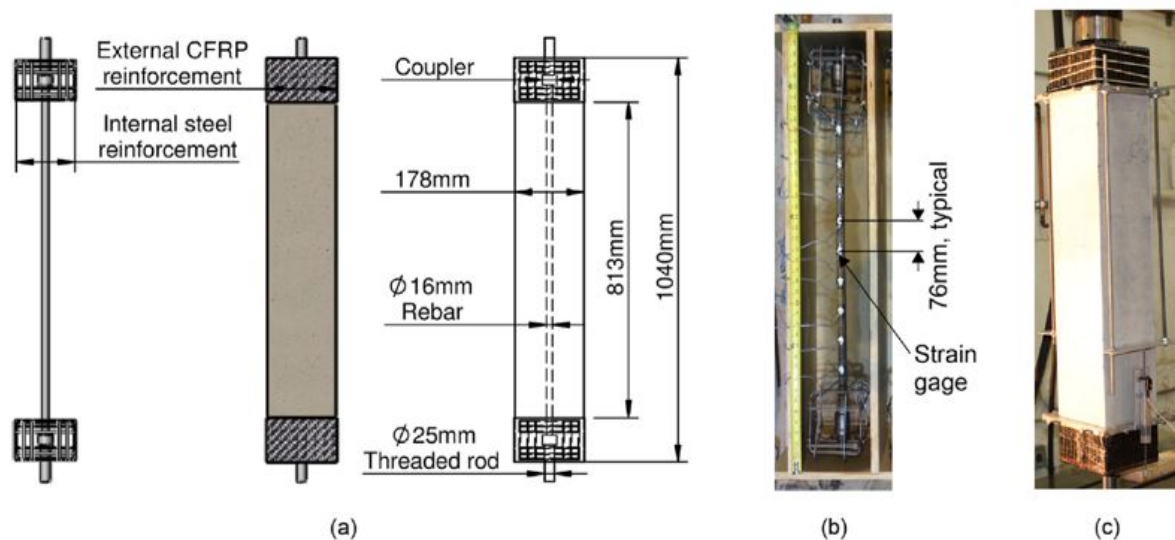
Figure 2.33: Specimen details: (a) materials and detailing; (b) strain-gauges placed prior to casting; and (c) global view of specimen prior to testing.

The reinforced concrete and HyFRC had mean compressive strengths of 42 MPa and 40 MPa, respectively. The HyFRC contained 1.5% by volume fibre content consisting of a blend of 8 mm long PVA fibres, 30 mm long end-hooked steel fibres, and 60 mm long end-hooked steel fibres. The specimens had square cross sections with side lengths of 178 mm and an 813 mm long region of interest. The total length of the specimens was 1040 mm. The reinforcement used was a United States number 5 (16 mm diameter) A706 steel bar with deformed ribs (ρ= 0.6%). The yield stress and ultimate stress of the rebar were 440 MPa and 620 MPa, respectively.

Measured load-average strain response for strains up to 0.4% (4 millistrain) are shown in Figure 2.34a, and the complete response is shown in Figure 2.34b. The mean embedded reinforcement rupture strain for the concrete specimen was 7.2% (72 millistrain) while the mean rupture strain for the HyFRC was 3.4% (34 millistrain), representing a 53% reduction. The bare bar rupture strain was not captured.
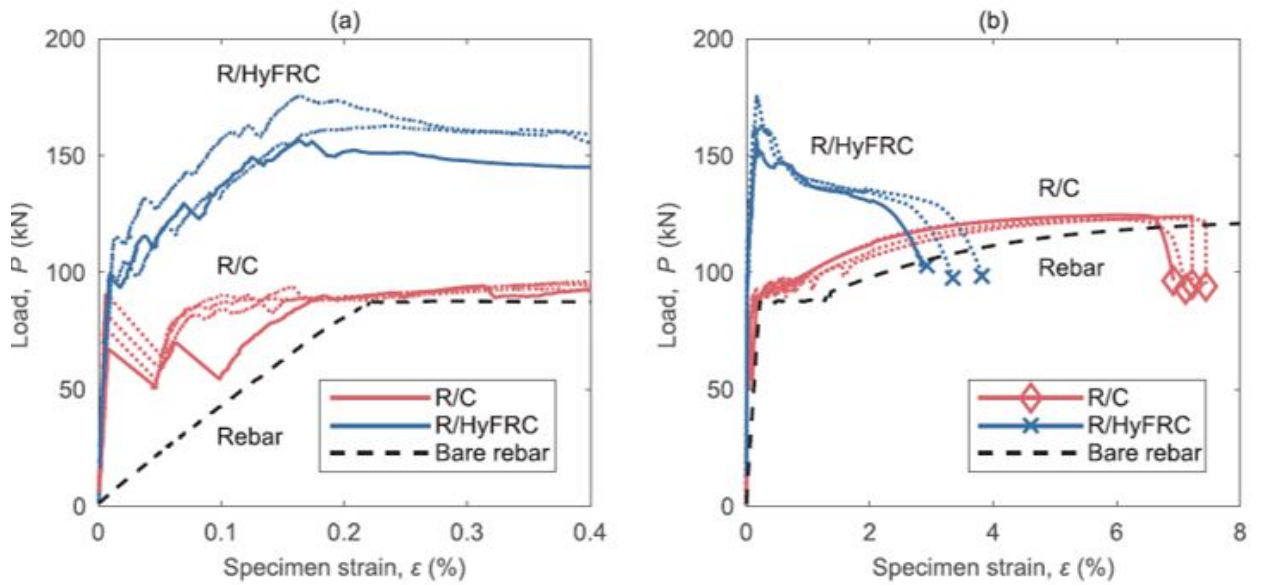
Figure 2.34: Load-average strain response of (a) up to $\varepsilon = 0.4\%$ and (b) complete response for specimens tested by Nguyen et al. (2019).

Chapter 3

Preliminary Studies

This chapter provides the preliminary studies on finite element modelling of UHPFRC elements using VecTor2. The purpose of these preliminary analyses was to investigate the influence of key parameters on UHPFRC modelled behaviour. The specimen modelled in this chapter was from a series of UHPFRC panels tested under pure shear monotonic conditions at the University of Toronto (Yap, 2020). The investigated parameters include concrete tensile strength (f_t'), FRC post-cracking tension models, maximum aggregate size (a), crack spacing (s_{cr}), and mesh size. Stochastic analyses were also performed to account for uncertainties in material properties, as well as to investigate the variability of properties within the specimen. All models were constructed using VecTor2's pre-processor software FormWorks (Wong et al., 2013). The results are processed and analyzed using VecTor2's post-processor Augustus (Bentz, 2010).

3.1 Modelling of the Panel

3.1.1 Panel YS1

Panel YS1 was 1625 mm by 1625 mm and 215 mm thick. The reinforcement consisted of both fibres and conventional reinforcement. The fibres included 1% of end-hooked fibres and 1% of straight fibres. The convention reinforcement used were Canadian 10M bars (bar area per bar = 100 mm^2) in both the x- and y-directions, allowing for 0.861% reinforcement in each of the two directions.

For simplicity, Panel YS1 was modelled in VecTor2 as a single four-noded plane stress rectangular element with a dimension of 1000 mm by 1000 mm and 100 mm thick. The lower left corner of the element was restrained in both the x- and y-direction, while the lower right corner was restrained in the y-direction only. As shown in Figure 3.1a, the model was load controlled, with loads applied at the nodes to create a pure shear loading condition. Loading was monotonically increased by 5 kN (0.05 MPa shear stress) at each analysis step until failure.

(a) Idealized panel.   (b) FormWorks model.
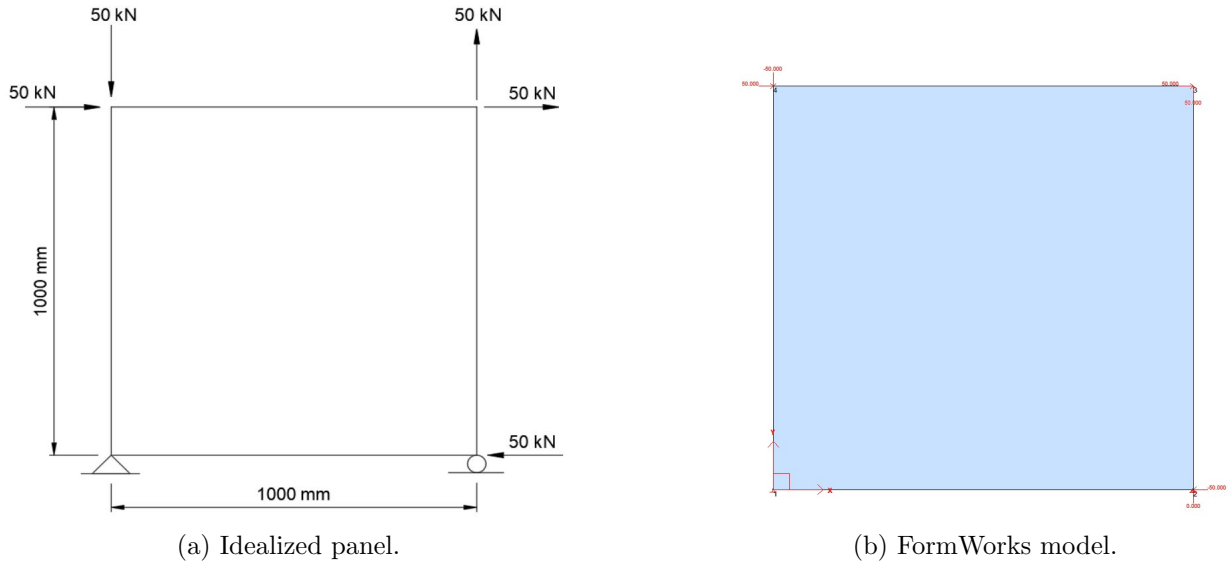
Figure 3.1: Finite element modelling of panels.

3.1.2 Model Parameters

The fibre reinforcement was modelled as smeared reinforcement by selecting end-hooked steel fibre as one reference type, and straight steel fibre as the second reference type. The conventional reinforcement was also modelled as smeared reinforcement by using the ductile steel reinforcement reference type.

The majority of the mechanical properties of the concrete found through material testing were not used as input parameters, but rather determined by the program, with the exception of concrete compressive strength, f'_c, concrete elastic modulus, E_c, and maximum aggregate size, a. The input longitudinal reinforcement parameters included reinforcement diameter, d_b, reinforcement ratio, ρ, yield strength, f_y, and ultimate strength, f_u. The fibre input properties included fibre volume ratios, V_f, length, l_f, diameter, d_f, and fibre ultimate tensile strength, f_{uf}. The input concrete and fibre properties are shown in Table 3.1, and the input reinforcement properties used are presented in Table 3.2. Default material properties calculated by VecTor2 are shown in Table 3.3.

Table 3.1: Concrete and fibre properties

Specimen ID	Thickness	Concrete			Straight Fibre				End Hooked Fibre			
		f'_c	E_c	a	V_f	l_f	d_f	f_{uf}	V_f	l_f	d_f	f_{uf}
	mm	MPa	GPa	mm	%	mm	mm	mm	%	mm	mm	mm
YS1	100	171	49.3	1	1	20	0.2	2700	1	25	0.25	2700

Table 3.2: Reinforcement properties

Specimen ID	Direction	ρ %	d_b mm	f_y MPa	f_u MPa	E_s MPa
YS1	X [0°]	0.861	10	480	600	200000
	Y [90°]	0.861	10	480	600	200000

Table 3.3: Default material properties

Concrete Properties		Steel Properties	
Tensile Strength (MPa)	$f'_t = 0.33\sqrt{f'_c}$	Elastic Modulus (MPa)	$E_s = 200000$
Cylinder Strain at f'_c (x10⁻³)	$\varepsilon_o = 1.8 + 0.0075 f'_c$	Strain Hardening Strain (x10⁻³)	$\varepsilon_{sh} = 10$
Poisson's Ratio	$\mu = 0.15$	Ultimate Strain (x10⁻³)	$\varepsilon_u = 150$
Mass Density (kg/m³)	$\gamma = 2400$	Poisson's Ratio	$\mu = 0.30$
Maximum s_x and s_y* (mm)	1000	Mass Density (kg/m³)	$\gamma = 7850$

*Maximum crack spacing values; VecTor2 calculates s_x, s_y according to reinforcement conditions.

3.1.3 Constitutive Models

VecTor2 contains a comprehensive selection of analysis models for various behaviour mechanisms. To verify the adequacy of the available constitutive models, all chosen models not investigated in the parametric study were taken as VecTor2 default, apart from the pre-peak concrete compression curve. The Hoshikuma model (Hoshikuma et al., 1997), an exponential function, was selected for the ascending branch of the compression-stress strain curve. This is because this model is known to respond well to concrete with high compressive strengths. Table 3.4 shows the selection of concrete and reinforcement constitutive models.

Table 3.4: Constitutive models used for finite element analysis

Concrete Constitutive Models			
Compression Pre-Peak*	Hoshikuma et al.	**Dilation**	Variable - Isotropic
Compression Post-Peak	Modified Park-Kent	**Cracking Criterion**	Mohr-Coulomb (Stress)
Compression softening	Vecchio 1992	**Crack Stress Calc**	Basic (DSFM/MCFT)
Tension Stiffening	Modified Bentz 2003	**Crack Width Check**	Agg/2.5 Max Crack width
Tension Softening	Nonlinear (Hordijk)	**Crack Slip Calc**	Walraven
FRC Tension	SDEM - Monotonic	**Creep and Relaxation**	Not Considered
Confined Strength	Kupfer/Richart	**Hysteretic Response**	Nonlinear w/ Plastic Offsets
Reinforcement Constitutive Models			
Hysteretic Response	Bauschinger Effect (Seckin)	**Buckling**	Modified Dhakal- Maeka
Dowel Action	Tassios (Crack Slip)	**Concrete Bond**	Eligehausen

∗non-default models.

3.2   Parametric Study

A parametric study involving six parameters was performed to consider the effect of those variables on the UHPFRC modelled behaviour in VecTor2. Table 3.5 lists the investigated parameters.

Table 3.5: Parameters investigated in the parametric study

Parameters	Symbol	Values
Tensile Strength (MPa)	f_t'	$0.33\sqrt{f_c'}, 0.4\sqrt{f_c'}, 0.5\sqrt{f_c'}, 0.6\sqrt{f_c'}$
SFRC Post-cracking Tension Model	-	DEM, SDEM, VEM
Maximum Aggregate Size (mm)	a	1, 2, 4, 6, 20
Crack Spacing (mm)	s_{cr}	5, 19.6, 50, 80
Element Size	-	1 element, 100 elements
Element tThickness (mm)	t	25, 50, 100, 200

3.2.1   Influence of Tensile Strength

In VecTor2, the default value for uniaxial cracking strength of conventional reinforced concrete is $f_c' = 0.33\sqrt{f_c'}$ MPa. Three other increasing tensile strengths were also investigated. From Figure 3.2, it can be seen that as tensile strength increases, the cracking stress of the element increases, while the post-cracking behaviour remains the same. Tensile strength does not influence

the predicted overall ultimate capacity or post-cracking deformation response.
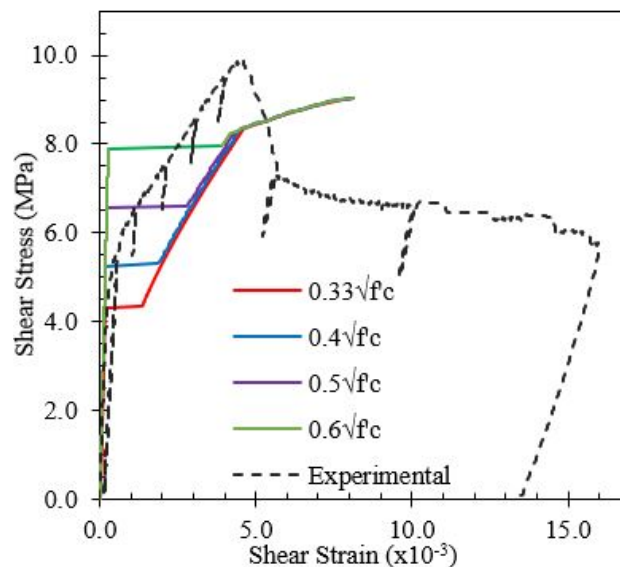
Figure 3.2: Influence of tensile strength of UHPFRC behaviour.

The inclusion of steel fibres in concrete is known to improve resistance to cracking when compared to conventional reinforced concrete. Current research has shown that the cracking strength of an UHPFRC member is dependent on many factors, such as fibre type, shape, and volume content (Yoo et al., 2016b). As such, Panel YS1 is expected to have a larger experimental cracking strength than the VecTor2 default cracking strength of $f_c' = 0.33\sqrt{f_c'}$ MPa. In Panel YS1, Figure 3.2 shows that the experimental cracking strength appears to be closer to $0.4\sqrt{f_c'}$ while VecTor2's default cracking strength is a conservative and a lower bound estimate of UHPFRC tensile strength. Despite the higher observed cracking strength, there are currently no widely accepted guidelines on how the cracking strength of UHPFRC is to be numerically determined. Therefore, in the absence of more available information, it is recommended to use the default cracking strength for modelling UHPFRC in VecTor2.

3.2.2 Influence of FRC Post-Cracking Tension Model

In VecTor2, several fibre reinforced concrete (FRC) tension models are available for considering the contribution of steel fibre reinforcement to the concrete post-cracking tensile response. Three FRC tension models were analyzed: the Diverse Embedment Model (DEM) (Lee et al., 2011a), the Simplified Diverse Embedment Model (SDEM) (Lee et al., 2013a), and the Variable Engagement Model (VEM) (Voo and Foster, 2003). The details of the different models are described in detail

in Chapter 2. The effect of the different FRC tension models on the UHPFRC behaviour of YS1 is shown in Figure 3.3. The selection of the FRC tension model is seen to have a significant effect on the post-cracking behaviour of UHPFRC. The pre-cracking shear stiffness was well predicted by all FRC models. However, all three models underestimated both the load-carrying capacity as well as the shear deformation capacity of the panel. The VEM calculated an ultimate shear capacity that most closely matched the experimental results of Panel YS1.
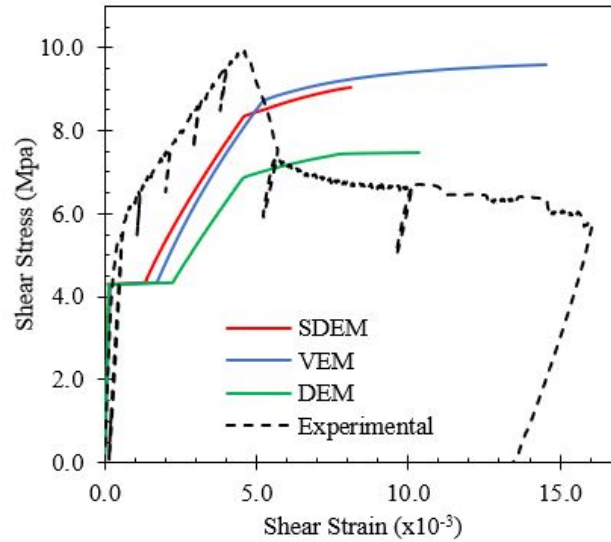
Figure 3.3: Influence of post-cracking tension model on UHPFRC behaviour.

3.2.3   Influence of Maximum Aggregate Size

In both the MCFT and DSFM, stress is transferred across a crack through aggregate interlock, which significantly influences the post-cracking behaviour of concrete subjected to shear-critical conditions. The maximum shear stress on the crack is influenced by both aggregate size, a, and crack width, w. In VecTor2, the default maximum aggregate size for reinforced concrete is 10 mm. Moreover, in VecTor2, materials with a maximum aggregate size of 2 mm or less are treated as a mortar, while those with a maximum aggregate size of greater than 2 mm are treated as concrete materials. This distinction results in different abilities for the material to redistribute post-cracking stresses through aggregate interlock. Figure 3.4 shows the effect of different aggregate sizes on predicted behaviour. In general, larger aggregate sizes gave results that are closer to experimental.

Since UHPFRC composition generally does not contain any coarse aggregate, it would be more appropriate to use smaller aggregate sizes in the finite element models. The recommended input aggregate size is less than 2 mm. However, despite UHPFRC's lack of coarse aggregate, the crack
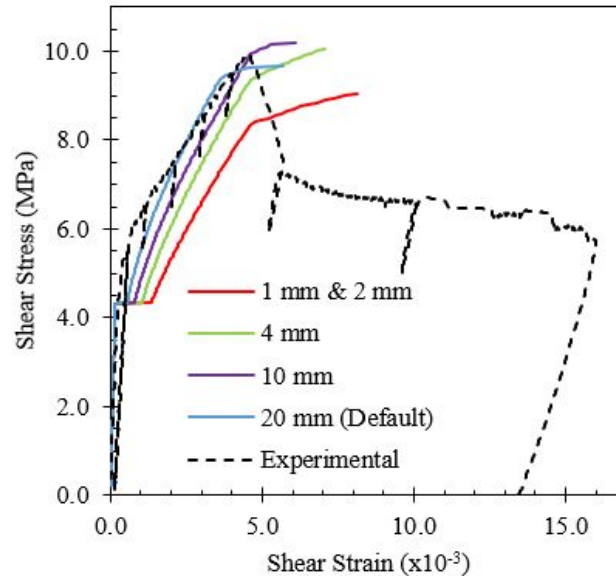
Figure 3.4: Influence of maximum aggregate size on UHPFRC behaviour.

surface is considerably rough due to the presence and action of steel fibres. Since the aggregate size affects a variety of parameters, such as crack spacing, this roughness needs to be sufficiently captured. It was proposed that an effective aggregate size calculation due to fibre frictional effects be considered in the VecTor2 formulation. This modification is further discussed in Chapter 4.

3.2.4 Influence of Crack Spacing

The addition of fibres in SFRC significantly improves its cracking characteristic by allowing for the formation of closely spaced cracks, thereby improving the tension stiffening behaviour and resulting in a larger post-yield load-carrying capacity compared to conventional reinforced concrete specimens. Thus, to accurately model the cracking characteristics, it is necessary to investigate the effect of average crack spacing on UHPFRC behaviour. VecTor2 allows for both program calculated and user input crack spacing values for use in its algorithm. The default crack spacing formulation for SFRC (Deluce et al., 2014) is adapted from fib Model Code 1978. It accounts for the effect of various reinforcement and fibre parameters, including clear cover or maximum aggregate size, longitudinal reinforcement ratio, bar size, fibre orientation, fibre content, fibre length, and fibre diameter. Figure 3.5 shows the effect of various input crack spacing values and VecTor2 calculated default crack spacing on modelled behaviour. An input crack spacing of 50 mm most closely matches experimental results.

For Panel YS1, the VecTor2 calculated crack spacing was 19.5 mm, while the experimental crack
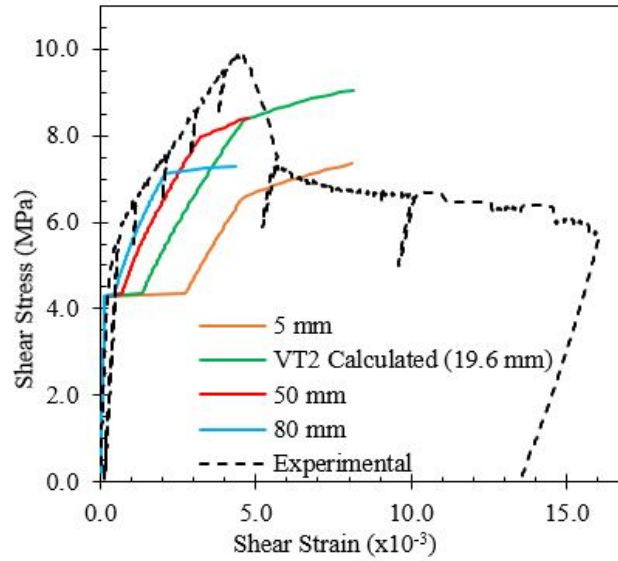
Figure 3.5: Influence of crack spacing on UHPFRC behaviour.
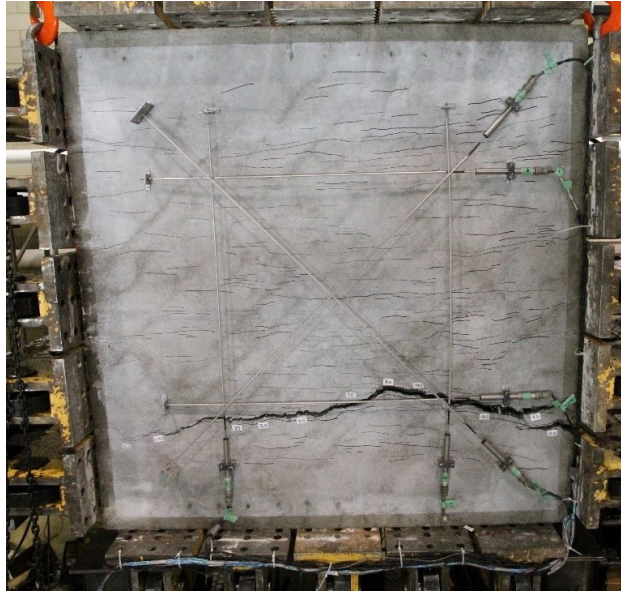
Figure 3.6: YS1 peak load crack pattern.

pattern shown in Figure 3.6 shows an average crack spacing of approximately 50 mm. This significant underestimation of crack spacing was partially due to the applicability of the SFRC crack spacing formulation to UHPFRC. Since UHPFRC typically contains much finer aggregates than conventional RC or SFRC, using a formulation dependent on maximum aggregate size for crack spacing calculations will result in significantly smaller crack spacing values that are not characteristic of UHPFRC.

Thus, although VecTor2 has been shown to adequately predicted crack spacing for SFRC (Deluce

et al., 2014), the current crack spacing formulations are not appropriate for UHPFRC. As a result, it is recommended to use user-input crack spacing values found through experimentation. Further research is required for the development of a suitable crack spacing formulation for UHPFRC.

3.2.5 Influence of Element Size and Thickness

In VecTor2, Luo (2014) eliminated the effect of mesh size by modifying the slip calculations to assume the same maximum crack width regardless of the element size. To confirm this elimination of mesh dependency, the panel was modelled using 100 elements (each element was 100 x 100 mm). Figure 3.7a shows this model with loads applied at each node to simulate pure shear loading. Figure 3.7b shows that the one-element model gives the same result as the 100-element model. As a result, the element size does not influence modelled behaviour.
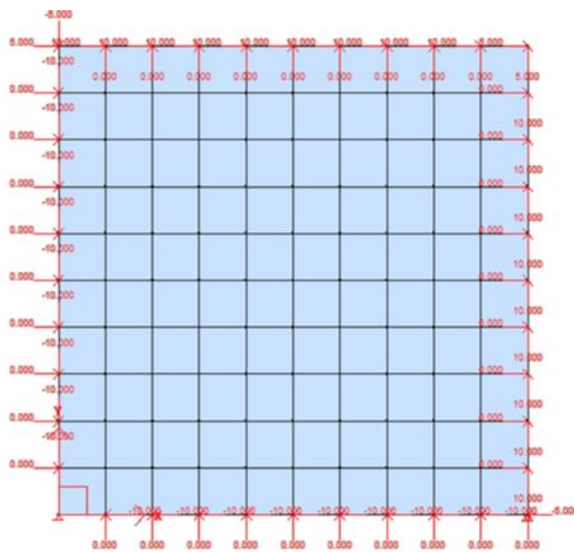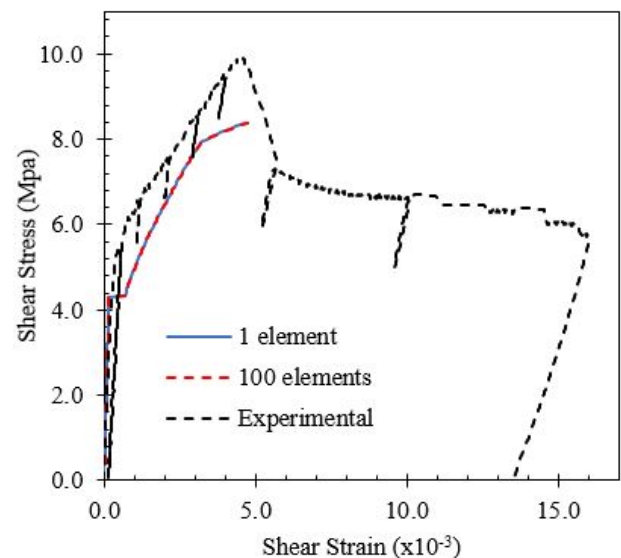
(a) Multi-element formworks model.   (b) Element size.
Figure 3.7: Influence of element size on UHPFRC behaviour.

Similarly, the effect of element thickness on the one-element model was also investigated, and the results are shown in Figure 3.8. Decreasing the element thickness appears to improve the post-cracking capacity and the shear deformation capacity of the element. This is because in VecTor2, the fibre efficiency factor is affected by the element thickness. As the element thickness decreases, fibres are more likely to be orientated parallel to the loading direction, thereby increasing the effectiveness of fibre bridging action and improving the ultimate strength capacity. Thus, it is essential to configure the model such that the actual specimen thickness is represented.
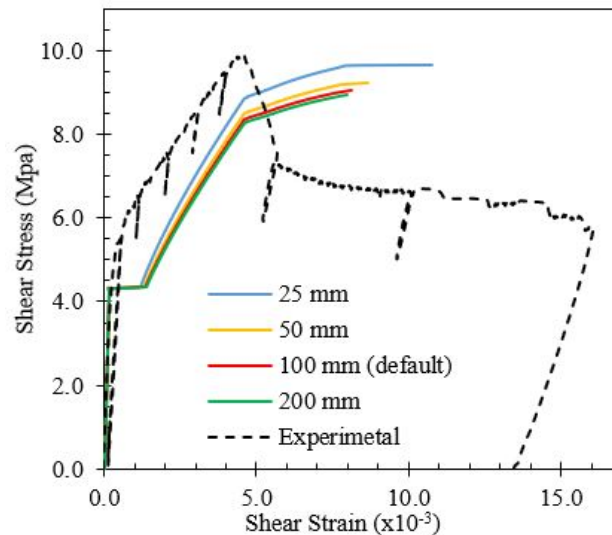
Figure 3.8: Influence of element thickness on UHPFRC behaviour.

3.3 Stochastic Analysis

As a composite material, fibre reinforced concrete is made of randomly distributed components such as sand, cement powder, and steel fibres. This random distribution may produce varying material properties in different positions of the member. As such, it may be important to investigate and quantify the impact of this inherent heterogeneity on modelled response. Stochastic simulations using both the Monte Carlo sampling and Monte Carlo sampling with random field spatial variation options available in VecTor2 (Hunter, 2016) were performed to consider uncertainties in the concrete and steel material properties.

Monte Carlo simulation is used when there are uncertainties in input material properties and is readily used in the reliability analysis of reinforced concrete. In a one-element model of YS1, uniform material properties were assigned to the entire panel. Monte Carlo sampling then generated statistically random numbers to a selected distribution for each of the selected input parameters.

In Monte Carlo sampling with spatially correlated random variables, variation of material properties within the panel can be investigated using a 100-element model. Each adjacent element is assumed to have material properties that are spatially correlated following a Gaussian random field distribution (Hunter, 2016). An example of the generated concrete compressive strength variation within the 100-element model is illustrated in Figure 3.9.

The input parameters considered for the stochastic analyses include the recommended default concrete and steel material distributions listed in Table 3.6. Additional parameters required for

179	181.1	182.5	184.2	186.2	188.6	190.5	191.3	190.8	188.8
176.8	178.7	180.2	181.8	184	186.4	188.6	190	190	189
175.3	177.2	178.5	180.1	181.9	184.2	186.6	188.3	189.1	188.8
174.4	176.1	177.3	178.5	180.1	182.1	184.3	186.4	187.6	188.3
174.1	175.6	176.5	177.3	178.4	180.1	181.9	184	185.7	186.9
173.7	174.9	175.4	175.8	176.5	177.5	179.2	181.1	183	184.9
173.4	174.2	174.2	174.1	174.1	174.6	175.8	177.5	179.7	181.9
172.7	172.9	172.5	171.9	171.2	171.2	172	173.6	175.8	178.5
171.7	171.2	170.1	168.9	167.9	167.6	168.1	169.6	172	175.1
170	168.9	167.4	165.9	164.7	164.2	164.5	166	168.6	172

Figure 3.9: One random field generation of concrete compressive strength, f'_c.

random field simulations are presented in Table 3.7. A total of 100 simulations were performed based on a reference strength taken as the known 28-day cylinder strength to remove the variability relating the cylinder strength to specified strength. The results of a stochastic simulation using Monte Carlo sampling is presented in Figure 3.10a, and the results of the stochastic simulation using spatially correlated random variables are shown in Figure 3.10b.

Table 3.6: Stochastic analysis parameters

Parameter	Model
Concrete	
Compressive Strength Dstn	Bartlett and MacGregor 1996
Tensile Strength Dstn	Mirza et al. 1979
Elastic Modulus Dstn	Hybrid Mirza + CSA
Steel	
Yield Strength Dstn	Nowak and Szerzen 2003
Ultimate Strength Dstn	Mirza et al. 1979
Elastic Modulus Dstn	Mirza et al. 1979

Table 3.7: Additional parameters for Monte Carlo sampling with spatially correlated (random field) variables

Parameter	Value
Number of Eigenvalues	100
Random Field Variance	1
Correlation Length (mm/in)	600
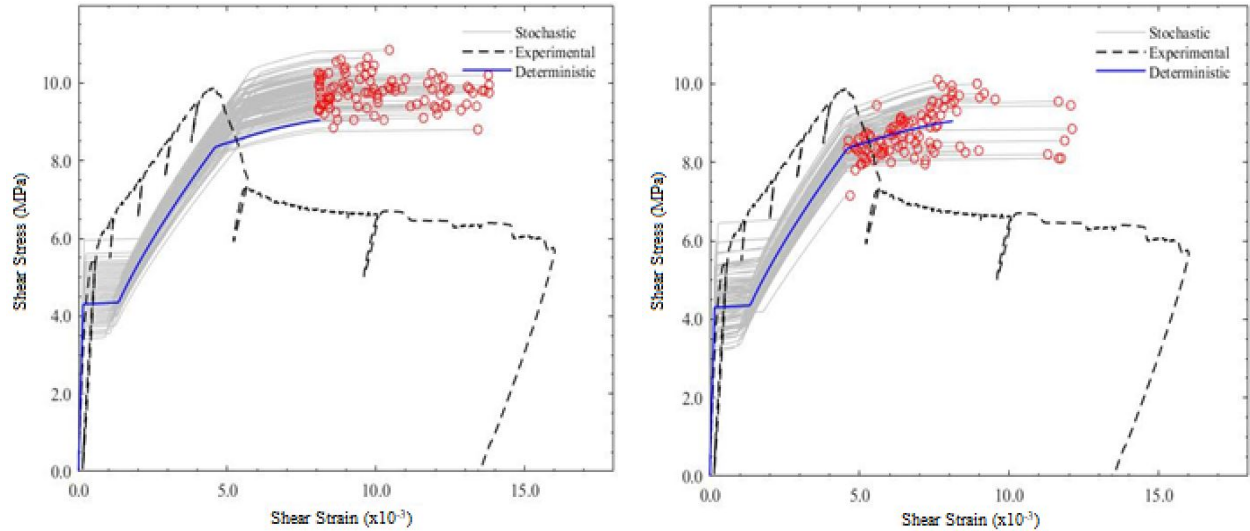
(a) Monte Carlo sampling.

(b) Monte Carlo sampling with spatially correlated (random field) variables.

Figure 3.10: Stochastic simulation of YS1.

Both the stochastic and deterministic simulations well capture the initial stiffness prior to cracking of the panel. However, post-cracking, the stochastic results showed considerable variability in the calculated shear stress-strain response. The simulations also showed significant variability in the failure stress and failure strain of the panel, as indicated by the circular data points for each trail. Despite consideration of the variability in material properties, the finite element simulation results still deviate substantially from the experimental results. When comparing the Monte Carlo sampling with the random field, local variability had little to no effect on the ultimate load and failure pattern for YS1. This is consistent with the results from Hunter (2016).

Chapter 4

Model Improvements for UHPFRC

This chapter describes the formulation improvements made to VecTor2 to enhance its capabilities in predicting the response of UHPFRC elements. These formulation changes were the result of the findings from Chapter 3 and included modifications to the aggregate modelling and maximum crack width calculations. In addition, the fibre reinforced concrete (FRC) tension models SDEM and VEM were validated for their performance in VecTor2. The following sections describe the improvements and their effect on the constitutive relationships of the MCFT and DSFM. Verification studies for these improvements are provided in Chapter 6.

4.1   Improvements to Aggregate Modelling

In conventional reinforced concrete, it is commonly observed that concrete mixes containing coarser aggregate sizes have higher shear resistance due to increases in aggregate interlock. However, due to the difference in thermal and mechanical properties between aggregates and the cement paste, shear and tensile stresses may develop and result in micro-cracking at the interface zone. In the initial development of ultra-high performance concrete, Richard and Cheyrezy (1995) found that using fine quartz sand instead of coarse aggregates significantly reduced micro-cracking from external loads and autogenous shrinkage. Decreasing the aggregate size also enhanced the homogeneity in the cementitious matrix and produced better workability. In addition, smaller aggregate sizes caused less frequent disturbances to the bond between fibres and the concrete matrix, thereby improving the effective fibre bridging effect (Dinh, 2010). As such, the coarsest aggregate size used in current UHPFRC mixtures generally lies between 0.5 and 4 mm, with most being fine sand with a maximum diameter of less than 1 mm.

Through the preliminary studies in Chapter 3, it was determined that the VecTor2-calculated behaviour for Panel YS1 was highly dependent on the aggregate size, a. In the comparison of four different aggregate sizes, larger aggregate sizes produced results that were closer to the experimental results. In addition, since the crack spacing formulation in VecTor2 is dependent on aggregate size, a smaller aggregate size resulted in significantly smaller crack spacing, which then produced poor estimates of shear strength. This is largely due to current models not considering the

enhanced mechanical behaviour of UHPFRC due to smaller aggregate sizes, such as the improved fibre bridging effect. In addition, it was hypothesized that the presence of fibres also provides the crack surface with sufficient roughness to compensate for the reduction in aggregate size. As such, based on the preliminary results of YS1, an effective aggregate size dependent on fibre properties was proposed and implemented. The proposed effective aggregate size, $a_{g,eff}$ (mm), formulation is as follows:

$$a_{g,eff} = \sum_{i=1}^{n} \frac{V_{f,i}}{0.02} \frac{l_{f,i}}{2} \tag{4.1}$$

where V_f and l_f are the volume fraction and length in mm of the ith fibre reinforcement, respectively.

To prevent this proposed aggregate size formulation from overestimating the improved effects of fibres on UHPFRC mechanical behaviour, there also exists a maximum limit on the effective aggregate size, $a_{g,eff,max}$ (mm), taken as the minimum of half the fibre length or 10 mm:

$$a_{g,eff} \leq a_{g,eff,max} \tag{4.2}$$

$$a_{g,eff,max} = min(\frac{l_f}{2}, 10\,mm) \tag{4.3}$$

The aggregate size, a (mm), to be used in the MCFT and DSFM is then taken as the maximum of the effective aggregate size calculated from Equations 4.1 to 4.3 and the user-specified maximum aggregate size:

$$a = max(a_{g,eff}, input) \tag{4.4}$$

For both conventional concrete and fibre reinforced concrete with unknown aggregate size, the default value in VecTor2 is 10 mm.

In the MCFT and DSFM, the aggregate size affects the constitutive relationships and the overall predicted behaviour of a member through its influence on a variety of different mechanisms, such as in computing the crack spacing and crack width, maximum local shear stress on the crack, as well as fracture energy.

4.1.1   Crack Spacing

The main parameter influenced by the implementation of an effective aggregate size is the computation of crack spacing. Since crack width is typically a function of crack spacing,

modifications to aggregate modelling can significantly change the response of modelled specimens. After cracking, the concrete elongates by the formation of new cracks and the widening of existing cracks. Ignoring the small elastic strain in the concrete between the cracks, the average crack width, $w_{cr,avg}$ (mm), can be taken as the product of the principal concrete tensile strain, ε_{c1}, and the average crack spacing, s_{cr}, in mm (Collins and Mitchell, 1997):

$$w_{cr,avg} = s_{cr}\varepsilon_{c1} \tag{4.5}$$

In VecTor2, The default crack spacing formulation for fibre reinforced concrete was developed by Deluce et al. (2014) and is based on the CEB-FIP 1978 mean crack spacing formulation. This model considers the effects of various fibre and conventional reinforcement properties on stabilized mean crack spacing. Under biaxial conditions, the mean crack spacing with respect to the principal axis, s_{cr} (mm), is calculated as:

$$s_{cr} = 2\left(c_a + \frac{s_b}{10}\right)k_3 + \frac{k_1 k_2}{s_m} \tag{4.6}$$

where:

c_a is the effective concrete cover, in mm, taken as $c_a = 1.5a$, where a is the aggregate size and $10 \leq c_a \leq 40$;

k_1 accounts for the bond characteristics of the reinforcing bar, and is taken as 0.4 for deformed bars and 0.8 for plain bars or prestressing tendons;

k_2 accounts for the strain conditions in the concrete member, and is taken as 0.25 for uniaxial strain conditions. For all other strain conditions, $k_2 = 0.25(\varepsilon_1 + \varepsilon_2)\,/\,\varepsilon_1$, where ε_1 and ε_2 are the maximum and minimum values of tensile strains in the concrete, respectively.

k_3 is the fibre content factor, calculated as:

$$k_3 = 1 - \frac{min(V_f, 0.015)}{0.015}\left(1 - \frac{1}{k_f}\right) \tag{4.7}$$

where the fibre volume fraction, V_f, is limited to a maximum value of 0.015 to consider the effect of fibre saturation on tensile behaviour; k_f is a factor accounting for fibre effectiveness due to its aspect ratio, and is calculated as $k_f = l_f \,/\, (50d_f) \geq 1.0$. l_f and d_f are the fibre length in mm and

fibre diameter in mm, respectively.

s_b is the effective longitudinal bar spacing, in mm, calculated as:

$$s_b = \frac{1}{\sqrt{\sum_i \frac{4}{\pi} \frac{\rho_{s,i}}{d_{b,i}^2} \cos^4 \theta_i}} \leq 15 d_b \tag{4.8}$$

where $\rho_{s,i}$, $d_{s,i}$, and θ_i are the reinforcement ratio, bar diameter in mm, and orientation in degrees of the ith reinforcement, respectively.

s_m is the reinforcement effective parameter, calculated as:

$$s_m = \sum_i \frac{\rho_{s,i}}{d_{b,i}} \cos^2 \theta_i + k_f \frac{\alpha_f V_f}{d_f} \tag{4.9}$$

where α_f is the fibre orientation factor, taken as 0.5 for random three-dimensional orientation of fibres.

4.1.2 Crack Width Check

One fundamental assumption in the MCFT is that an element under plane stress monotonic loading can be modelled as having a single crack direction which rotates as the material state or loading condition changes. This rotating crack model represents the formation of new cracks through the gradual change in the orientation of the principal stresses and strains. The average angle of the crack changes as new cracks form inclined to the initial cracks while remaining perpendicular to the direction of the principal tension. However, in elements where cracks rotate by a large amount, such as in elements with significantly different reinforcements in the x- and y-directions, there is a tendency for the rotating crack model to overestimate ductility in the concrete. As a result, a crack width check exists to account for the concrete's inability to transmit compressive stresses across large crack widths. This limit was first introduced in the analysis of shear-critical reinforced concrete beams having little or no shear reinforcement (Vecchio, 2000). These beams exhibited a dominant shear crack of considerable width at failure, and it was determined that when the crack widths exceeded a specific value, local compressive stresses were unlikely to be transmitted across the crack. Thus, reducing the average compressive stress at large crack widths provided more accurate predictions of the load-deformation response.

In VecTor2, the crack width check is implemented by a specific crack width limit, w_{lim} (mm),

past which there is a reduction of the average compressive stresses in the element. This limiting crack width can be selected to be a variety of different values. The default limit is related to the maximum aggregate size, a in mm, and is calculated as:

$$w_{lim} = \frac{a}{2.5} \tag{4.10}$$

For crack widths exceeding w_{lim}, the average concrete compressive stress computed from the stress-strain response, f_{cr}^* (MPa), is reduced by a crack coefficient, β_{cr}:

$$f_{c2} = \beta_{cr} f_{c2}^* \tag{4.11}$$

$$\beta_{cr} = \begin{cases} 1 & for \quad w_{cr} < w_{lim} \\ 1 - \frac{w_{cr} - w_{lim}}{3} \geq 0 & for \quad w_{cr} \geq w_{lim} \end{cases} \tag{4.12}$$

Although this limit also exists in the DSFM, it is not as important as with the MCFT, since the DSFM inherently limits the ability for cracks to rotate.

4.1.3 Maximum Crack Shear and Crack Slip

The maximum aggregate size in VecTor2 also affects concrete stress-strain behaviour through its influence on the maximum local shear stress on a crack in the MCFT and the crack slip calculations in the DSFM. The MCFT treats concrete as a new orthotropic material with uniformly distributed cracks. The strains and compatibility requirements in cracked concrete are taken as the average strains over the entire specimen. Average stresses in the concrete are then related to these strains using smeared-crack constitutive models in the principal direction. In addition, one main feature of the MCFT is the consideration of local stresses and strains at the crack. In general, concrete tensile stresses will be zero at the crack and higher than average between the cracks. To transfer concrete tensile stresses across the crack, local tensile stresses in the reinforcement will be higher than the average reinforcement stresses. As shown in Figure 4.1, the reinforcement generally crosses the crack at a skewed angle. Thus, with local increases in reinforcement stresses, equilibrium of average and local stresses results in shear stresses on the crack, v_{ci} (MPa).

In the MCFT, local shear stresses can be so large that slip on the crack occurs, particularly for lightly reinforced elements subjected to shear. Thus, it is important to check that the local shear
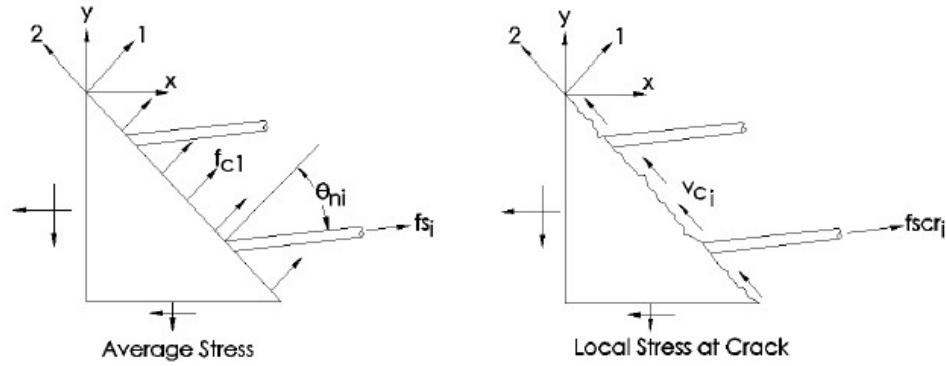
Figure 4.1: Comparison of average and local stresses at a crack.

stress across the crack, v_{ci}, does not exceed a specific limit, v_{cimax}. This maximum shear stress limit is affected by aggregate interlock, which decreases in efficacy as the crack width, w, increases and as the maximum aggregate size, a, decreases. The maximum shear stress across a crack check in the MCFT is based on the analysis of aggregate interlock by Walraven (1981), and is calculated as follows:

$$v_{ci} \leq v_{cimax} \tag{4.13}$$

$$v_{cimax} = \frac{0.18\sqrt{f'_c}}{0.31 + \frac{24w}{a+16}} \tag{4.14}$$

where f'_c and v_{cimax} are in MPa; a and w are in mm.

If the maximum shear stress at a crack is exceeded, the strain state of the element is modified to result in a lower average concrete tensile stress, f_{c1}, until Equation 4.13 is satisfied. Thus, modifying the effective aggregate size in the MCFT only affects the calculation of average concrete tensile stress since the MCFT does not consider shear slip on the crack in determining the deformation of the structure.

The DSFM is an extension of the MCFT and addresses some of its systematic weaknesses, such as its tendency to overestimate shear stiffness and strength of elements where crack shear slip is significant. The DSFM expands the compatibility relationships of the MCFT by explicitly incorporating a calculation for deformations due to crack shear slip. Modelling the crack shear slip deformation can significantly affect the computed stiffness and ductility of the structure, as well as the collinearity of stresses and strains. In addition, the check for maximum shear stress across

the crack required by the MCFT in Equation 4.13 is eliminated. Thus, the tensile stress, f_{c1}, in the DSFM is not subjected to the limitation of shear stresses at a crack in the same way as in the MCFT.

Several constitutive models have been developed for calculating slip, many of which are affected by the proposed change in maximum aggregate size formulation through crack spacing and crack width. The default crack slip model used in VecTor2 is the Walraven (1981) formulation. This formulation for crack slip, δ_s (mm), is related to the magnitude of shear stress on crack, v_{ci} in mm, and the crack width, w in mm:

$$\delta_s = \frac{v_{ci}}{1.8w^{-0.8} + (0.234w^{-0.707} - 0.20)f_{cc}} \tag{4.15}$$

where f_{cc} is the concrete cubic strength, in MPa, taken as approximately $1.20f_c'$.

The Lai-Vecchio (2004) formulation is another option for calculating crack slip in VecTor2. This model is affected by the maximum shear stress at a crack, v_{cimax}, and is thus also affected by the proposed change in maximum aggregate size. It is based on the Walraven (1981) model but provides better correlation in some cases.

The Lai-Vecchio (2004) model calculates the crack slip, δ_s, as:

$$\delta_s = \delta_2\sqrt{\frac{\psi}{1 - \psi}} \tag{4.16}$$

$$\delta_2 = \frac{0.5v_{cimax} + v_{c0}}{1.8w^{-0.8} + (0.234w^{-0.707} - 0.20)f_{cc}} \tag{4.17}$$

where $\psi = v_{ci} \, / \, v_{cimax}$, and $v_{c0} = f_{cc} \, / \, 30$ MPa.

The effective slip shear strain, γ_s, can then be computed by dividing the crack slip, δ_s in mm, by the average crack spacing, s_{cr} in mm, from Equation 4.6:

$$\gamma_s = \frac{\delta_s}{s_{cr}} \tag{4.18}$$

This average slip shear strain is then used to compute the total element strain.

4.1.4   Fracture Energy and Tension Softening

Lastly, the maximum aggregate size in VecTor2 affects concrete stress-strain behaviour through its influence on fracture energy. Since concrete is not perfectly brittle, fracture mechanics is typically used to describe the formation of localized cracks. As cracks widen, the concrete near the vicinity of the crack releases stress and this dissipated energy then propagates the crack tip. As illustrated in Figure 4.2, the presence of post-crack tensile stresses in the concrete is known as tension softening, which is commonly defined as a function of fracture energy. In structures exhibiting brittle fracture, tension softening effects can be crucial in modelling the stress redistributions and localization of damage. By including the tension softening response, the load-deformation and ductility of a member are more accurately predicted.
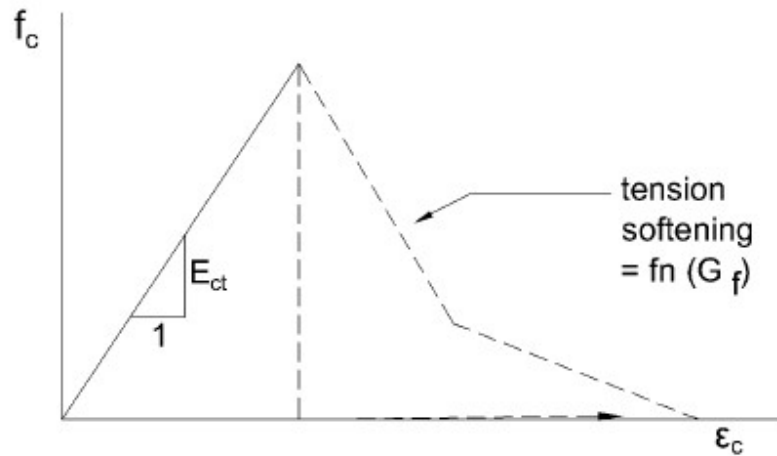
Figure 4.2: Tension softening response.

The fracture energy is the energy required to open a unit area of crack surface. It is a material property independent of size but dependent on maximum aggregate size; the concrete fracture energy increases with increasing maximum aggregate size and is the lowest for pure hardened cement paste. In VecTor2, the fracture energy, G_f (N/mm), is estimated according to Bazant (2002):

$$G_f = \frac{2.5 * 1.44(\frac{f_c'}{0.051})^{0.46}(1 + \frac{a}{11.27})^{0.22}0.35^{-0.30}}{1000} \tag{4.19}$$

where f_c' is in MPa, and a is in mm.

This fracture energy in turn influences tension softening behaviour, which is dependent on the selected descending post-cracking average tensile stress-strain curve. The default model in VecTor2

is the nonlinear (Hordijk) tension softening model, which calculates the average concrete tensile stress due to tension softening, f_{c1}^b (MPa), as:

$$f_{c1}^b = f_t' \left[\left(1 + \left(C_1 \frac{w_{crx}}{w_{ult}} \right)^3 \right) \exp \left(-C_2 \frac{w_{crx}}{w_{ult}} \right) - \frac{w_{crx}}{w_{ult}} (1 + C_1^3) \exp \left(-C_2 \right) \right] \qquad (4.20)$$

where f_t' is the concrete cracking stress in MPa, $C_1 = 3$, $C_2 = 6.93$, w_{crx} is the crack width in mm, and $w_{ult} = \frac{5.136 G_f}{f_t'}$.

In Chapter 3, as well as noted in Yap (2020), both the SDEM and VEM responses presented a large horizontal plateau after cracking that was not observed in the experimental response. To resolve this discrepancy, a slight adjustment was made to the value of w_{crx} used in equation 4.20. Previously, this value was incorrectly taken as the combined width of all cracks (i.e., $w_{crx} = w_{cr,avg} * number\ of\ cracks$). Instead this value was adjusted to be the average width of a single crack calculated from Equation 4.5 (i,e., $w_{crx} = w_{cr,avg}$). As shown in Figure 4.3, this adjustment resulted in the elimination of the plateau observed in both the SDEM and VEM calculated shear stress-strain responses for Panel YS1; both the SDEM and VEM presented a smooth transition between the uncracked and cracked response, more closely matching the experimental results. Similar improvements were noted in all five shear panels. This modification only resulted in the elimination of the plateau and did not affect the panels' ultimate strength or deformation capacities.

To capture this change for other tension softening formulations, such as the linear and bilinear tension softening models, an adjustment was made to the modified fracture energy value used in these models. Originally, this modified fracture energy, G_{f2} (N/mm), was a function of the element size. Instead, the modified fracture energy was adjusted to be a function of crack spacing, s_{cr}:

$$G_{f2} = \begin{cases} \frac{G_f}{s_{cr}} \frac{f_t'}{0.33 \sqrt{f_c'}} & for \quad f_t' \leq 0.33 \sqrt{f_c'} \\ \frac{G_f}{s_{cr}} & for \quad f_t' > 0.33 \sqrt{f_c'} \end{cases} \qquad (4.21)$$

where f_t' is in MPa, and s_{cr} is in mm.

Finally, the average post-cracking principal tensile stress in the concrete, f_{c1} (MPa), is taken as the larger of the tensile stress predicted by tension stiffening, f_{c1}^a, and the tensile stress predicted by tension softening, f_{c1}^b:

$$f_{c1} = max(f_{c1}^a, f_{c1}^b) \qquad (4.22)$$

(a) SDEM response.

(b) VEM response.
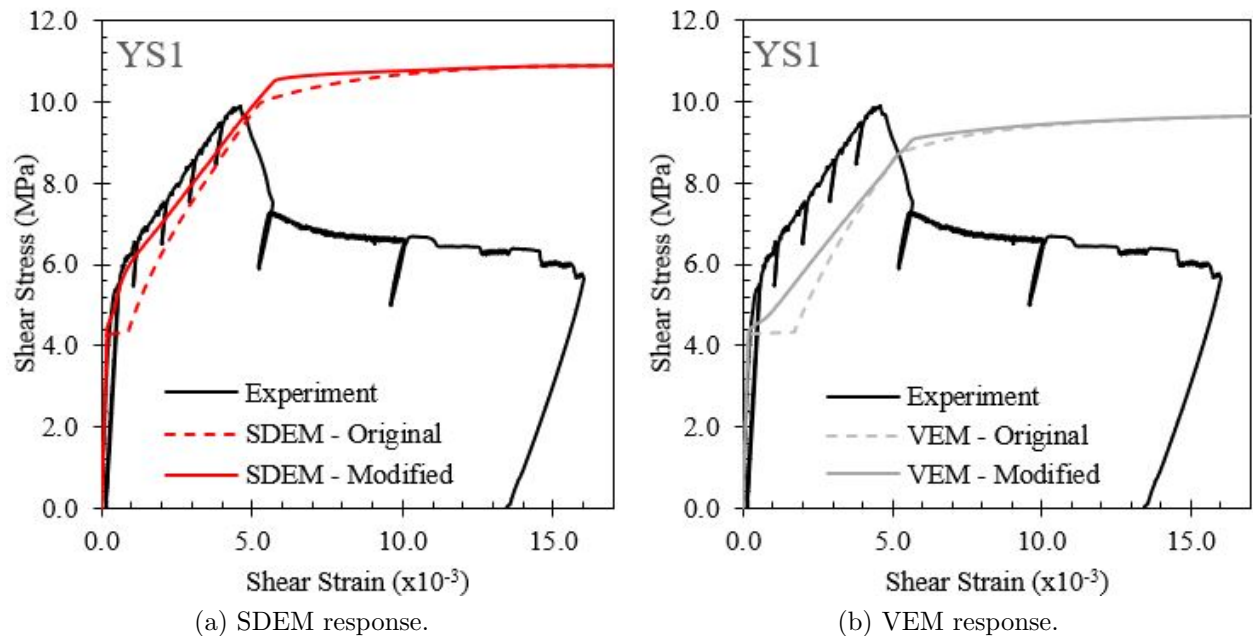
Figure 4.3: Comparison between VecTor2 original and modified shear stress-strain responses for Panel YS1.

4.2 Improvements to Crack Width Calculations

It is well known that the inclusion of random, discontinuous fibres significantly improves the cracking ability and tensile behaviour of concrete materials. The addition of fibres produces many favourable characteristics, such as reducing crack widths, crack spacing, and improving the overall deformation capacity of the member. This is the result of the fibres' ability to bridge and transmit tensile stresses across cracks, thereby enhancing the concrete energy-absorbing mechanisms and significantly improving the post-cracking tensile behaviour. In SFRC members with conventional longitudinal reinforcement, fibres also reduce the strains in the reinforcing bars and enhance the overall tension stiffening effects (Fischer and Li, 2002).

When loaded under uniaxial tension, SFRC typically displays a strain-softening behaviour, where the response is controlled by the localization of a single dominant crack. After cracking, the specimen's residual tensile stress never reaches the tensile strength, and instead, gradually reduces to zero. Deluce (2011) conducted a comprehensive experimental program to study the cracking and tension stiffening behaviour in SFRC containing conventional reinforcement. It was confirmed that the addition of steel fibres indeed decreases both the crack spacing and crack width of the tested specimens. Deluce also found that the post-yield localization of deformations at the cracks was more pronounced in SFRC than in the conventional reinforced concrete specimens. Deluce

concluded that once the crack width exceeded a certain threshold, crack localization occurred; the fibres began to pull out, and the fibre bridging phenomenon diminished, making the weakest section of the specimen even weaker.

Since structural members will typically fail at the location of the largest crack, a maximum crack width calculation was presumed necessary to determine the resistance of a section. In conventional reinforced concrete, there exists a characteristic crack width, w_k, which describes the crack width that only 5% of the cracks will exceed. The CEB-FIP estimates this characteristic crack width as 1.7 times the average crack width (CEB-FIP, 1978). Deluce et al. (2014) concluded however, that due to crack localization, the ratio of maximum crack width to average crack width ($w_{cr,max}$ / $w_{cr,avg}$) for fibre reinforced concrete is larger than that of conventional reinforced concrete. In addition, for a given strain, the fibre volume fraction, V_f, and the fibre aspect ratio, l_f / d_f, also influenced the maximum crack width value; as fibre volume fraction or aspect ratio increases, the ratio of maximum to average crack width also increases. Thus, in VecTor2 the maximum crack width, $w_{cr,max}$ (mm), for fibrous concrete is calculated as:

$$w_{cr,max} = \left(1.7 + 3.4\frac{V_f l_f}{d_f}\right) w_{cr,avg} \tag{4.23}$$

On the other hand, UHPFRC typically displays strain-hardening behaviour under uniaxial tension. In contrast to strain-softening materials, where crack localization occurs immediately after cracking, the tensile stress in strain-hardening materials continues to increase after cracking through the formation of multiple close-spaced narrow cracks (Naaman, 2008). As shown in Figure 4.4, the softening behaviour associated with crack localization and fibre pullout occurs only after significant tensile straining.

In VecTor2, the tensile stress response of fibre reinforced concrete members is calculated as the summation of the tensile stress attained by the fibres, and the tensile stress attained by the concrete matrix. The tensile stress provided by the fibres, f_f (MPa), is taken as the minimum of the fibre tensile stress calculated at the average crack width, $f_{f,w_{cr,avg}}$, and the maximum crack width, $f_{f,w_{cr,max}}$:

$$f_f = min(f_{f,w_{cr,avg}}, f_{f,w_{cr,max}}) \tag{4.24}$$

Since there is less tendency for cracks to localize for strain-hardening materials, the maximum crack limit introduced by Deluce et al. (2014) may unnecessarily limit the tensile stress attained by the
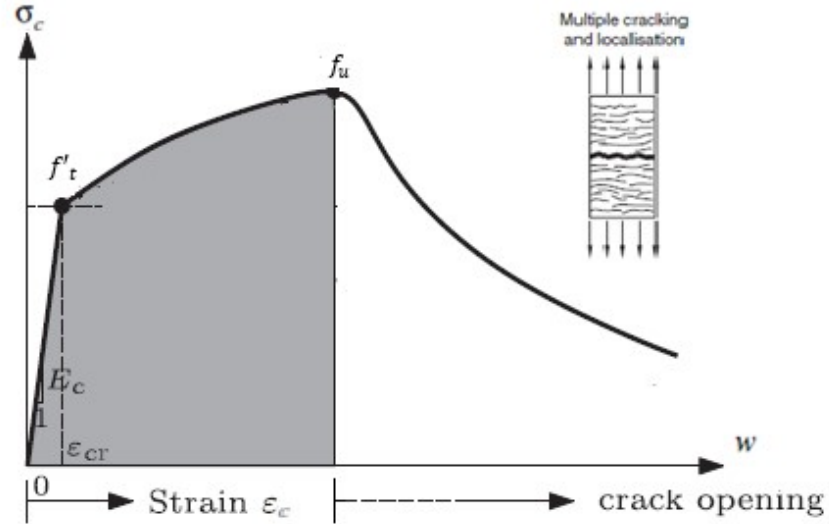
Figure 4.4: Stress-strain relationship of strain-hardening UHPFRC (Wille et al. 2014).

fibres, and consequently, also limit the tensile stress of the member. Thus, for strain-hardening materials such as UHPFRC, it was proposed that the maximum crack width be reverted to 1.7 times the average crack width ($w_{cr,max} = 1.7w_{cr,avg}$). The maximum crack width for fibre reinforced concrete in VecTor2 is then calculated as:

$$w_{cr,max} = \begin{cases} 1.7w_{cr,avg} & for \quad strain - hardening\,material \\ \left(1.7 + 3.4\frac{V_f l_f}{d_f}\right)w_{cr,avg} & for \quad strain - softening\,material \end{cases} \tag{4.25}$$

Currently, a strain-hardening UHPFRC material in VecTor2 is defined as any fibre reinforced concrete with a compressive strength, f'_c, of greater than 120 MPa.

4.2.1 Fibre Tensile Stress

This change in maximum crack width calculation significantly affects the computation of the contribution of steel fibre reinforcement to concrete tensile strength. In VecTor2, several models are available for calculating the contribution of steel fibre reinforcement to concrete tensile strength. The default model is the Simplified Diverse Embedment Model (SDEM) for monotonic loading conditions. The SDEM is considered to provide an accurate estimate of fibre stress since it considers various fibre mechanisms on tensile stress, such as the effect of fibre frictional bond behaviour and mechanical anchorage effects.

For both end-hooked and straight fibres, the fibre tensile stress attained by the frictional bond between the embedded fibres and the concrete, f_{st} (MPa), is calculated as:

$$f_{st} = \alpha_f V_f K_{st} \tau_{f,max} \frac{l_f}{d_f} \left(1 - \frac{2w_{cr}}{l_f}\right)^2 \tag{4.26}$$

$$K_{st} = \begin{cases} \frac{\beta_f}{3}\frac{w_{cr}}{s_f} & for \quad w_{cr} \leq s_f \\ 1 - \sqrt{\frac{s_f}{w_{cr}}} + \frac{\beta_f}{3}\sqrt{\frac{s_f}{w_{cr}}} & for \quad w_{cr} > s_f \end{cases} \tag{4.27}$$

$$\tau_{f,max} = 0.396\sqrt{f_c'} \tag{4.28}$$

where $\alpha_f = 0.5$, s_f is the slip corresponding to the full bond strength, taken as 0.01, $\beta_f = 0.6$, and w_{cr} is the crack width in mm. $\tau_{f,max}$ and f_c' are in MPa.

For end-hooked fibres, additional stress is attained through the mechanical anchorage of the hooked ends. This additional stress, f_{eh} (MPa), is calculated as:

$$f_{eh} = \alpha_f V_f K_{eh} \tau_{eh,max} \frac{2(l_f - 2w_{cr})}{d_f} \tag{4.29}$$

$$K_{st} = \begin{cases} \beta_{eh}\left[\frac{2}{3}\frac{w_{cr}}{s_f} - \frac{1}{5}\left(\frac{w_{cr}}{s_f}\right)^2\right] & for & w_{cr} \leq s_{eh} \\ 1 + \left(\frac{7\beta_{eh}}{15} - 1\right)\sqrt{\frac{s_{eh}}{w_{cr}}} - \frac{2(\sqrt{w_{cr}} - \sqrt{s_{eh}})^2}{l_f - l_i} & for & s_{eh} < w_{cr} \leq \frac{l_f - l_i}{2} \\ \left(\frac{l_i - 2w_{cr}}{2l_i - l_f}\right)^2 K_{eh,i} & for & \frac{l_f - l_i}{2} \leq w_{cr} < \frac{l_i}{2} \end{cases} \tag{4.30}$$

$$\tau_{eh,max} = 0.429\sqrt{f_c'} \tag{4.31}$$

where l_i is the distance between mechanical anchorages for end-hooked fibres, in mm, $K_{eh,i}$ is K_{eh} at $w_{cr} = (l_f - l_i)2$, $\beta_{eh} = 0.8$, and $s_{eh} = 0.1$.

The tensile stress attained by steel fibres, f_f (MPa), can then be calculated for the two different types of steel fibres:

$$f_f = \begin{cases} f_{st} & for & straight\ fibres \\ f_{st} + f_{eh} & for & end-hooked\ fibres \end{cases} \tag{4.32}$$

Lastly, to obtain the tensile stress of the fibre reinforced member at a given crack width, the tensile stress attained by the fibres is then added to the tensile stress due to the tension-softening effect

of the concrete matrix, f_{ct} (MPa):

$$f_{SFRC} = f_f + f_{ct} \tag{4.33}$$

$$f_{ct} = f_{cr} \exp(-cw_{cr}) \tag{4.34}$$

where f_{cr} is the cracking stress in MPa, the coefficient c is taken as 15 and 30 for concrete and mortar, respectively, and w_{cr} is in mm.

4.3 Verification of FRC Tension Models

One critical component of this thesis was in validating the accuracy of current model implementations in VecTor2 for analyzing fibre reinforced concrete. Specifically, the SDEM and VEM fibre tension models used in calculating the tensile stress contribution from fibres were investigated and verified for their performance in VecTor2. This was done for each FRC tension model by comparing the tensile stress to crack width response of a uniaxial tension member modelled in VecTor2 against the response from hand calculations.

4.3.1 The Simplified Diverse Embedment Model (SDEM)

To validate the accuracy of the SDEM implementation, the material properties of Panel C1V1F1 from a series of SFRC shear panels tested by Susetyo (2009) were used to model a uniaxial tension member in VecTor2. The SDEM was selected as the FRC tension model; all other constitutive models used were VecTor2 default models. The tensile stress of the member, f_{SFRC}, was calculated according to the formulations specified by the SDEM (Lee et al., 2013a) in Equations 4.25 to 4.33.

The panel modelled contained 0.5% by volume of 50 mm long, 0.62 mm in diameter straight fibres. The ultimate tensile stress for the fibres was 1050 MPa. The compressive strength, f'_c, of the member was 50 MPa and the mean tensile strength was taken as 2.33 MPa based on the equation $f'_t = 0.33\sqrt{f'_c}$. The fibre bond strength was taken as 2.8 MPa based on the equation $\tau_{f,max} = 0.396\sqrt{f'_c}$, specified by the SDEM bond strength formulation for straight fibres (Lee et al., 2013a). Figure 4.5 shows that the resulting VecTor2 stress to crack width response correlated well with the hand-calculated response.
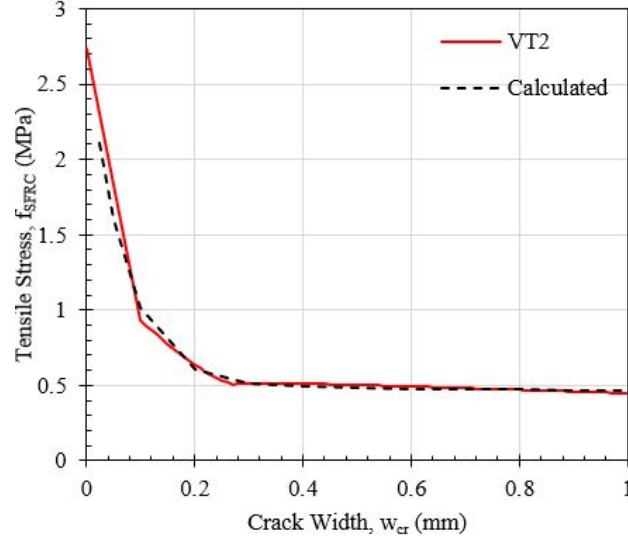
Figure 4.5: Comparison between VecTor2 and hand-calculated stress to crack width response using SDEM.

4.3.2 The Variable Engagement Model (VEM)

Similarly, to validate the accuracy of the VEM implementation in VecTor2, a uniaxial tension member was modelled using the VEM FRC tension model. The tensile stress attained by the fibres was computed using the VEM formulation specified in Voo and Foster (2003). Since the VEM did not specify a formulation for calculating the contribution of the concrete matrix to tensile stress, Equation 4.34 from the SDEM formulation was used. The VEM relates the tensile stress to the crack width with the following relationship:

$$f_f = K_f K_d \frac{l_f}{d_f} V_f \tau_b \tag{4.35}$$

$$K_f = \frac{tan^{-1}(w_{cr} / \alpha)}{\pi} \left(1 - \frac{2w_{cr}}{l_f} \right)^2 \tag{4.36}$$

$$\tau_b = \begin{cases} 2.5 f'_t & for & concrete\,with\,hooked-end\,fibres \\ 2.0 f'_t & for & concrete\,with\,straight\,fibres \\ 1.2 f'_t & for & mortar\,with\,hooked-end\,fibres \\ 1.0 f'_t & for & mortar\,with\,straight\,fibres \end{cases} \tag{4.37}$$

where $\alpha = d_f / 3.5$, w_{cr} is the crack width in mm, and K_d is a damage factor, taken as 1.0 for concrete containing a conventional volume of fibres. d_f and l_f are in mm while f'_t and τ_b are in MPa.

The concrete and fibre material properties were taken from a beam within an experimental series tested by Voo et al. (2003). This beam contained 1.88% by volume of 13 mm long, 0.2 mm diameter straight fibres, and 0.62% of 30 mm long, 0.5 mm diameter end-hooked fibres. The ultimate tensile stress for the straight and end-hooked fibres were 1800 MPa and 1000 MPa, respectively. The compressive strength, f_c', of the member was 169 MPa and the mean tensile strength was taken as 7.8 MPa based on the equation $f_t' = 0.6\sqrt{f_c'}$ specified by Voo and Foster (2003).

The resulting stress to crack width relationship is shown in Figure 4.6a. In contrast to the SDEM, the VEM showed a significant divergence of results between the hand-calculated and the VecTor2 response. Upon further investigations, it was determined that the VEM formulation implemented in VecTor2 did not use the correct crack width in its algorithms. As a result, the tensile stress attained by the fibres was incorrectly calculated, resulting in the steep drop in tensile stress after cracking. Following the correct modifications to the formulations, the revised stress to crack width response is shown in Figure 4.6b. The corrected VecTor2 response correlated well with the hand-calculated response.
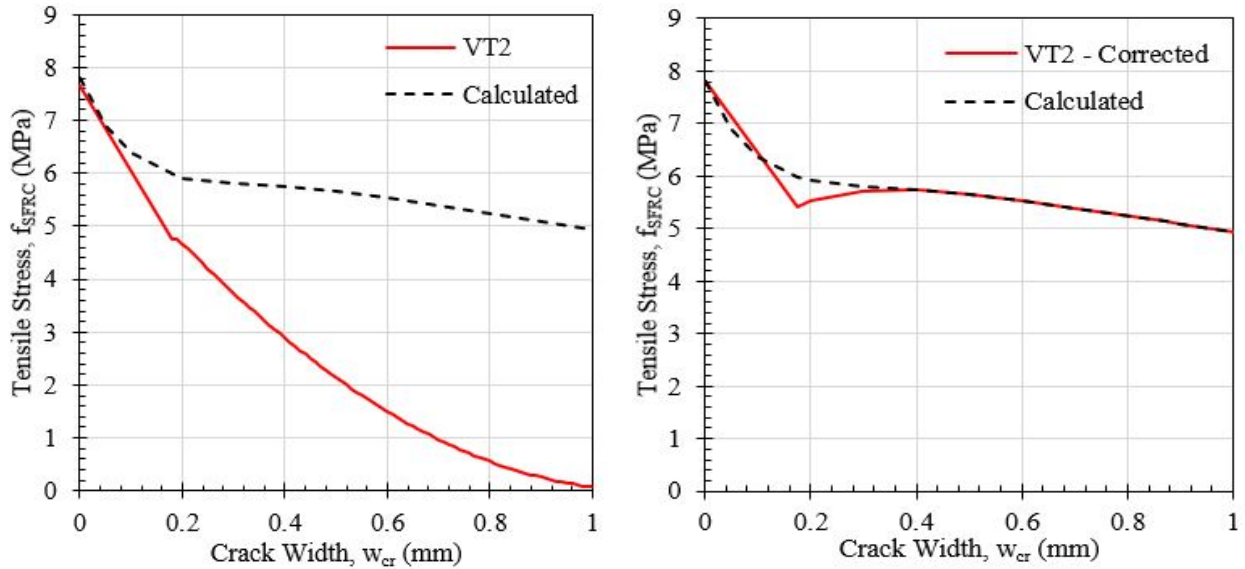
(a) VEM original response.　　　　　　　　(b) VEM corrected response.

Figure 4.6: Comparison between VecTor2 and hand-calculated stress to crack width response using VEM.

Chapter 5

Improvements to Rebar Rupture Models

5.1 Introduction

Reinforcement rupture was observed in UHPFRC shear panels YS1 and YS5 tested by Yap (2020). In nonlinear finite element analysis of UHPFRC members, this rupture must be captured to accurately predict the deformation capacity. A simplified reinforcement rupture model was derived from regression analysis and implemented into VecTor2 to capture the response of embedded reinforcement rupture for both reinforced concrete and fibre reinforced concrete with conventional reinforcing bars.

5.1.1 Tension Stiffening

In VecTor2, concrete in tension is categorized into the uncracked and cracked response. Prior to cracking, the tensile stress response is assumed to be linear-elastic and is calculated as $f_{c1} = E_{ct}\varepsilon_{c1}$, where E_{ct} is the concrete initial tangent modulus of elasticity and ε_{c1} is the net principal tensile strain. After cracking, the concrete tensile stresses diminish to zero at the crack surface, while the concrete between the cracks still attracts tensile stresses due to the bond between the concrete and reinforcing steel. As a result, there is an increased post-cracking stiffness of the concrete structure beyond the stiffness of the reinforcement; this mechanism is known as tension stiffening.

Tension stiffening in VecTor2 can be modelled using a post-cracking concrete stress-strain curve. Numerous models have been implemented to account for tension stiffening of bonded steel reinforcement. However, most models are focused on the behaviour prior to yielding of the reinforcement and do not directly predict reinforcement strain at rupture. After yielding, the contribution of concrete on tensile behaviour is typically ignored, and the computed tensile behaviour becomes the same as that of the bare steel bars. The ultimate stress and strain of the member become identical to those of the bare bar.

5.2 Lee Mechanics-Based Models

Lee et al. (2011b) showed that tension stiffening effects after yielding of the reinforcement can have a major effect on the ductility of reinforced concrete members subjected to direct tension. Figure 5.1a shows the average stress-strain relationship of a reinforced concrete member subjected to uniaxial tension up to failure, while Figure 5.1b shows the stress-strain relationship in only the concrete. After initial cracking, the concrete stresses decrease nonlinearly due to tension softening effects (line A-B). After yielding of the reinforcement at a crack (point B), the stresses in the concrete continue to reduce since the total strength capacity across the crack is assumed not to exceed the yield strength of the reinforcement (line B-C). After the average strain of the reinforcement reaches the yield strain and the average concrete tensile stress becomes zero (point C), the concrete tensile stress contribution is then typically ignored. However, average tensile stresses in the concrete still exist due to bond interaction between concrete and steel (line C-D). As such, the concrete member remains stiffer than the bare bar, and the average tensile strain of reinforced concrete member which results in reinforcement rupture is significantly less than that of the bare bar. The strain difference between a concrete-embedded bar and a bare bar (points E and D) illustrates the tension stiffening effect after yielding of the reinforcement. The Lee 2011 (w/ Post-Yield) tension stiffening model was developed to consider concrete stresses after yielding (line C -E) and provides a realistic representation of reinforced concrete ductility.

(a) Average member stress-strain.   (b) Average concrete stress-strain.
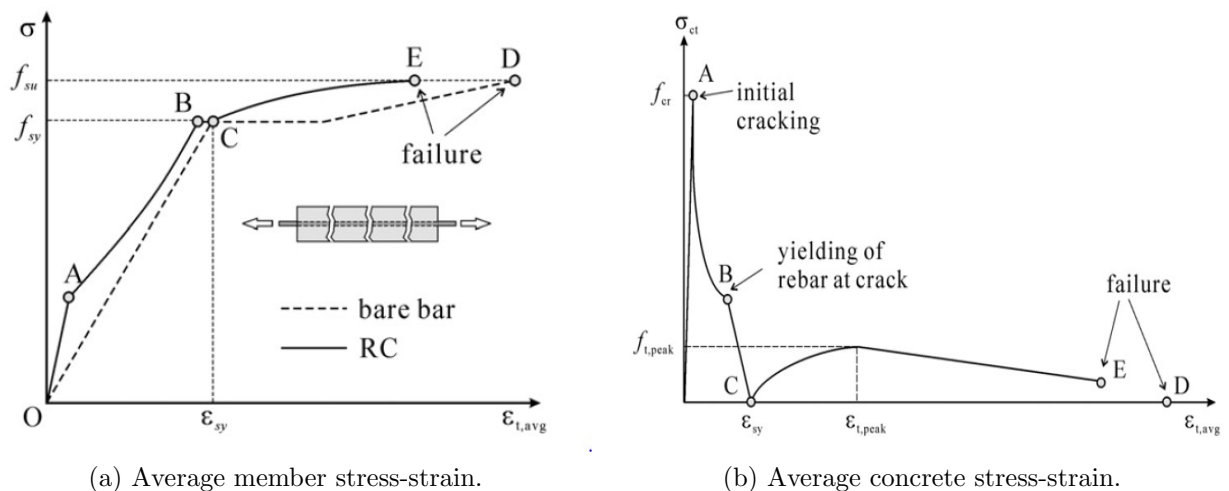
Figure 5.1: Stress-strain response of reinforced concrete member subjected to uniaxial tension up to failure.

5.2.1 Reinforcement Rupture Strain

The Lee 2011 (w/ Post-Yield) tension stiffening model in VecTor2 was developed based on a series of analytical parametric studies investigating factors that influence average concrete tensile stresses after reinforcement yielding. The parameters considered include concrete compressive strength, reinforcement yield strength, strain hardening strain, strain hardening modulus, reinforcement diameter, and reinforcement ratio. In the Lee 2011 model, as shown in Figure 5.1b, after the average strain of the reinforcement reaches the yield strain, the average tensile stress in the concrete increases from zero to a peak average tensile stress, $f_{ct,peak}$, then gradually diminishes again. A parabolic average tensile stress-strain relationship was assumed for pre-peak behaviour, and a linear relationship was assumed for post-peak behaviour. From the parametric study, it was determined that the peak average tensile stress in the concrete after yielding, $f_{ct,peak}$ (MPa), was affected by concrete compressive strength, f'_c (MPa), reinforcement diameter, d_b (mm), and reinforcement ratio, ρ_s:

$$f_{ct,peak} = a\sqrt{f'_c} \tag{5.1}$$

where $a = -0.0313\rho_s^{0.57}d_b + 3.3881\rho_s^{0.76}$.

The Lee 2011 (w/ Post-Yield) average tensile stress-strain relationship after yielding of the reinforcement is described with Equation 5.2:

$$f_{ct,avg} = \begin{cases} f_{ct,peak} - f_{ct,peak}\left(\frac{\varepsilon_{t,peak}-\varepsilon_{t,avg}}{\varepsilon_{t,peak}-\varepsilon_{sy}}\right)^2 & for \quad \varepsilon_{sy} \leq \varepsilon_{t,avg} \leq \varepsilon_{t,peak} \\ f_{ct,peak} - \frac{f_{ct,peak}-0.5f_{ct,peak,\rho_{min}}}{0.1-\varepsilon_{t,peak}}\left(\varepsilon_{t,avg}-\varepsilon_{t,peak}\right) \geq 0.5f_{ct,peak,\rho_{min}} & for \ \varepsilon_{t,avg} \geq \varepsilon_{t,peak} \end{cases} \tag{5.2}$$

where $\rho_{min} = \frac{\varepsilon_{cr}E_c}{f_{sy}-\varepsilon_{cr}E_s}$, and $\varepsilon_{t,peak} = 0.01 + 0.001\max(15-d_b,0) \geq \varepsilon_{sh}$.

The Lee 2011 model calculates reinforcement stresses at crack locations and determines the average strain conditions resulting in rupture of reinforcement. The steel stress at a crack, f_{scr} (MPa), is then calculated from force equilibrium conditions according to Equation 5.3:

$$f_{scr} = f_{s,avg} + \frac{f_{ct,avg}}{\rho_s} \tag{5.3}$$

where $f_{s,avg}$ and $f_{ct,avg}$, both in MPa, are the average tensile stress of the reinforcement and concrete, respectively.

Under the assumption that the steel stress-strain relationship after hardening strain is linear and

satisfying force equilibrium condition at the crack, the average tensile strain of reinforced concrete at reinforcement rupture is calculated as:

$$\varepsilon_{t,avg,rupt} = \frac{B - \sqrt{B^2 - 4AC}}{2A} \quad for \quad f_{su} \leq f_{scr,\varepsilon_{t,peak}} \tag{5.4}$$

$$\varepsilon_{t,avg,rupt} = \frac{\varepsilon_{sh}E_{sh} + f_{su} - f_{sy}\frac{0.5f_{ct,peak,\rho_{min}}}{\rho_s} - \varepsilon_{t,peak}K_E}{E_{sh} - K_E} \quad for \quad f_{scr,\varepsilon_{t,peak}} < f_{su} \leq f_{scr,0.1} \tag{5.5}$$

$$\varepsilon_{t,avg,rupt} = \varepsilon_{sh} + \frac{1}{E_{sh}}(f_{su} - f_{sy} - \frac{0.5f_{ct,peak,\rho_{min}}}{\rho_s} \quad for \quad f_{scr,0.1} \leq f_{su} \tag{5.6}$$

where:

$$A = \frac{f_{ct,peak}}{(\varepsilon_{t,peak} - \varepsilon_{sy})^2} \tag{5.7}$$

$$B = \rho_s E_{sh} + 2A\varepsilon_{t,peak}^2 \tag{5.8}$$

$$C = \rho_s(f_{su} - f_{sy} + E_{sh}\varepsilon_{sh}) - f_{ct,peak} + A\varepsilon_{t,peak}^2 \tag{5.9}$$

$$f_{scr,0.1} = f_{sy} + (0.1 - \varepsilon_{sh})E_{sh} + \frac{0.5f_{ct,peak,\rho_{min}}}{\rho_s} \tag{5.10}$$

$$K_E = \frac{1}{\rho_s}\frac{f_{ct,peak} - 0.5f_{ct,peak,\rho_{min}}}{0.1 - \varepsilon_{t,peak}} \tag{5.11}$$

5.2.2   Crack Stress Check

Local increases in reinforcement stresses will result in shear stresses on a crack. In general, calculation of the shear stress on a crack, v_{ci} (MPa), in VecTor2 is calculated as follows:

$$v_{ci} = \sum_{i=1}^{n} \rho_{s,i}(f_{scr,i} - f_{s,i})\cos\theta_{n,i}\sin\theta_{n,i} - (1 - \alpha_f)f_f\sin\theta_f \tag{5.12}$$

$$\tan\theta_f = \frac{\delta_s}{w_{cr}} \tag{5.13}$$

where i represents a layer of conventional reinforcement in a given direction; $\rho_{s,i}$ is the reinforcement ratio; $f_{scr,i}$ is the local reinforcement stress on a crack, in MPa; $f_{s,i}$ is the reinforcement stress, in MPa; and $\theta_{n,i}$ is the angle between the reinforcement direction and normal to the crack, in degrees. In fibre reinforced concrete α_f is the average fibre orientation factor; θ_f is the angle of the tensile

stress attained by the fibres from the axis perpendicular to the crack surface, in degrees; δ_s is the slip, in mm; and w_{cr} is the average crack width, in mm.

An advanced (Lee 2009) crack stress option is also available in VecTor2 which employs a bi-section method of convergence while using the same basic crack stress formulation. This advanced crack stress option will be investigated and validated in combination with the Lee 2011 reinforcement rupture model in Section 5.4.

5.2.3 Lee 2011 (w/ Post-Yield) Formulation Issues

Although the Lee 2011 model can predict reinforcement rupture, this model in VecTor2 shows slight inconsistencies in results. A single 100 x 100 x 100 mm element was modelled in VecTor2 using the Lee 2011 (w/ Post-Yield) tension stiffening model and all other VecTor2 default constitutive models. Figure 5.2 shows the effect of rebar diameter on embedded reinforcement rupture for three different concrete compressive strengths ($f'_c = 25, 40, 60$ MPa). The ratio of embedded steel rupture strain to bare bar rupture strain ($\varepsilon_{rupt,embed}/\varepsilon_{rupt,air}$) was employed for the comparison, with a constant bare bar rupture strain of 150 millistrain. Six different rebar diameters ($d_b = 10$, 13, 16, 19, 22, 25 mm) and 5 different reinforcing ratios ($\rho = 0.5\%, 1.0\%, 1.5\%, 2.0\%, 3.0\%$) were investigated. All reinforcement was modelled as smeared. The reinforcement yield strength and ultimate strengths were assumed to be 400 and 600 MPa, respectively. In general, as the reinforcing ratio increases, the rupture strain also increases, and as rebar diameter increases, rupture strain also increases. However, the effect of reinforcing bar diameter on rupture is not consistent. For example, with a concrete compressive strength of 25 MPa, the $\varepsilon_{rupt,embed}/\varepsilon_{rupt,air}$ ratio is the same for $d_b = 13, 16$, and 19 mm. Furthermore, with a concrete compressive strength of 25 MPa and a bar diameter of 25 mm, changing the reinforcement ratio from 1.5% to 2.0% does not affect rebar rupture strain, which is not consistent with the overall trend. Similar inconsistencies are present with other compressive strengths, which suggests that this model may require further optimization.
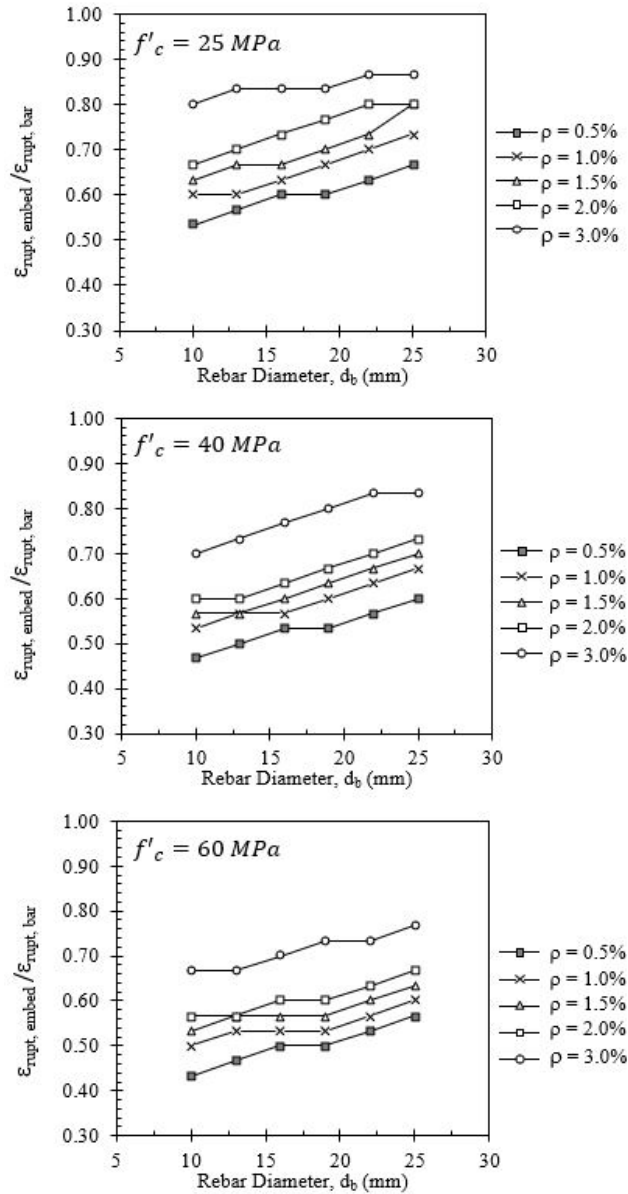
Figure 5.2: Effect of rebar diameter on embedded reinforcement rupture using Lee 2011 (w/ Post-Yield) model.

5.3   Formulation of Simplified Reinforcement Rupture Model

In response to the somewhat inconsistent results provided by the Lee 2011 (w/ Post-Yield) model and a lack of reinforcement rupture considered in other tension stiffening models, a simplified model for reinforcement rupture using regression analysis was proposed and combined with the default Modified Bentz 2005 formulation for tension stiffening.

5.3.1   Modified Bentz 2005

The default Modified Bentz 2005 (Bentz, 2005) model is a rigorous formulation that considers the effect of reinforcement percentage and bond characteristics on tension stiffening. The formulation for average tensile stress, f_{c1} (MPa), is:

$$f_{c1} = \frac{f'_t}{1 + \sqrt{c_t \varepsilon_{c1}}} \quad for \quad \varepsilon_{c1} \geq \varepsilon'_t \tag{5.14}$$

where $c_t = 3.6 t_d * m$, $t_d = 0.6$, $1/m = \sum_{i=1}^{n} 4\rho_i / d_{bi} * |\cos(\theta - \alpha_i)|$; ρ_i is the reinforcement ratio, d_{bi} is the rebar diameter in mm, θ is the inclination of the principal direction, and α_i is the inclination of the reinforcement.

This formulation was subsequently modified in VecTor2 to consider the contribution from fibre reinforcement (Lee et al., 2013b), and is as follows:

$$f_{c1} = \frac{f'_t}{1 + \sqrt{c_f * 3.6 * M\varepsilon_1}} \quad for \quad \varepsilon_{c1} \geq \varepsilon'_t \tag{5.15}$$

$$c_f = 0.6 + \frac{1}{0.034} \left(\frac{l_f}{d_f}\right) \frac{(100V_f)^{1.5}}{M^{0.8}} \quad for \quad end-hooked\ fibres \tag{5.16}$$

$$c_f = 0.6 + \frac{1}{0.058} \left(\frac{l_f}{d_f}\right)^{0.9} \frac{100V_f}{M^{0.8}} \quad for \quad straight\ fibres \tag{5.17}$$

$$M = \frac{A_c}{\sum d_b \pi} \tag{5.18}$$

where l_f is the fibre length, in mm, d_f is the fibre diameter, in mm, V_f is the fibre volume ratio. M is the bond parameter in mm, A_c is the cross-sectional area of the concrete matrix in mm^2, and d_b is the diameter of the reinforcement in mm.

However, the Modified Bentz 2005 model is limited by the yield of the reinforcement across a crack and does not directly predict reinforcement strain at rupture. As such, a formulation of a simplified reinforcement rupture model was developed using regression analysis and implemented into this model for tension stiffening.

5.3.2 Basics of a Regression Analysis

In statistical modelling, linear regression analysis is a linear approach used to mathematically determine the relationship between two sets of variables: the dependent variable, which is the factor to be predicted, and the independent variable, the factor suspected of having an impact on the dependent variable. Using an appropriate set of data, a linear relationship can be obtained between the dependent variable and the independent variable:

$$Y = bx + a + \varepsilon \tag{5.19}$$

where, Y represents the dependent variable of interest, x represents the independent variable, a is the y-intercept and a constant, b is a dimensional regression coefficient and the slope of the regression line, and ε is the random error term.

A linear regression using the least-squares method is the most common type of modelling method, where the unknown parameters are estimated by minimizing the sum of the squared deviations between the data and the model. The minimizing process produces a system of equations that can be solved to obtain an estimate of the unknown parameters in equation 5.19.

Regression analysis can be performed by Excel using the least-squares method to fit a line through a set of observations. The relevant outputs given with each analysis that determine the fit of the regression equation include the Correlation Coefficient, the Coefficient of Determination, the Standard Error, and residual plots. The Correlation Coefficient, commonly known as the "Multiple R", measures the strength of the linear relationship. The Multiple-R is a value between -1 and 1, and its absolute value indicates the strength of the relationship. A value of 1 suggests a strong positive relationship, while -1 suggests a strong negative relationship, and 0 suggests no relationship. The Coefficient of Determination, commonly known as the "R-squared", indicates the goodness of fit and is used to measure how well the regression model fits the data sample. An R-squared is a value between 0 and 1, and indicates the extent to which the dependent variable is predictable from the independent variable; a value closer to 1 signifies a better model fit. Lastly, the Significance F value is a measure of the reliability of the results and differentiates between a statistically significant regression analysis from a statistically insignificant analysis. In Excel, a Significance F value of less than 5% is considered reliable.

5.3.3 Experimental Specimens Used for Regression Analysis

Researchers Mayer and Eligehausen (1998), Moreno et al. (2014), Kang et al. (2017), and Nguyen et al. (2019) tested a total of eight normal strength reinforced concrete members under direct uniaxial tension until rupture of the reinforcement was achieved. These experimental specimens were used in the regression analysis to obtain a simplified numerical model for reinforcement rupture. Although Kang et al. (2017) tested five different normal concrete members, specimen NC-150-13/0.59 was omitted from the regression analysis as the unusually low rupture strain of 14 millistrain reported was inconsistent with other test results. In the absence of available experimental data on the rupture of reinforcement, these seven experimental specimens were assumed to be a representative sample of reinforcement rupture in the regression analysis. Further investigations and experimental data will be required to verify and calibrate the results of this regression analysis.

The details of each experimental set up can be found in Chapter 2. A summary of the specimens and their material properties is provided in Table 5.1. In the absence of reported data, the tensile strength and Young's modulus of concrete were assumed to be $f'_t = 0.33\sqrt{f'_c}$ and $E_c = 3300\sqrt{f'_c} + 6900$ MPa, respectively. The Young's modulus of reinforcement steel was assumed to be 200 000 MPa.

Table 5.1: Constitutive models used for panel YS1 finite element analysis

Author	Specimen ID	d_b mm	f'_c MPa	f'_t MPa	ρ %	f_y MPa	f_u MPa	$\varepsilon_{rupt,bar}$ x10^{-3}	$\varepsilon_{rupt,test}$ x10^{-3}
Mayer & Eligehausen (1998)	S4D16 - A	16	28.4	1.65	0.50	519	588	85	45
Moreno et al. (2014)	RC	16	44.0	1.40	1.25	440	620	140*	103
Kang et al. (2017)	NC-90-13/1.64	13	42.4	2.15	1.64	545	629	113	38
	NC-120-13/0.92	13	42.4	2.15	0.92	545	629	113	38
	NC-150-16/0.89	16	42.4	2.15	0.89	574	664	126	60
	NC-150-20/1.40	20	42.4	2.15	1.40	541	636	150	71
Nguyen et al. (2019)	R/C	16	42.0	2.14	0.64	440	620	140*	72

d_b = reinforcement diameter; f'_c = concrete compressive strength; f'_t = concrete tensile strength; ρ = longitudinal reinforcement ratio; f_y = reinforcement yield strength; f_u = reinforcement ultimate strength; $\varepsilon_{rupt,bar}$ = bare bar rupture strain; $\varepsilon_{rupt,test}$ = tested embedded bar rupture strain.
* Rupture strain not reported in test program. Value assumed from a typical US No. 5 A706 steel bar.

5.3.4 Regression Analysis

Multiple variables and combinations of variables were investigated in the regression analysis to identify which material properties affect the reinforcement rupture strain. The variables used included those in the parametric study conducted by Lee et al. (2011b), which include concrete

compressive strength, f_c', reinforcement yield strength, f_y, reinforcement ratio, ρ, and reinforcement diameter, d_b. Other parameters that could potentially influence rupture strain were also investigated, including reinforcement ultimate strength, f_u, and concrete tensile strength, f_t'. The dependent variable to be predicted was the ratio between the embedded reinforcement rupture strain and the bare bar rupture strain, $\varepsilon_{rupt,embed}$ / $\varepsilon_{rupt,bar}$.

The regression analysis was first performed using each single variable as the independent variable to be investigated. The relevant resulting outputs are listed in Table 5.2. Both f_c' and ρ produced low Multiple R and R-Squared values along with a high Significance F value, suggesting both a low degree of correlation between these variables and reinforcement rupture as well as low reliability of results. In contrast, d_b, f_y, and f_t' showed relatively high Multiple R and R-Squared values, suggesting these material properties may affect reinforcement rupture. Despite this, an R-Squared of 0.680 (68.0%) was still considerably low to be indicative of a good fit. As such, regression analysis was then performed using a combination of variables and the outputs are listed in Table 5.3. It was determined that using $d_b(f_u - f_y)/f_t'$ as the independent variable produces the best fit. A Multiple R of 0.824 indicates a good positive linear relationship, and an R-Squared of 0.794 signifies that 79.4% of the data fit the regression line. In addition, the low Significance F of 0.007 (0.7%) further suggests a reliable model based on the available sample observations.

Table 5.2: Regression analysis output using single variables as the independent variables

Independent Variable	f_c'	ρ	f_u	d_b	f_y	f_t'
Multiple R	0.068	0.210	0.256	0.442	0.702	0.824
R-Squared	0.005	0.044	0.066	0.195	0.493	0.680
Significance F	88.5%	65.1%	57.9%	2.1%	7.9%	2.3%

Table 5.3: Regression analysis output using single variables as the independent variables

Independent Variable	$\rho\dfrac{f_u-f_y}{f_c'-f_t'}$	$\dfrac{f_u-f_y}{f_t'*\rho}$	$\rho\dfrac{f_u-f_y}{f_t'}$	$\dfrac{f_u-f_y}{f_c'-f_t'}$	$\dfrac{f_u-f_y}{f_t'}$	$d_b\dfrac{f_u-f_y}{f_t'}$
Multiple R	0.550	0.667	0.692	0.756	0.848	0.891
R-Squared	0.303	0.445	0.479	0.572	0.719	0.794
Significance F	20.0%	10.2%	8.5%	4.9%	1.6%	0.7%

Using $d_b(f_u - f_y)$ / f_t' as the independent variable, the mathematical expression for the regression is described in Equation 5.20:

$$Y = 0.28 + 0.00021 d_b \frac{f_u - f_y}{f_t'} \tag{5.20}$$

Figure 5.3a shows the relationship from Equation 5.20 graphically when compared to the observed data sample, while Figure 5.3b shows the residuals plot corresponding to the regression model. Figure 5.3a shows that the observed $\varepsilon_{rupt,embed}$ / $\varepsilon_{rupt,bar}$ data range appears to be between 0.34 and 0.74. This range is important in determining an upper and lower limit for the reinforcement rupture formulation in the section below. The residuals plot in Figure 5.3b shows the difference between the observed values and the model fitted values, and is a good indicator for any bias in the model. The residuals from this analysis are symmetrically distributed and generally centered on zero, indicating a normal distribution of errors. The residuals also show a random pattern, indicating a good fit for a linear model; any error present is indicative of random error rather than error associated with the chosen independent variable.

(a) Regression line of fit. (b) Plot of residuals.
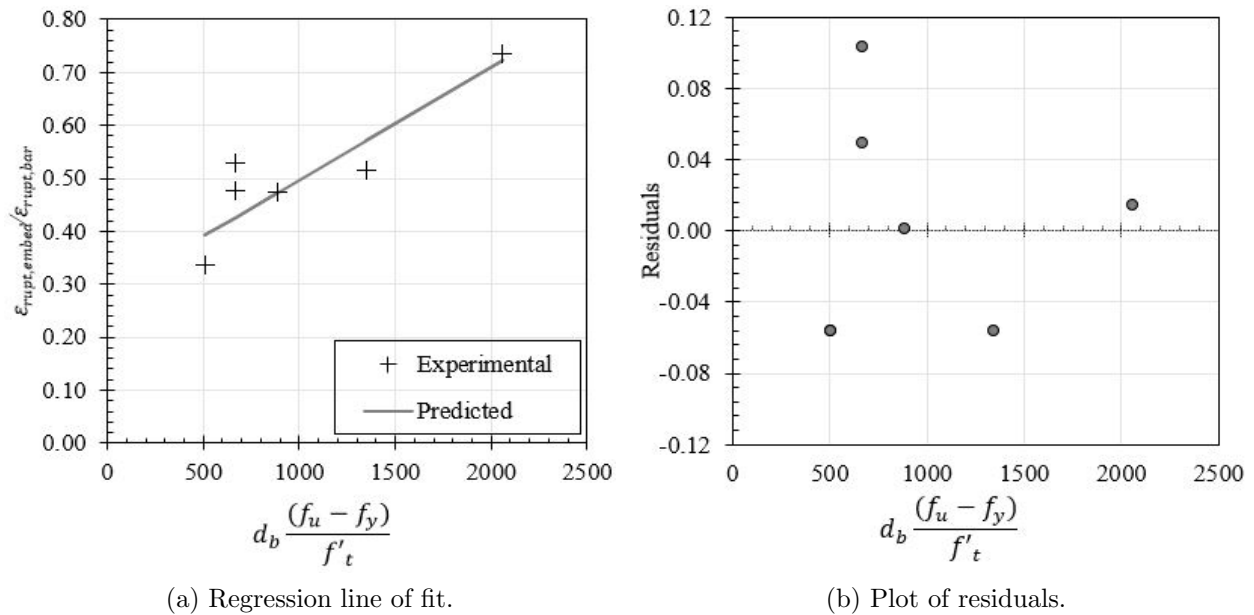
Figure 5.3: Regression analysis results for reinforcement rupture of reinforced concrete members.

5.3.5   Simplified Reinforcement Rupture

Based on the chosen regression expression in Equation 5.20, the following simplified equation for predicting the reinforcement strain at rupture was derived:

$$\frac{\varepsilon_{rupt,embed}}{\varepsilon_{rupt,bar}} = FAC = \frac{7}{25} + 213 * 10^{-6} * d_b \frac{f_u - f_y}{f'_t} \tag{5.21}$$

$$\frac{1}{3} \leq FAC \leq 1.0 \tag{5.22}$$

$$\varepsilon_{rupt,embed} = \varepsilon_{rupt,bar} * FAC \tag{5.23}$$

where, d_b is the diameter of reinforcement in mm, f_u is the ultimate strength of reinforcement in MPa, f_y is the yield strength of reinforcement in MPa, f'_t is the tensile strength of the concrete in MPa, $\varepsilon_{rupt,embed}$ is the calculated rupture strain of the embedded reinforcement in millistrain, $\varepsilon_{rupt,bar}$ is the rupture strain of the bare reinforcement in millistrain, and FAC is the ratio between rupture strain of the embedded reinforcement and the rupture strain of the bare bar, $\varepsilon_{rupt,embed}$ / $\varepsilon_{rupt,bar}$.

The $\varepsilon_{rupt,embed}$ / $\varepsilon_{rupt,bar}$ ratio is assumed to be limited to between 0.33 and 1.0. The value 0.33 was chosen considering the regression line of fit shown in Figure 5.3b. The upper limit of 1.0 was chosen since the embedded rupture strain is assumed to not exceed the bare bar reinforcement rupture strain.

The simplified reinforcement rupture formulation in Equations 5.21, 5.22, and 5.23 was then combined with the Modified Bentz 2005 tension stiffening model as an additional step to predicting reinforcement rupture for both smeared and discrete reinforcements.

5.4   Model Verification

To verify the proposed reinforcement rupture model, a similar verification study to Section 5.2.3 was first performed, and the results are shown in Figure 5.4. Since the reinforcement ratio is no longer a variable in determining reinforcement rupture, only one relationship is available for each concrete compressive strength. The effect of rebar diameter on reinforcement rupture is consistently linear. In addition, as the concrete compressive strength increases, the member increases in stiffness, consequently increasing tension stiffening effects and decreasing reinforcement rupture strain.
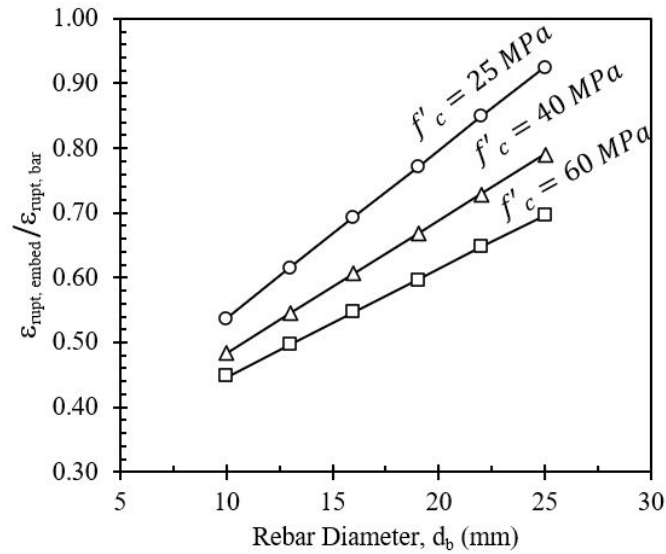
Figure 5.4: Effect of rebar diameter on embedded reinforcement rupture using Modified Bentz 2005 with proposed reinforcement rupture model.

In addition, the seven uniaxial tension members used in the regression analysis were modelled in VecTor2 to validate the proposed reinforcement rupture model. All models were constructed using VecTor2's pre-processor software FormWorks (Wong et al., 2013). The results were processed and analyzed using VecTor2's post-processor Augustus (Bentz, 2010). All constitutive models were VecTor2 default models.

The material properties listed in Table 5.1 were used as input parameters for each specimen. The longitudinal reinforcements were modelled as smeared reinforcements. Pin supports were added to the member's left end nodes, while monotonically increasing displacement-controlled loading points were placed on the right end nodes. A 2D finite element model of a typical uniaxial tension member is shown in Figure 5.5. A mesh sensitivity was performed, and mesh size was determined to have little effect on reinforcement rupture strain. As such, an element size of 50 mm was used to facilitate faster computation speed. The following sections describe the result of the finite element analysis from each experimental program.
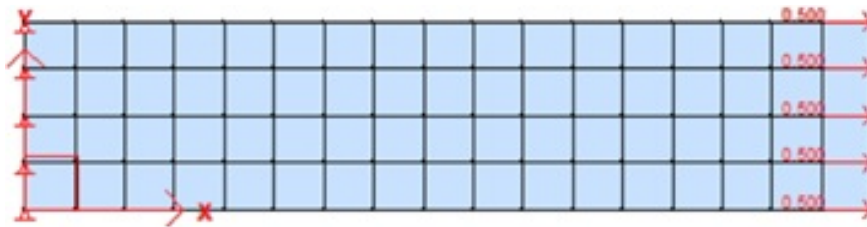
Figure 5.5: 2D finite element model of a typical uniaxial tension member.

Mayer and Eligehausen (1998)

Mayer and Eligehausen (1998) investigated the influence of the bond between concrete and reinforcement on tension stiffening beyond reinforcement yielding. The reinforced concrete members tested varied in cross-sectional size, compressive strength, reinforcement ratio, and reinforcement ductility. The specimen in focus, S4D16-A, was 400 mm by 400 mm in cross section and 2000 mm in length. The member contained four ribbed reinforcing bars, each with a diameter of 16 mm ($\rho = 0.5\%$) and steel ductility class A according to CEB-FIP Model Code 90. Lee et al. (2011) also used this specimen to validate the Lee 2011 (w/ Post-Yield) reinforcement rupture model.

Figure 5.6a shows the experimental and VecTor2 initial response of specimen S4D16-A up to 2.4 millistrain, while Figure 5.6b shows the complete response. Both the VecTor2 initial response and the complete response up until rebar rupture matched experimental results well. In the tensile test of the bare steel bar, the reinforcement ruptured at an average tensile strain of 85 millistrain. Within the concrete tension member, the same reinforcement ruptured at 45 millistrain. The proposed formulation calculates a member embedded reinforcement rupture strain of 36 millistrain, reasonably close to the observed value.
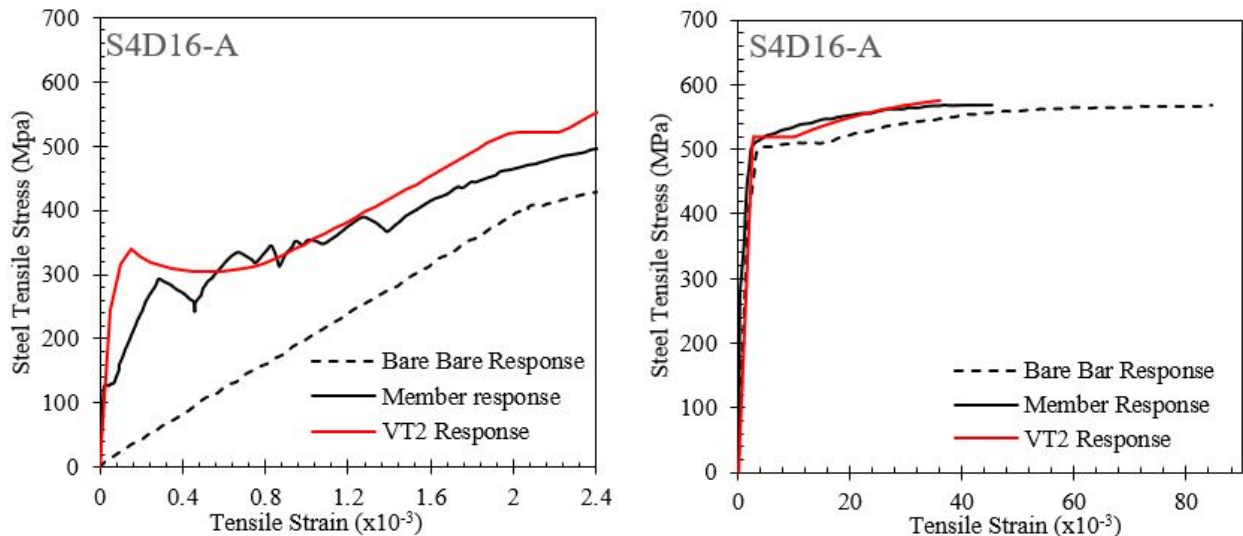
(a) Initial response up to 2.4 millistrain.   (b) Complete response including rebar rupture.

Figure 5.6: Steel stress vs average specimen strain behaviour (Mayer and Eligehausen, 1998).

Moreno et al. (2014)

Moreno et al. (2014) investigated tension stiffening in normal concrete and various high-performance fibre reinforced concrete composite materials. Only the normal reinforced concrete specimen was

used in this verification study. This specimen was 127 mm by 127 mm in cross section and 1041 mm in length. A single US No. 5 ($d_b = 16$ mm) deformed steel bar was placed in the center, resulting in a reinforcement ratio of 1.2%.

Figure 5.7a shows the experimental and VecTor2 response of the normal reinforced concrete specimen in this test program up to 5.0 millistrain, while Figure 5.7b shows the full response up to rupture of the reinforcing bar. The reinforcing bar was assumed to be an A706 US No. 5 bar with a reinforcement rupture strain of 140 millistrain. Within the concrete tension member, the same reinforcement ruptured at 103 millistrain. The proposed formulation calculated a member embedded reinforcement rupture strain of 101 millistrain, close to the observed value.
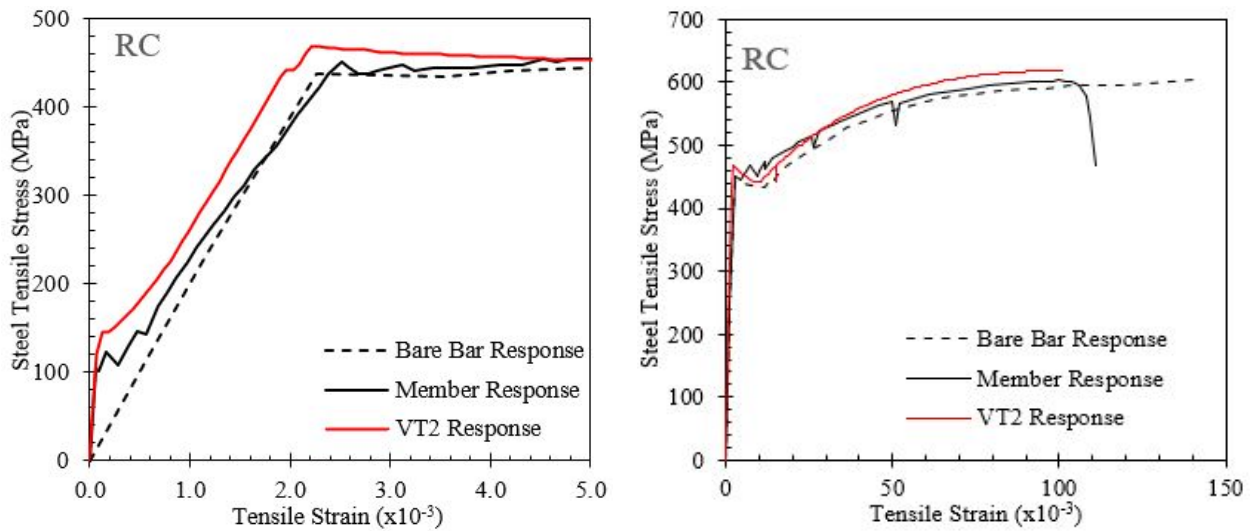
(a) Initial response up to 5.0 millistrain. (b) Complete response including rebar rupture.
Figure 5.7: Steel stress vs average specimen strain behaviour (Moreno et al., 2014).

Kang et al. (2017)

Kang et al. (2017) investigated tension stiffening in normal concrete and reinforced engineered cementitious composites. Only the four normal reinforced concrete specimens were used in this verification study. The specimens had varying cross-sectional sizes and types of reinforcement, both specified in Table 5.4. The bare bar rupture strain for each test specimen is also shown in Table 5.4. All specimens were 1000 mm in length.

Figure 5.8 shows the experimental and VecTor2 full response of the normal reinforced concrete specimens in this test program up to rupture of the reinforcing bar. The proposed reinforcement rupture formulation calculated rupture strains that were reasonably close to the observed values.

Table 5.4: Cross-sectional properties and reinforcement properties for specimens tested by Kang et al. (2017)

Specimen ID	Cross Section mm x mm	d_b mm	A_s mm^2	ρ_s %	$\varepsilon_{rupt,bar}$ x10^{-3}
NC-90-13/1.64	90 x 90	13	111.4	1.64	113
NC-120-13/0.92	120 x 120	13	111.4	0.92	113
NC-150-16/0.89	150 x 150	16	179.5	0.89	126
NC-150-20/1.40	150 x 150	20	292.4	1.40	150
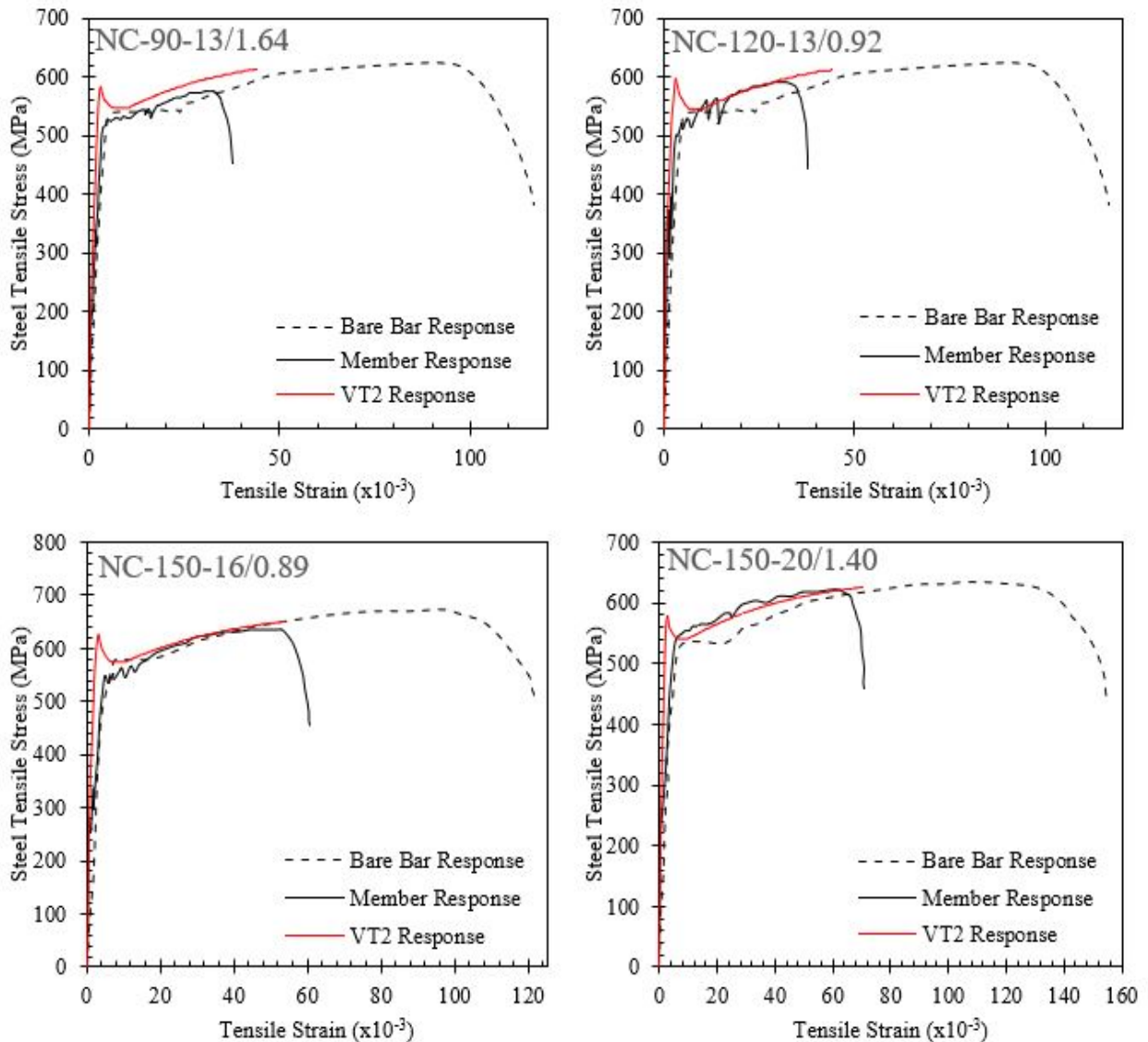
Figure 5.8: Steel stress vs average specimen strain behaviour (Kang et al., 2017).

Nguyen et al. (2019)

Nguyen et al. (2019) investigated reinforcement rupture in normal concrete and hybrid

fibre-reinforced concrete. Only the normal reinforced concrete was used in this verification study. This specimen was 178 mm by 178 mm in cross section and 1040 mm in length. A single US No. 5 (d_b = 16 mm) A706 steel bar was placed in the center, resulting in a reinforcement ratio of 0.6%.

Figure 5.9a shows the experimental and VecTor2 response of the normal reinforced concrete specimen in this test program up to 4.0 millistrain, while Figure 5.9b shows the full response up to rupture of the reinforcing bar. In a tensile test of the bare US No. 5 A706 steel bar, the reinforcement ruptured at an average tensile strain of 140 millistrain. Within the concrete tension member, the same reinforcement ruptured at 72 millistrain. The proposed formulation calculated a member embedded reinforcement rupture strain of 77 millistrain, again reasonably close to the observed value.
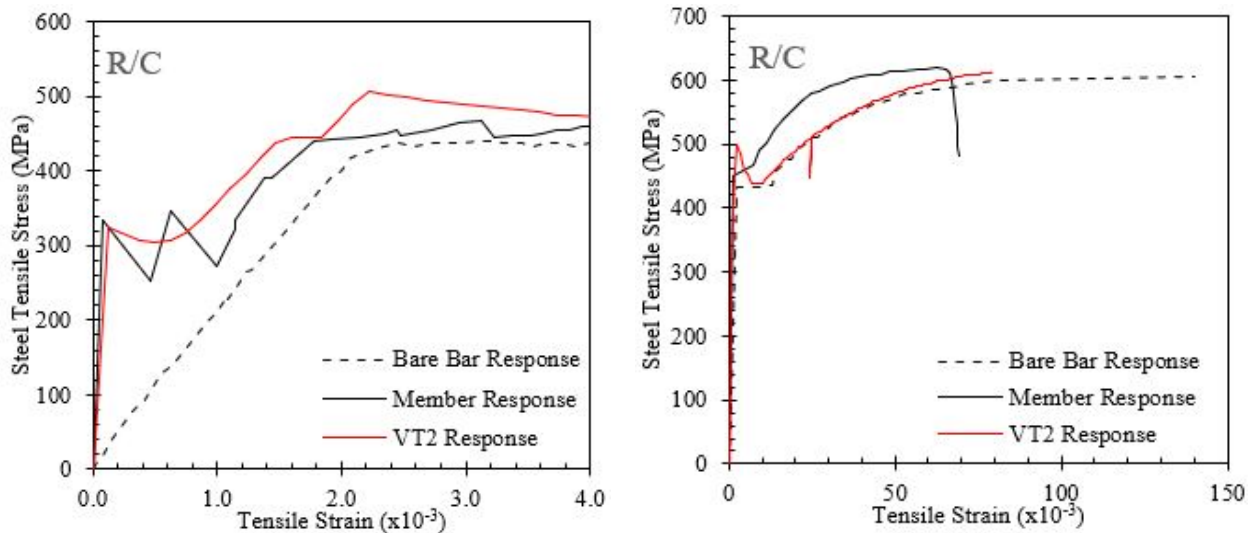
(a) Initial response up to 4.0 millistrain.   (b) Complete response including rebar rupture.

Figure 5.9: Steel stress vs average specimen strain behaviour (Nguyen et al., 2019).

All finite element analysis results using the proposed model matched experimental results reasonably well. Table 5.5 shows a summary comparison between experimental member response and various reinforcement rupture models in VecTor2. Included in this summary is the experimental response, the Lee 2011 (w/ Post Yield) model response, the Lee 2011 model combined with the advanced (Lee 2009) crack stress option mentioned in Section 5.2.2, and the proposed rupture formulation when combined with the Modified Bentz 2005 model.

Figure 5.10 shows a visual comparison between the VecTor2 calculated member rupture strain and the experimental member rupture strain; Figure 5.10a compares the proposed formulation and Lee 2011 model and both models have comparable accuracy. However, Lee's formulation tends to

underestimate the rupture strain. The majority of the calculated-to-test rupture strains for the Lee 2011 model fall below the 0.8 comparison line, with a mean of 0.72, while the proposed formulation has a mean of 1.00. In addition, the Lee 2011 model also has a larger coefficient of variation (CoV) compared to the proposed formulation (17% compared to 13%).

In Figure 5.10b, the bare bar response represents the response obtained from tension stiffening models that do not consider the contribution of concrete stresses after yielding of reinforcement. It is evident that the Lee 2011 model combined with the advanced (Lee 2009) crack stress option significantly overestimates embedded steel rupture strain, with a large dispersion in results (mean of 1.93 with a CoV of 28%). As such, the results from this option were more comparable to the bare bar response, suggesting that perhaps the contribution of concrete stresses was not adequately considered after yielding of the reinforcement. Therefore, further study is required to investigate the advanced (Lee 2009) crack stress option, and the default basic crack stress option is recommended when modelling reinforcement rupture.

(a) comparison of rupture strains for uniaxial tension specimens.

(b) Lee 2011 (w/ Post-Yield) Tension stiffening model with Advanced (Lee 2009) Crack Stress Check.
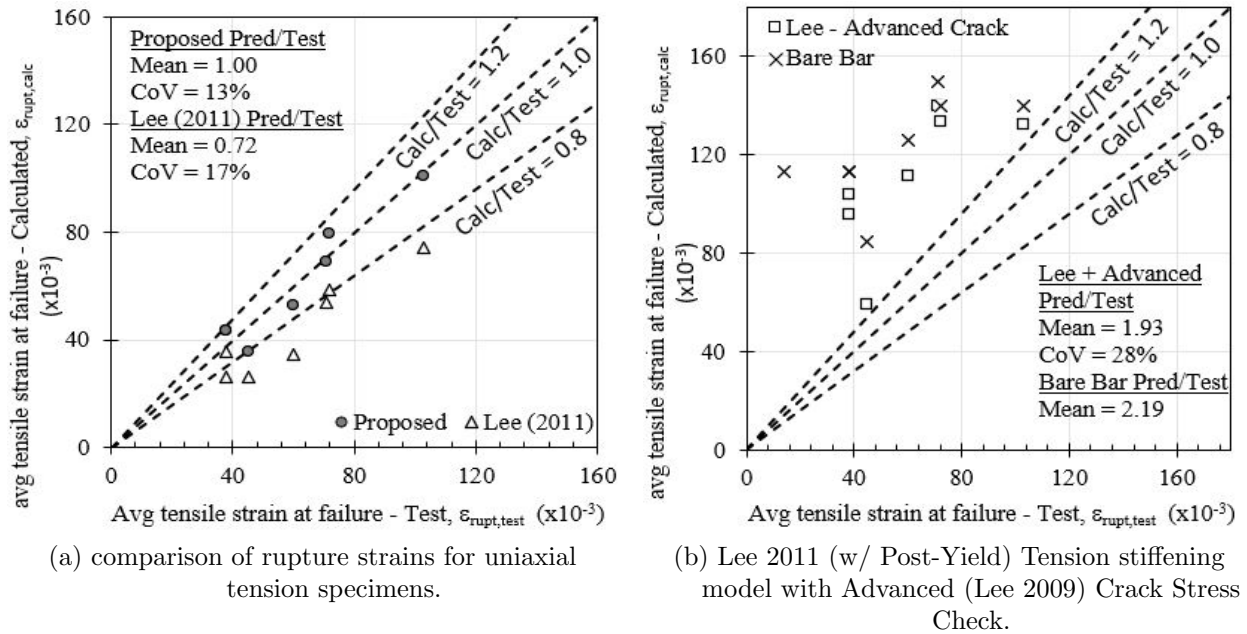
Figure 5.10: Comparison of embedded reinforcement failure strains for uniaxial tensile specimens.

Table 5.5: Comparison of rupture strains for uniaxial test specimens using different models

| Author | Specimen ID | Steel rupture strain (x10^{-3}) | | | | Ratio | | |
		Test (1) $\varepsilon_{rupt,test}$	Lee 2011 (2) $\varepsilon_{rupt,calc}$	Lee + Advanced (3) $\varepsilon_{rupt,calc}$	Proposed (4) $\varepsilon_{rupt,calc}$	(2)/(1)	(3)/(1)	(4)/(1)
Mayer and Eligehausen (1998)	S4D16-A	45	26	59	36	0.59	1.31	0.80
Moreno et al. (2014)	RC	103	74	133	101	0.72	1.29	0.98
Kang et al. (2017)	NC-90-13/1.64	38	36	104	43	0.94	2.73	1.14
	NC-120-13/0.92	38	26	96	43	0.69	2.51	1.14
	NC-150-16/0.89	60	35	112	53	0.58	1.86	0.88
	NC-150-20/1.40	71	54	140	69	0.76	1.97	0.98
Nguyen et al. (2019)	R/C	72	59	134	79	0.82	1.86	1.10
					Mean	0.72	1.93	1.00
					CoV	17%	28%	13%

Chapter 6

Verification Studies

6.1 Introduction

This chapter presents an examination of the efficacy of the revised finite element constitutive models implemented into VecTor2. The finite element (FE) model is first validated using the remaining UHPFRC pure shear panels tested at the University of Toronto. The accuracy of the FE model is further validated with experimental data from SFRC and UHPFRC beam tests found in the literature. The VecTor2 and experimental responses for each tested specimen are then compared and discussed. The finite element modelling of each experimental program is described below. All models were implemented in the nonlinear finite element software VecTor2 and were constructed using VecTor2's pre-processor software FormWorks (Wong et al., 2013). The results were processed and analyzed using VecTor2's post-processor Augustus (Bentz, 2010). The details of each experimental program can be found in Chapter 2. All models conform to the recommendations provided in Chapter 3.

6.1.1 Constitutive Models

VecTor2 contains a comprehensive selection of analysis models for various behaviour mechanisms. Table 6.1 lists the chosen constitutive models to describe these behaviours. The selected models for the analyses were primarily VecTor2 default models, except for the compression pre-peak response and FRC tension response. The chosen constitutive models are briefly described below. Further information on available analysis models in VecTor2 can be found in the FormWorks Manual (Wong et al., 2013).

Concrete Compression Response

For the compression pre-peak response, the Hoshikuma model (Hoshikuma et al. 1997), an exponential function, was selected for the ascending branch of the compression stress-strain curve. This is because this model is known to respond well to concrete with high compressive strengths.

Table 6.1: Constitutive models used for finite element analysis

Concrete Constitutive Models			
Compression Pre-Peak*	Hoshikuma et al.	**Dilation**	Variable - Isotropic
Compression Post-Peak	Hoshikuma et al.	**Cracking Criterion**	Mohr-Coulomb (Stress)
Compression softening	Vecchio 1992	**Crack Stress Calc**	Basic (DSFM/MCFT)
Tension Stiffening	Modified Bentz 2003	**Crack Width Check**	Agg/2.5 Max Crack width
Tension Softening	Nonlinear (Hordijk)	**Crack Slip Calc**	Walraven
FRC Tension*	SDEM - Monotonic OR VEM	**Creep and Relaxation**	Not Considered
Confined Strength	Kupfer/Richart	**Hysteretic Response**	Nonlinear w/ Plastic Offsets
Reinforcement Constitutive Models			
Hysteretic Response	Bauschinger Effect (Seckin)	**Buckling**	Modified Dhakal-Maeka
Dowel Action	Tassios (Crack Slip)	**Concrete Bond**	Eligehausen

*non-default models.

The ascending branch of the compressions stress-strain curve is described as:

$$f_{ci} = E_c \varepsilon_{ci} \left(1 - \frac{1}{n} \left(\frac{\varepsilon_{ci}}{\varepsilon_p} \right)^{n-1} \right) \quad for \quad \varepsilon_p < \varepsilon_{ci} < 0 \tag{6.1}$$

$$n = \frac{E_c}{E_c - E_{sec}} \tag{6.2}$$

$$E_{sec} = -\frac{f_p}{\varepsilon_p} \tag{6.3}$$

where f_{ci} is the principal compressive stress, ε_{ci} is the principal compressive strain, ε_p is the strain at peak stress, E_c is the initial stiffness, f_p is the peak compressive stress, and ε_p is the corresponding strain at peak stress.

The compression post-peak response also used the Hoshikuma model. Beyond the peak compressive stress, f_p, and corresponding strain, ε_p, this model accounts for confinement effects of reinforced concrete and idealizes the descending branch of the compression stress-strain curve as a straight line.

Lastly, compression softening was included to account for the reduction in strength and stiffness due

to transverse cracking and tensile straining. In VecTor2, the compression softening is accounted for by a softening parameter, β_d, with a value between zero and one. The selected model to calculate this parameter was the default Vecchio 1992-A (e1/e2-form) (Vecchio and Collins 1993), a strength and strain softened model based on 116 panel and shell element tests performed at the University of Toronto.

Concrete Tension Response

Prior to cracking, the response was assumed to be linear elastic up to the concrete cracking stress, f'_t.

Tension stiffening effects were included using the Modified Bentz 2005 formulation. This model most accurately represents the average tensile stresses in the concrete as it incorporates the effects of reinforcement properties, bond characteristics, and fibre properties on tension stiffening. In addition, this model is combined with the simplified reinforcement rupture model formulated in Chapter 5.

Tension softening considers the presence of tensile stresses in concrete after cracking. The default Nonlinear (Hordijk) descending post-cracking tensile stress-strain curve was used and considers the softening behaviour of both normal-weight and light-weight concrete. In VecTor2, the average post-cracking concrete tensile stress is assumed to be the larger of the tension stiffening tensile stress and tension softening tensile stress.

Lastly, in this verification study, two types of FRC tension models were considered to account for the contribution of steel fibre reinforcement to the concrete post-cracking tensile stress response: the Simplified Diverse Embedment Model (SDEM) for monotonic loading conditions (Lee et al., 2013a), and the Variable Engagement Model (VEM) (Voo and Foster, 2003). The SDEM considers tensile stress through frictional bond behaviour in straight fibres, and additional tensile stress attained through mechanical anchorage of the hooked-ends in end-hooked fibres. The VEM was developed by integrating the behaviour of a single fibre in three-dimensional space, with the assumption that fibres are uniformly distributed. The VEM calculates the crack opening displacement to determine fibre engagement. For end-hooked fibres, slip between the concrete and fibres must occur before the anchorage is engaged.

Reinforcement Response

The stress-strain model used for ductile steel reinforcement was a three-phase relationship, which includes an initial linear-elastic response, a yield plateau, and a nonlinear strain-hardening phase until rupture.

6.1.2 Material Properties

All material properties not provided by the experimental program were assumed to be the VecTor2 default values shown in Table 6.2.

Table 6.2: Default VecTor2 material properties

Concrete Properties		Steel Properties	
Tensile Strength (MPa)	$f_t' = 0.33\sqrt{f_c'}$	Elastic Modulus (MPa)	$E_s = 200000$
Initial Tangent Modulus (MPa)	$E_c = 3320\sqrt{f_c'} + 6900$	Strain Hardening Strain (x10⁻³)	$\varepsilon_{sh} = 10$
Cylinder Strain at f_c' (x10⁻³)	$\varepsilon_o = 1.8 + 0.0075 f_c'$	Ultimate Strain (x10⁻³)	$\varepsilon_u = 150$
Poisson's Ratio	$\mu = 0.15$	Poisson's Ratio	$\mu = 0.30$
Mass Density (kg/m³)	$\gamma = 2400$	Mass Density (kg/m³)	$\gamma = 7850$

The effect of concrete tensile strength, f_t', on UHPFRC behaviour was previously investigated in Chapter 3. The recommended default tensile strength used in VecTor2 of $f_t' = 0.33\sqrt{f_c'}$ MPa was considered conservative and a lower bound estimate of tensile strength. As a result, it is expected that there will be a lower-bound predicted response for all models in this verification study.

Chapter 3 also showed that the predicted load-deflection curve is sensitive to the input maximum crack spacing in the x- and y- directions, s_x and s_y (mm), respectively. For a UHPFRC material with strain-hardening performance after cracking, a consistent value for maximum crack spacing was assumed to be:

$$s_x = s_y = 2l_f \tag{6.4}$$

where l_f is the maximum length of the fibres used, in mm.

In the case of RC specimens with no fibres, and for FRC with a strain-softening response after cracking, the maximum crack spacing is taken as the minimum between the overall specimen depth

and the CSA A23.3-14 formulation for equivalent crack spacing parameter:

$$s_x = s_y = min(h, \frac{35d_v}{15 + a})$$

(6.5)

where h is the depth of the beam in mm, a is the maximum aggregate size in mm, d_v is the effective shear depth in mm, taken as the greater of $0.9d$ or $0.72h$.

6.1.3 Analysis Parameters

All analysis parameters were VecTor2 default settings, which included a maximum number of iterations per load stage of 60, an averaging factor of 0.6, a convergence limit of 1.00001, a displacement-based weight average convergence criteria, and a static nonlinear load step. The VecTor2 default analysis models were also used. No analysis parameter calibrations were performed.

6.2 Modelling of Shear Panels

The modelling first focused on the series of large-scale UHPFRC panels with varying conventional reinforcement tested by Yap (2020). All panels were tested under in-plane pure shear monotonic loading conditions at the University of Toronto.

The panels were modelled as a single four-node plane stress rectangular element with a dimension of 1000 x 1000 mm. In Chapter 3, the element thickness was shown to affect the behavioural response. As a result, each panel was modelled with a thickness matching the as-built experimental thickness. The lower-left corner of the element was restrained in both the x- and y-directions, while the lower-right corner was restrained in the y-direction only. The FE models were load-controlled with loads applied at the four nodes to create pure shear loading conditions. For each panel, nodal forces were modified to result in a monotonically increasing shear stress of 0.05 MPa at each analysis step until failure. Figure 6.1 shows an example of the support and loading condition using panel YS1, which had a thickness of 215 mm.

All material properties available from the testing program were used in the models. Both the conventional and fibre reinforcement were modelled as smeared reinforcement embedded in the concrete. The input material parameters for concrete and smeared reinforcement are given in Table 6.3 and Table 6.4, respectively. As per the recommendations of Chapter 3, the maximum crack spacing in both the x- and y-directions were taken as the experimental value of 50 mm. The

steel fibre properties are given in Table 6.5.
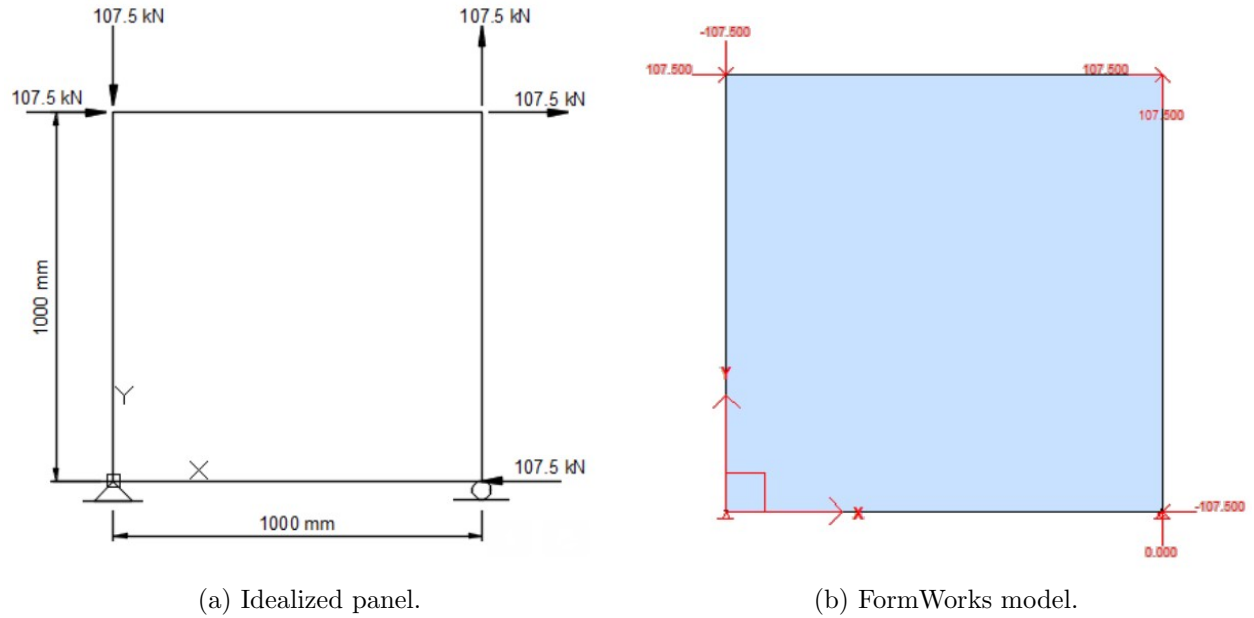
(a) Idealized panel.   (b) FormWorks model.
Figure 6.1: Finite element modelling of panel YS1.

Table 6.3: Panel properties used for finite element modelling of UHPFRC panels tested by Yap (2020)

Panel	Concrete							Reinforcement			
								x reinf.		y reinf.	
	t	f'_c	E_c	ε_o	a	s_x	s_y	Type	ρ_x %	Type	ρ_y %
	mm	MPa	MPa	x10^{-3}	mm	mm	mm				
YS1	215	171.0	49600	3.91	1	50	50	10M	0.861	10M	0.861
YS2	206	167.5	46400	4.16	1	50	50	10M	0.899	-	0
YS3	212	164.2	48000	4.04	1	50	50	-	0	-	0
YS4	217	157.0	47100	3.67	1	50	50	20M	2.560	-	0
YS5	224	160.3	46600	3.86	1	50	50	D8	0.427	-	0

t = beam width; f'_c = concrete compressive strength; E_c = Young's modulus; a = maximum aggregate size; s_x and s_y = crack spacing in x- and y-direction, respectively; ρ_x and ρ_y = longitudinal reinforcement in x- and y-direction, respectively.

Table 6.4: Reinforcement properties used for finite element modelling of UHPFRC panels tested by Yap (2020)

Bar	d_b mm	E_s MPa	f_y MPa	f_u MPa	ε_{sh} x10^{-3}	ε_u x10^{-3}
D8	8.1	191300	588	603	-	35.8
10M	11.3	185600	481	633	18.6	144.5
20M	19.5	174200	467	564	21.7	123.8

d_b = bar diameter; E_s = elastic modulus; f_y = yield strength; f_u = ultimate strength; ε_{sh} = strain hardening strain; ε_u = ultimate strain.

Table 6.5: Steel fibre properties for finite element modelling of UHPFRC panels tested by Yap (2020)

Fibre Type	V_f %	l_f mm	d_f mm	f_{uf} MPa
Straight	1.0	20	0.2	2700
End-hooked	1.0	25	0.25	2700

V_f = fibre volume fraction; l_f = fibre length; d_f = fibre diameter; f_{uf} = fibre ultimate tensile strength.

Figure 6.2 compares the shear stress-strain relationships between the experimental response and the VecTor2 response using the SDEM and VEM FRC tension models. Both SDEM and VEM captured the initial pre-cracking shear stiffness well. The predicted cracking stress for both SDEM and VEM was approximately 4.2 MPa for the five panels, all lower than the reported experimental cracking stress. This was expected as a result of using the default cracking strength available in VecTor2, which is commonly used for conventional reinforced concrete rather than UHPFRC.

Both the SDEM and VEM captured well the post-cracking stiffness for all panels, except for YS3 and YS5. In Panel YS3, the experimental results showed a strain-softening response after cracking. Yap (2020) speculated that since this specimen did not contain any conventional reinforcement, there may have been a weak plane with fewer fibres, resulting in a strain-softening behaviour. Both the SDEM and VEM, however, showed strain-hardening responses. This is expected since VecTor2 automatically categorizes any concrete material with a compressive strength of greater than 120 MPa as a strain-hardening material. Although Panel YS5 showed a strain-hardening response similar to the other panels, both the SDEM and VEM significantly underestimated its post-cracking stiffness.

In general, the SDEM post-cracking, pre-peak response was better aligned with the experimental results. However, the VEM captured the ultimate shear strength capacity better than the SDEM. Both the SDEM and VEM appear to overestimate the deformation capacity of the panels. Furthermore, rupture of the conventional reinforcement was observed experimentally in panels YS1 and YS5, though the finite element model results did not capture this rupture. Since the reinforcement rupture formulated in Chapter 5 was based on reinforced concrete members, it is not yet suitable for UHPFRC, and further research is required.
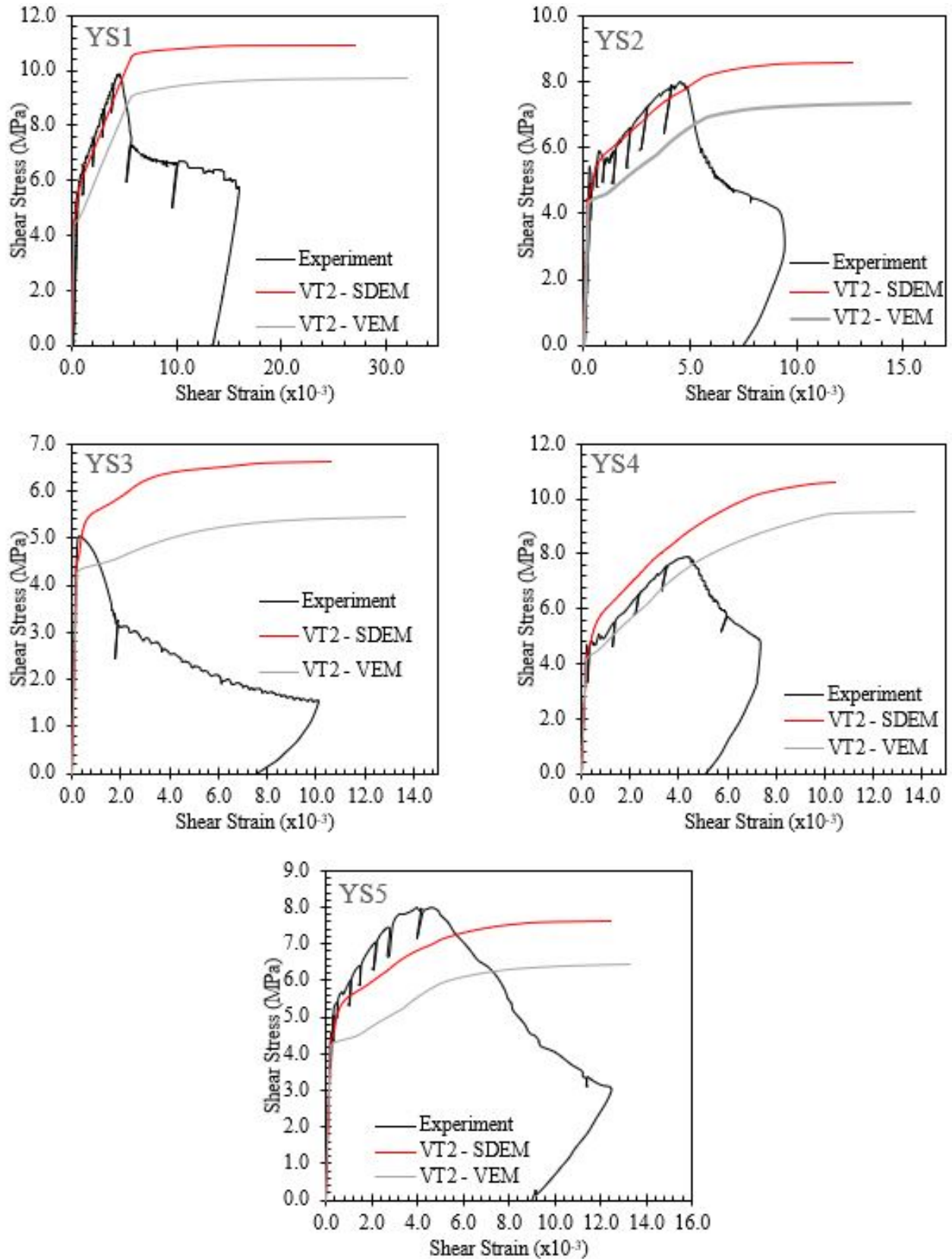
Figure 6.2: Experimental and VecTor2 shear stress-strain response of UHPFRC panels tested by Yap (2020).

6.2.1   Inverse Analysis

In addition to the large-scale panel element tests, Yap (2020) also performed flexural bending tests on prisms and uniaxial direct tension tests on dogbone specimens. Tensile properties for panels YS1 to YS4 were obtained from inverse analysis of the prism tests, while tensile properties for panel YS5 were obtained from the direct tension tests. The SDEM and VEM calculated tensile responses were first compared with the results from the inverse analysis and direct tension tests. VecTor2 models that used a custom tension softening curve with input data taken from the inverse analysis and direct tension tests were then compared with the large-scale experimental results.

First, tensile responses from the inverse analysis of the prism tests and direct tension tests were compared with the SDEM and VEM calculated tension responses. Five uniaxial tension members were modelled in VecTor2 using the concrete and fibre material properties of each YS panel. The tension members were modelled as a single four-node plane stress rectangular element 1000 mm in length, 150 mm in width, and with a thickness of 100 mm. The lower-left corner of the element was restrained in both the x- and y-directions, while the upper-left corner was restrained in the x-direction only. Displacement controlled loads were applied to the right nodes, and monotonically increased by 0.1 mm at each analysis step until failure. The fibre reinforcement was modelled as smeared reinforcement embedded in the concrete, and no conventional reinforcement was included in the model. Figure 6.3 shows an example of the uniaxial tension specimen model in VecTor2.

Figure 6.3: 2D VecTor2 model of uniaxial tension specimen.

Figure 6.4 shows the tensile responses from the inverse analysis of prism tests when compared to the SDEM and VEM calculated tensile responses. The inverse analysis results are shown as dotted lines, while the SDEM and VEM calculated results are shown in solid lines. Although all five panels had similar material properties, there were large variations in tensile responses from the inverse analysis. For example, YS3 and YS4 produced the highest cracking stresses and peak tensile stress. YS5, which was tested using direct tension tests, produced the lowest tensile response. These variations may be a possible result of experimental factors affecting UHPFRC behaviour, such as fibre distribution and orientation, not captured by the VecTor2 calculated responses.

At large crack widths, the SDEM captured the reduction in tensile stresses well and provided a very similar post-peak response to the inverse analysis results. When compared to the VEM-calculated response, the SDEM results more closely matched the post-cracking peak stress for three of the five panels. Additionally, the SDEM accurately predicted the crack width at which the concrete tensile stress is zero. As the concrete tensile stresses approach zero, the SDEM-calculated maximum crack width for all five panels was approximately 6.3 mm. This value is roughly one-fourth of the maximum fibre length in the panels and may suggest a correlation between fibre length and maximum crack width. In contrast, the VEM underestimated the reduction in tensile stresses at large crack widths and significantly overestimated the maximum crack width to over 9.0 mm.
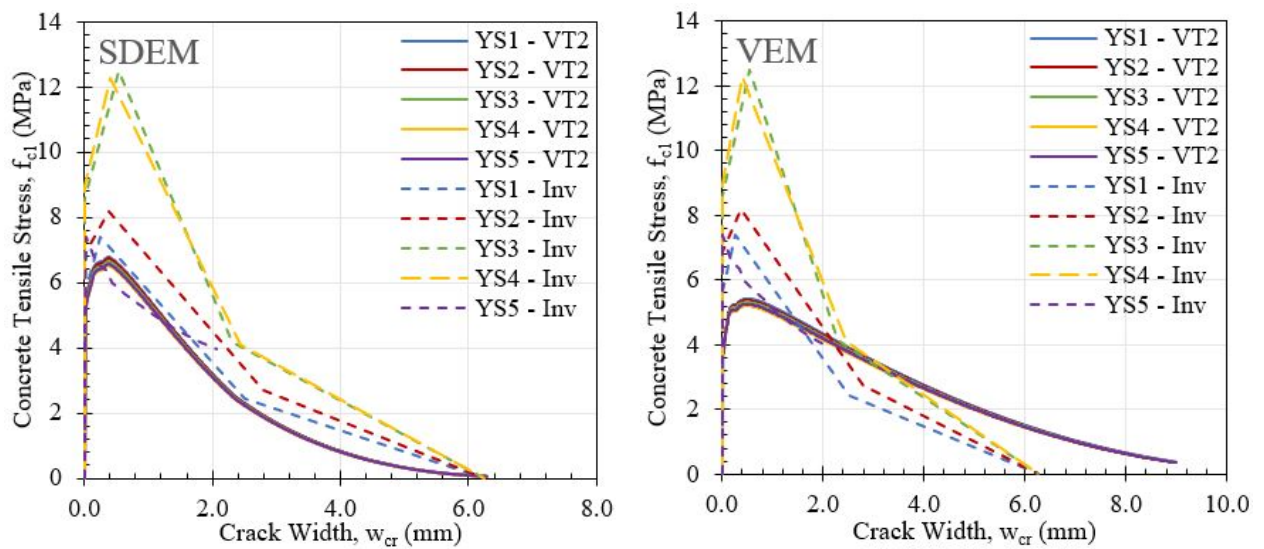
(a) SDEM tensile stress-crack width responses.   (b) VEM tensile stress-crack width responses.

Figure 6.4: Tensile responses from inverse analysis of prism tests compared with tensile response calculated by SDEM and VEM for all YS panels.

Next, VecTor2 models were constructed with a custom tension softening curve using the inverse analysis and direct tension results. The Custom Input (Crack Based) option was selected as the tension softening constitutive model. The peak stress-crack value, along with two other points taken from the post-peak stress-crack width tensile response in Figure 6.4, were manually entered into the tension softening curve in VecTor2. Table 6.6 shows the pre-peak inverse analysis results from prism tests for YS1 to YS4 and the direct tension test results for YS5. The default VecTor2 cracking strength of $f_t' = 0.33\sqrt{f_c'}$ MPa used in each model was also replaced by cracking stress from Table 6.6. Table 6.7 shows the input crack-stress values that were entered into VecTor2 as the custom tension softening model for each panel. The crack width at peak stress used as the first

point in the tension softening model was calculated using Equation 6.6:

$$w_{cr} = \varepsilon_{fu} s_{cr} \qquad\qquad (6.6)$$

where ε_{fu} is the strain at peak stress from Table 6.6, and s_{cr} is the crack spacing estimated using Equation 6.5.

Table 6.6: Inverse analysis and uniaxial direct tension test properties for finite element analysis

Specimen	f'_c MPa	f'_t MPa	f_{fu} MPa	ε_{fu} x10⁻³
YS1	171.1	5.66	7.39	5.16
YS2	167.5	6.89	8.18	7.46
YS3	164.2	8.57	12.48	10.80
YS4	157.0	8.96	12.28	8.27
YS5*	160.3	4.67	7.41	0.42

*results from direct tension test.

Table 6.7: Custom (crack based) tension softening input values for inverse analysis

Specimen	Point 1 w_{cr} mm	Point 1 f_{c1} MPa	Point 2 w_{cr} mm	Point 2 f_{c1} MPa	Point 3 w_{cr} mm	Point 3 f_{c1} MPa	Point 4 w_{cr} mm	Point 4 f_{c1} MPa
YS1	0.23	7.39	2.5	2.5	6.25	0	0	0
YS2	0.37	8.18	2.82	2.71	6.26	0	0	0
YS3	0.54	12.48	2.33	4.1	6.25	0	0	0
YS4	0.41	12.28	2.48	4.07	6.26	0	0	0
YS5*	0.02	7.41	0.92	5.23	2.05	3.92	6.25	0

*results from direct tension test.

The results obtained from the custom tension softening curve were compared with experimental, SDEM, and VEM results in Figure 6.5. Similar to the SDEM and VEM results, the models using the inverse analysis and direct tension tests captured the pre-cracking shear stiffness well. In addition, models of all panels, except for YS3 and YS5, also captured the post-cracking stiffness well. However, the models that used inverse analysis results grossly overestimated the cracking stress of the panels; the inverse analysis cracking stress ranged from 5.66 MPa to 8.96 MPa, all significantly higher than the reported panel experimental cracking stress.
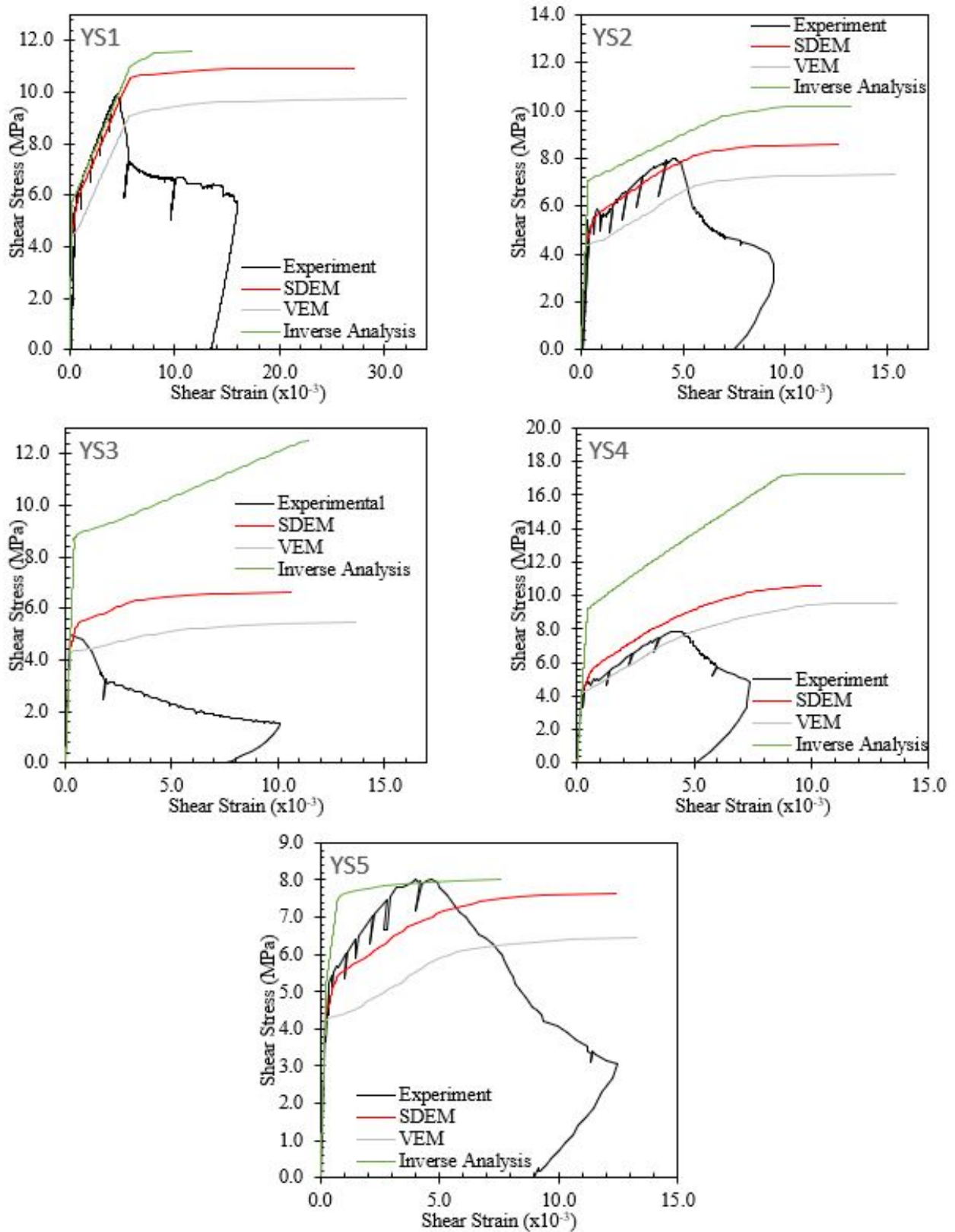
Figure 6.5: Experimental and VecTor2 responses using inverse analysis results from prism tests and direct tension tests of UHPFRC panels tested by Yap (2020).

Similarly, the models which used the inverse analysis results also significantly overestimated the ultimate stress capacity, especially for YS3 and YS4. In panel YS3, which had no conventional reinforcement, the VecTor2 model using the inverse analysis results were unable to capture the strain-softening behaviour, much like SDEM and VEM. The model for panel YS5, which used the direct tension test properties in the tension softening curve, also captured the pre-cracking stiffness well. However, using inverse analysis methods for this model appears to overestimate the post-cracking shear stiffness. This model also produced the most accurate estimate of cracking stress and ultimate capacity. Lastly, all models using the custom tension softening curve were unable to capture the panels' deformation capacity. Panels YS1 and YS5 underestimated the deformation capacity, while panels YS2 and YS4 overestimated the deformation capacity; panel YS3, however, produced a reasonably similar deformation capacity to the experimental results.

A comparison summary of the experimental and VecTor2 peak shear stress, $\nu_{xy,u}$, is provided in Table 6.8. The average VecTor2 calculated-to-experimental ultimate capacity ratios for SDEM and VEM were 1.17 and 1.00, respectively. Both SDEM and VEM had a coefficient of variation (CoV) of 16%. This suggests that the SDEM overestimated the shear capacity compared to the VEM, and that the VEM may be a better predictor of the response. In contrast, the average calculated-to-experimental ultimate capacity using the custom tension softening curve extracted from the inverse analyses of test prism data was 1.62, a gross overestimation of capacity. In addition, the CoV of 41% suggests a weak correlation of results. The significant overestimation of cracking stress and ultimate stress capacity is a result of the input parameters found through inverse analysis of the prism tests. Since the direct tension test results provided satisfactory results, the large deviations from experimental results when modelling with inverse analysis may be due to flaws with the flexural prism testing and post-analysis procedure.

Overall, the models using inverse analysis results as input parameters in the tension softening curve provided much poorer response calculations when compared to SDEM and VEM. The use of flexural prism test results in finite element models produced a gross overestimation of UHPFRC behaviour and is therefore not recommended for use in modelling in its current form. On the other hand, direct tension test results may aid in increasing the accuracy of finite element models. Further investigations are recommended for the applicability of using uniaxial direct tension test properties in the custom tension softening model in VecTor2.

Table 6.8: Experimental and VecTor2 peak shear stress. Yap (2020)

Panel	$\nu_{xy,u,exp}$ Experiment (1) MPa	$\nu_{xy,u,SDEM}$ SDEM (2) MPa	$\nu_{xy,u,VEM}$ VEM (3) MPa	$\nu_{xy,u,inv}$ Inverse (4) MPa	$\dfrac{\nu_{xy,u,SDEM}}{\nu_{xy,u,exp}}$ (2)/(1)	$\dfrac{\nu_{xy,u,VEM}}{\nu_{xy,u,exp}}$ (3)/(1)	$\dfrac{\nu_{xy,u,inv}}{\nu_{xy,u,exp}}$ (4)/(1)
YS1	9.90	10.91	9.73	11.59	1.10	0.98	1.17
YS2	8.03	8.58	7.35	10.17	1.07	0.92	1.27
YS3	4.99	6.62	5.44	12.5	1.33	1.09	2.51
YS4	7.91	10.60	9.55	17.24	1.34	1.21	2.18
YS5	8.04	7.98	6.47	8.03	0.99	0.80	1.00*
				Mean	1.17	1.00	1.62
				CoV	16%	16%	41%

*tensile properties from direct tension tests.

6.3   Modelling of Beams

In order to validate SDEM and VEM capabilities in modelling fibre reinforced beams, the modelling first focused on a comprehensive experimental test series by Dinh (2010), which consisted of 28 steel fibre reinforced concrete (SFRC) beams in shear. Subsequently, SDEM and VEM capabilities were examined using 22 UHPFRC flexural specimens tested by Yang et al. (2010), Yoo and Yoon (2015), Yoo et al. (2016a), Singh et al. (2017), and Kodur et al. (2018).

All beams were modelled in VecTor2 with specific dimensions according to each test specimen. In general, the finite element mesh consisted of four-node plane stress rectangular elements and three-node constant strain triangular elements, both with uniform thickness. Mesh size sensitivity analyses were not performed as 15-20 elements through the depth of a beam is historically seen to have good results in VecTor2. Thus, depending on the height of the beam, the maximum mesh size used was between 10 mm and 25 mm, with a maximum aspect ratio of 1.5. Two-node truss elements were used to model the longitudinal reinforcement. As bond failure was not experimentally observed in any test specimens, perfect bond was assumed between the longitudinal rebar and the concrete. Fibres and shear reinforcement were modelled as smeared reinforcement within the concrete. At supports and load application points, one layer of bearing material with one layer of steel plate material was defined to adequately disperse concentrated forces to the beams. The total number of each element type for the modelled beams is summarized in Table 6.9.

Table 6.9: VecTor2 2D finite element modelling specimen and mesh summary

Author	Specimen ID	Maximum mesh size	Elements through depth	Rectangular Elements	Triangular Elements	Truss Elements
Dinh et al. (2010)	B18-0a,b B18-1a,b B18-3a,b,c,d B18-5a,b	25	19	2095	0	210
	B18-7a,b B18-2a,b,c,d B27-1a,b B27-2a,b	25	19	2001	6	206
	B27-3a,b B27-4a,b B27-5 B27-6 B27-7	35	19	2464	6	384
Yang et al. (2010)	NR-1,2 R13-1,2 R14-2	15	18	1788	0	98
Yoo and Yoon (2015)	NF-0.94 NF-1.50 S13-0.94 S13-1.50 S19.5-0.94 S19.5-1.50 S30-0.94 S30-1.50	15	22	2830	0	250
Yoo et al. (2016)	UH-N UH-0.53% UH-1.06% UH-1.71%	15	18	1792	6	98
Singh et al. (2017)	B15-1 B15-2 B25-1	10	15 15 25	2024 1984 4679	0 0 3	272 272 354
Kodur et al. (2018)	U-B3 and U-B5 U-B4 and U-B6	15	22	2458 4866	6 9	135 268

Loading conditions for the modelled beams include symmetrical three-point bending, symmetrical four-point bending, and asymmetrical loading for shear investigations. The load in the FE models was applied as a vertical displacement and increased monotonically until failure. Figure 6.6 shows examples of the various loading scenarios and the associated 2D VecTor2 models. The various colours signify different material regions used. Any beams loaded under symmetric four-point bending only required modelling of half of the system to save computational time and power.
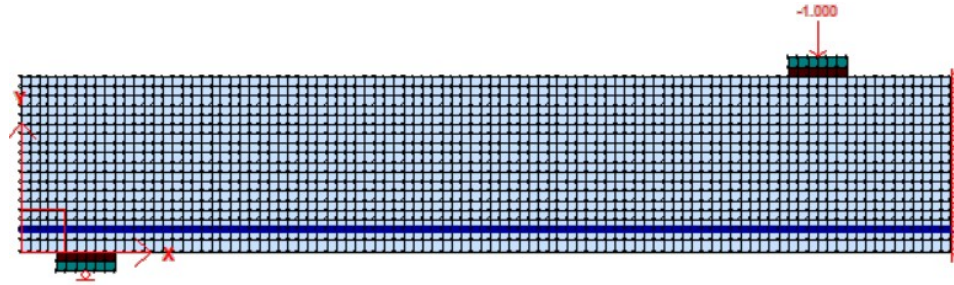
(a) Modelling of a beam under symmetrical four-point bending. Yang et al. (2010) Beam R13.
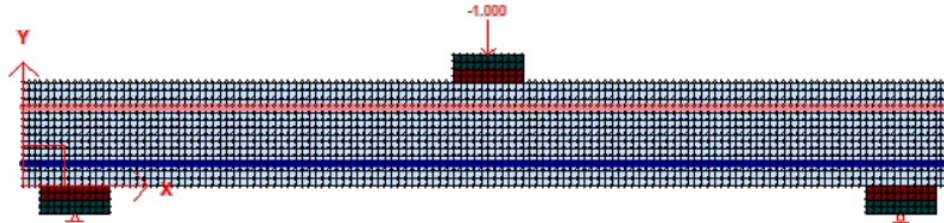
(b) Modelling of a beam under symmetrical three-point bending. Singh et al. (2017) Beam B15-1.
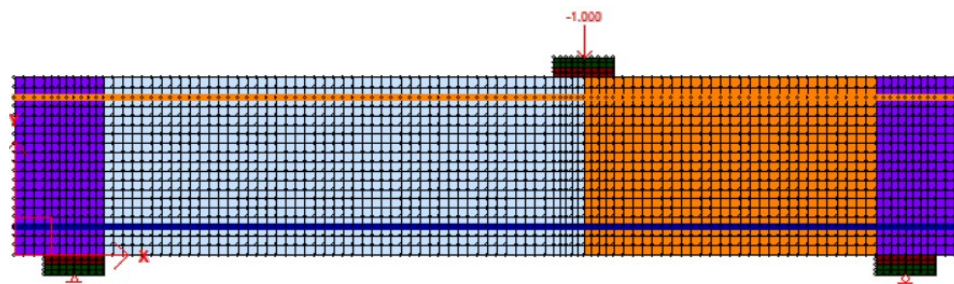
(c) Modelling of a beam under asymmetrical shear loading. Dinh (2010) Beam B18-1.
Figure 6.6: 2D finite element model for the simulation of beams under various loading configurations.

6.3.1 SFRC Beams

Dinh (2010) tested 28 large-scale simply-supported SFRC beams under a monotonic concentrated load to investigate the effect of end-hooked fibres on SFRC shear behaviour. The experimental program consisted of eight pairs of B18-Series beams, and four pairs plus four single beams for the B27-Series. Beams from each pair were considered identical to reduce uncertainty in the data, and experimental results from both are presented. The beams in Beam Series B18 were 152 mm wide and 455 mm in depth, while those in Beam Series B27 were 203 mm wide and 685 mm in depth. All beams had a shear-span-to-effective-depth ratio of approximately 3.5 and were all designed to fail in the longer shear span. The shorter shear span and supports in all beams were reinforced with transverse reinforcement. The studied parameters included beam depth, fibre length, fibre aspect ratio, fibre strength, and fibre volume fraction.

All material properties available from the testing program were used in the models. Different material regions were defined to simulate the varying shear reinforcement along the span. In the shorter shear span, Beam Series B18 contained US #4 stirrups spaced at 127 mm while Beam Series B27 contained US #4 stirrups spaced at 102 mm. All transverse reinforcement was modelled as smeared vertical reinforcement within the concrete. Three types of end-hooked fibre reinforcement and three types of longitudinal reinforcement were investigated. Two control specimens, beams B18-0 and B27-7, did not contain any fibre reinforcement. The input concrete material property, along with reinforcement used, is shown in Table 6.10. The crack spacing values were taken as twice the maximum fibre length as per Equation 6.4 and as per Equation 6.5 for the control specimens without fibres. All other material properties were reported by Dinh (2010). The fibre reinforcement and longitudinal reinforcement properties are shown in Table 6.11 and Table 6.12, respectively.

Table 6.10: Material properties used for finite element modelling of SFRC beams tested by Dinh (2010)

Specimen	Concrete				Reinforcement							
	f_c'	a	s_x	s_y	Fibre		Bottom Bars			Top Bars		
					Type	V_f	Type	No. of	A_s	Type	No. of	A_s
	MPa	mm	mm	mm		%		bars	mm^2		bars	mm^2
B18 − 0a,b	42.8	10	455	455	-	-	#7	4	1548	#4	2	258
B18 − 1a,b	44.8	10	60	60	1	0.75	#6	4	1136	#4	2	258
B18 − 2a,b	38.1	10	60	60	1	1.00	#6	4	1136	#4	2	258
B18 − 2c,d	38.1	10	60	60	1	1.00	#7	4	1548	#4	2	258
B18 − 3a,b	31.0	10	60	60	1	1.50	#7	4	1548	#4	2	258
B18 − 3c,d	44.9	10	60	60	1	1.50	#7	4	1548	#4	2	258
B18 − 5a,b	49.2	10	120	120	2	1.00	#7	4	1548	#4	2	258
B18 − 7a,b	43.3	10	60	60	3	0.75	#6	4	1136	#4	2	258
B27 − 1a,b	50.8	10	60	60	1	0.75	#8	5	2545	#4	2	258
B27 − 2a,b	28.7	10	120	120	2	0.75	#8	5	2545	#4	2	258
B27 − 3a,b	42.3	10	60	60	1	0.75	#7	5	1935	#4	2	258
B27 − 4a,b	29.0	10	120	120	2	0.75	#7	5	1935	#4	2	258
B27 − 5	44.4	10	60	60	1	1.50	#8	5	2545	#4	2	258
B27 − 6	42.8	10	120	120	2	1.50	#8	5	2545	#4	2	258
B27 − 7	37.0	10	685	685	-	-	#7	5	1935	#4	2	258

Table 6.11: Fibre properties. Dinh (2010)

| Fibre Number | Fibre Type | l_f | d_f | f_{uf} |
		mm	mm	MPa
1	End-Hooked	30	0.55	1100
2	End-Hooked	60	0.75	1050
3	End-Hooked	30	0.28	2300

Table 6.12: Longitudinal reinforcement properties. Dinh (2010)

Bar	d_b mm	A_b mm^2	E_s MPa	ε_{sh} x10^{-3}	f_y MPa	f_u MPa
#3	9.5	71	199948	-	414	579
#4	12.7	129	193053	8	461	689
#6	19.1	284	193053	9	496	751
#7	22.2	387	193053	8	448	675
#8	25.4	509	193053	8	455	686

The experimental and VecTor2 simulated load-deflection response for SFRC Beam Series B18 and B27 are shown in Figure 6.7 and Figure 6.8, respectively. In general, both SDEM and VEM models were unable to capture the response of the specimens with a high degree of accuracy, with significant scatter in the results apparent. In particular, both models were unable to capture the deformation capacity of the beams consistently.
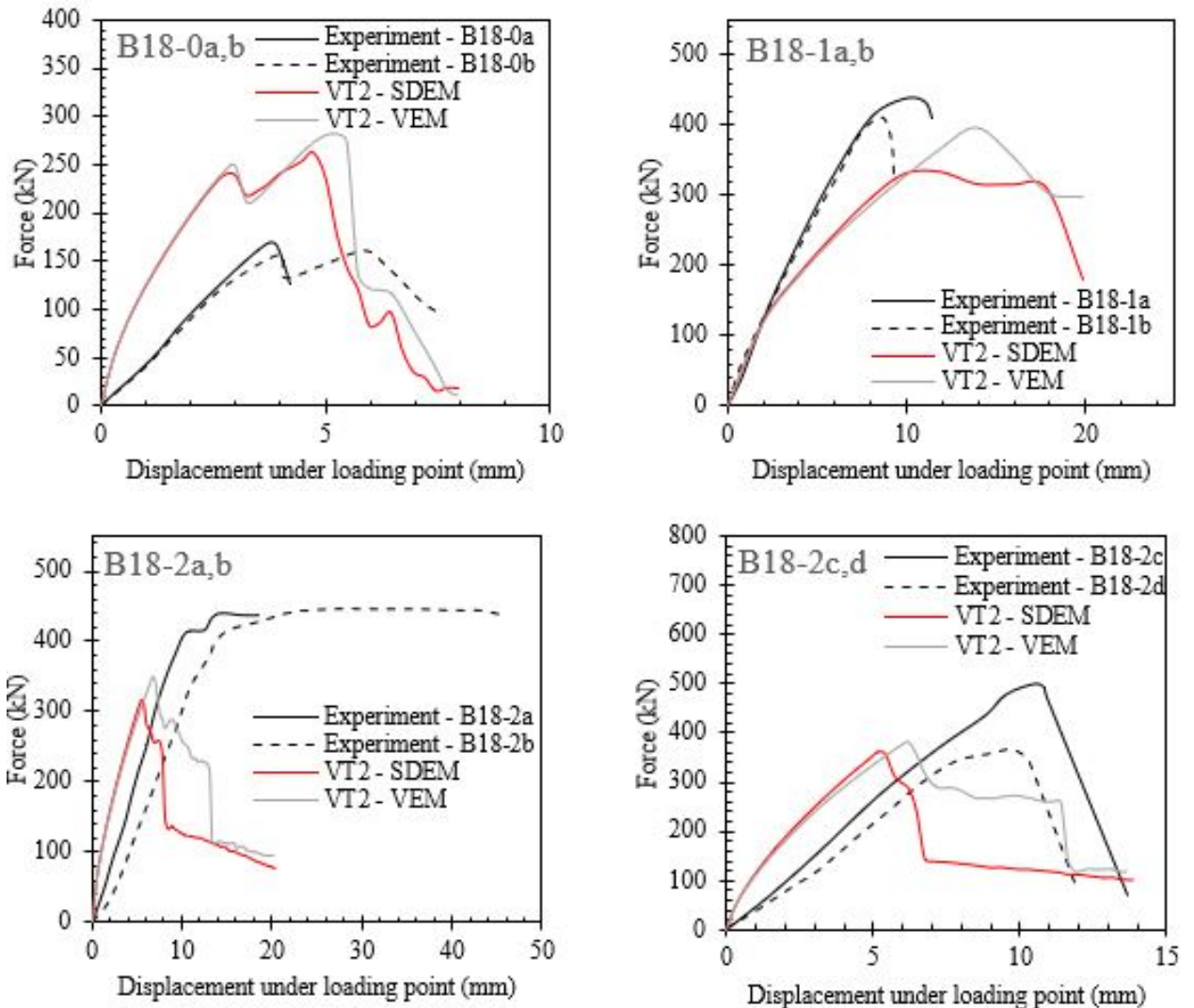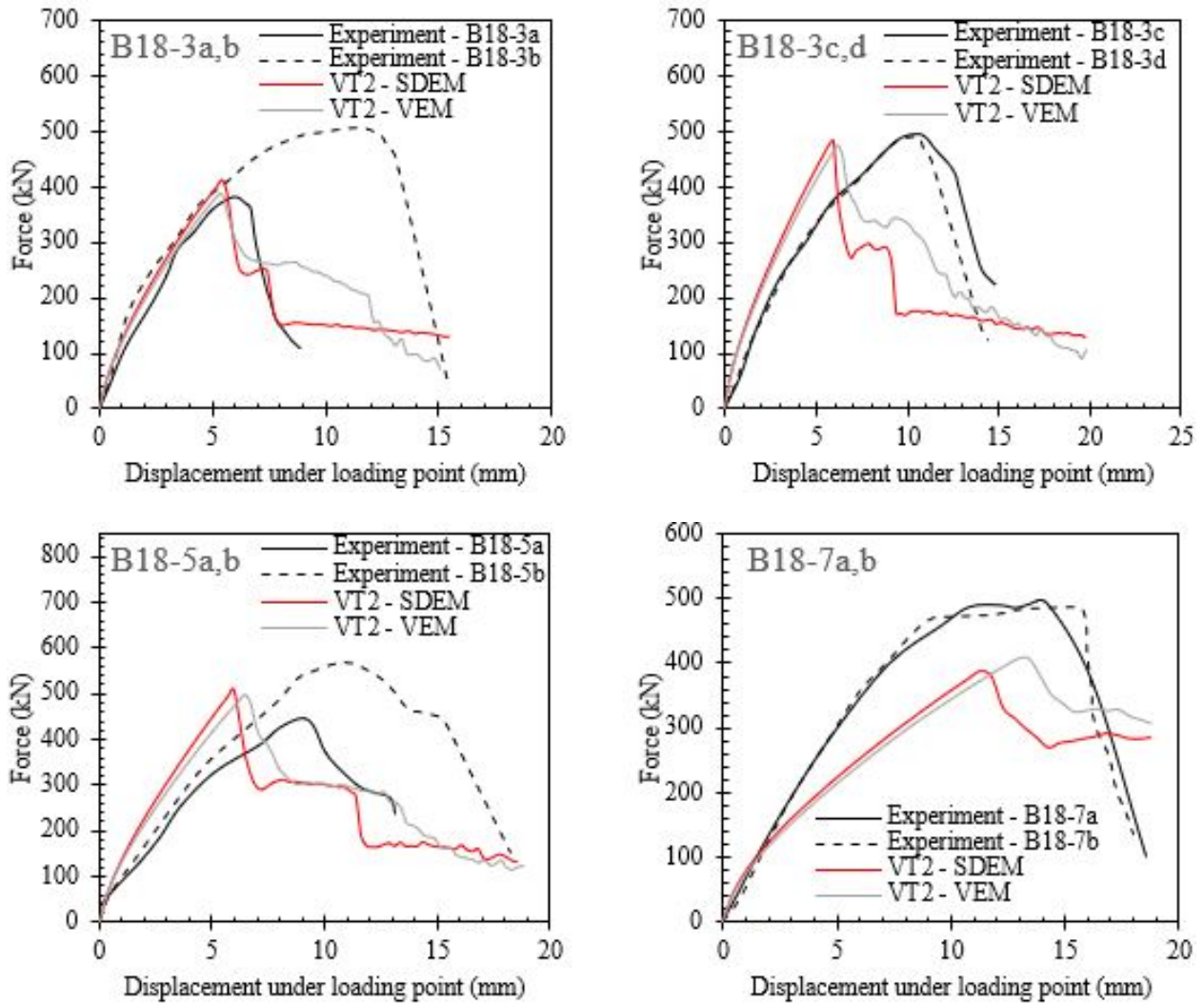
Figure 6.7: Experimental and VecTor2 force-displacement curves of Beam Series B18 tested by Dinh (2010).

First, it is interesting to note that there were significant differences in the observed experimental response within each pair of identical beams tested. For example, Beam 18-2b exhibited a much larger yield plateau than Beam 18-2a. Likewise, Beams 18-3b and B18-5b exhibited much lower ultimate strengths than their identical counterparts 18-2a and 18-5a. It is evident that a wide range of factors, such as fibre orientation and concrete consolidation, can affect the experimental results. It may be challenging to accurately assess the capabilities of VecTor2 in analyzing these members as it currently cannot account for these unpredictable variations.
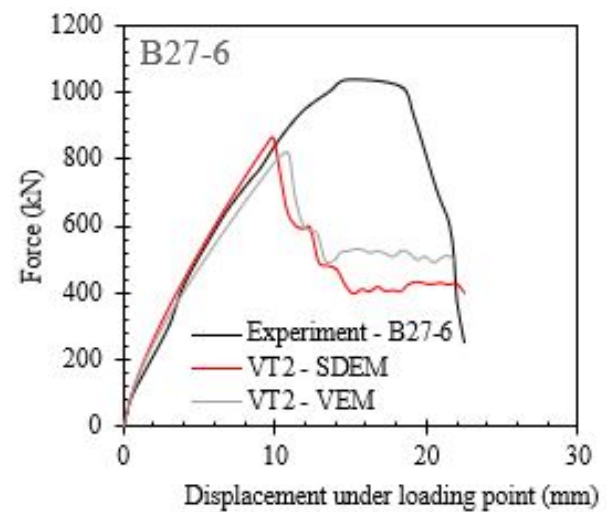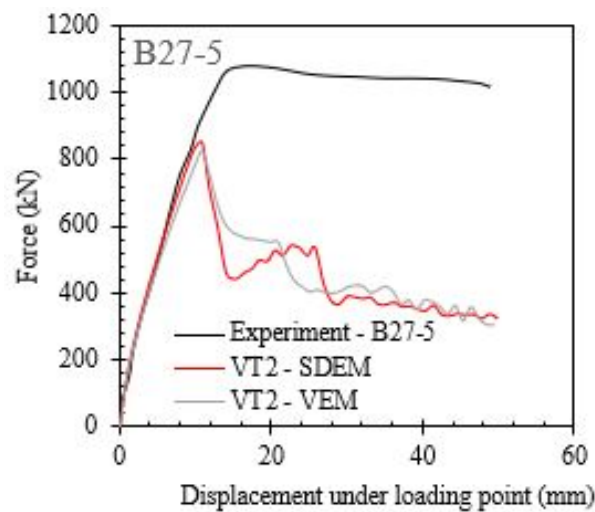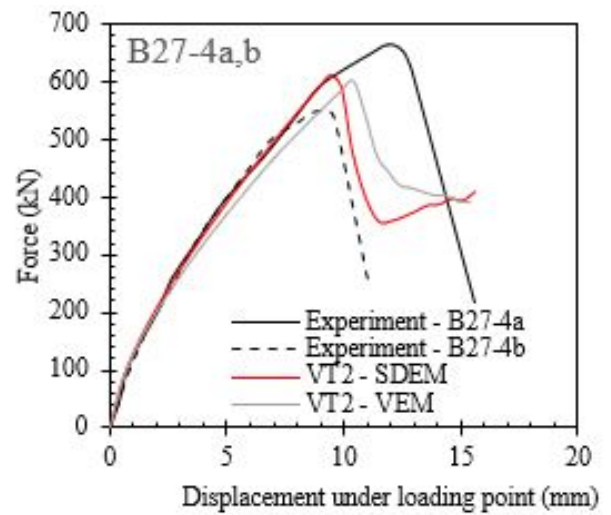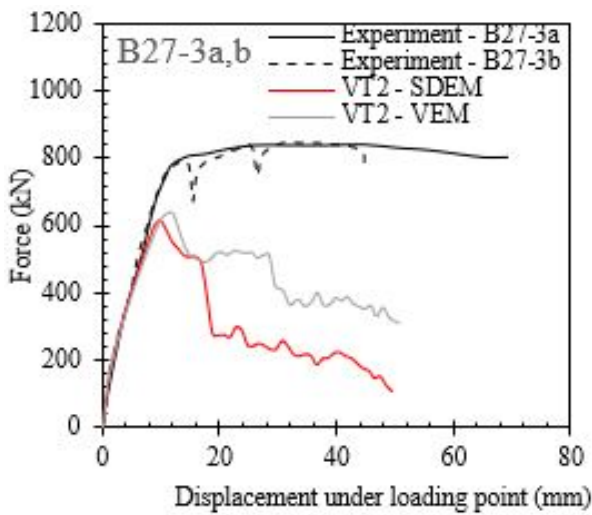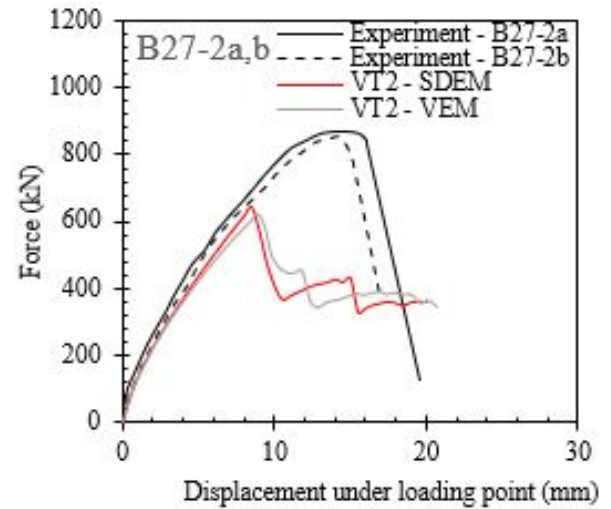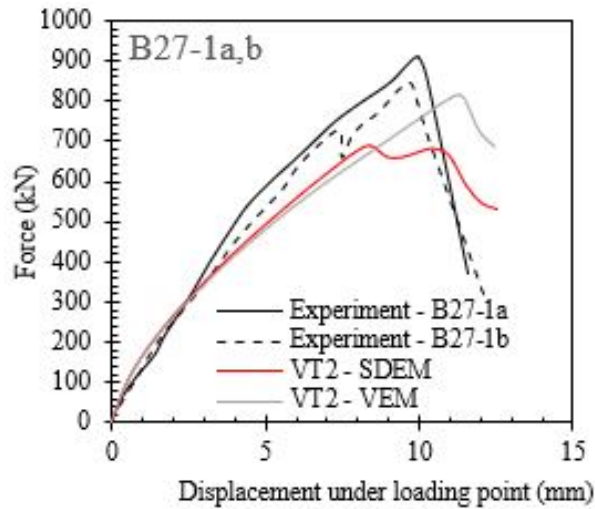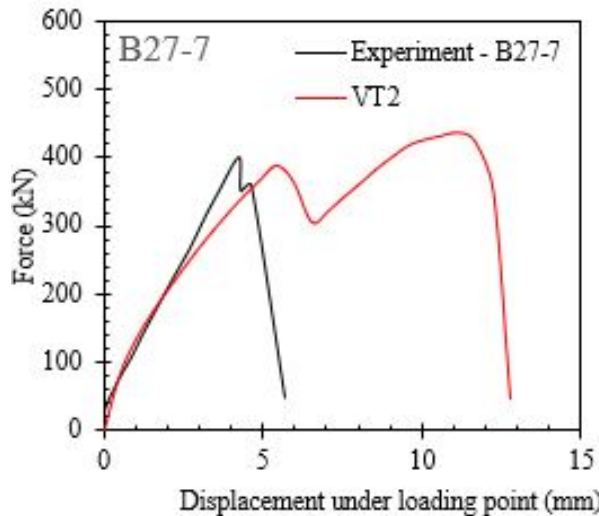
Figure 6.8: Experimental and VecTor2 force-displacement curves of Beam Series B27 tested by Dinh (2010).

In Beams B18-1 and B18-7, where the fibre contents were both 0.75%, the finite element models captured the pre-cracking stiffness well but underestimated the post-cracking stiffness. By comparison, the finite element models overestimated both the pre- and post-cracking stiffnesses of beams with 1% and 1.5% fibre content. In the B27-Series, both finite element models captured the pre-peak stiffness well, except in the case of B27-7 with no fibres. In addition, the stiffness was best captured in Beams 18-3a,b, which had the lowest compressive strength ($f'_c = 31.0$ MPa), large reinforcement ratio (ρ_s=2.7%), and large fibre content ($V_f = 1.5$%). By contrast, the stiffness was overestimated for Beams 18-3c,d, which were identical to Beams B18-3a,b, except for a higher compressive strength ($f'_c = 44.9$ MPa). This may suggest that VecTor2 default stiffness formulation may be more accurate for fibre reinforced concrete with low compressive strengths.

In the experimental investigation, all test beams except for B27-3a failed in shear. Both SDEM and VEM were able to capture this observed shear failure, whereby failure was instigated by the opening of a critical diagonal crack in the longer shear span that propagated along the flexural reinforcement towards the support. Both Beams B27-3a and B27-3b, which contained 0.75% of Type 2 fibre and 1.56% longitudinal reinforcement, exhibited ductile behaviour after yielding of the reinforcement. Beam B27-3a showed a flexural failure with crushing of the compression zone near the loading point after yielding of the reinforcement. Beam 27-3b, in contrast, experienced a shear-compression failure with a shorter yield plateau. Although the ultimate failure modes of these two identical beams were different, both beams exhibited ductile failure with the ultimate strength governed by the flexural strength. This ductile behaviour, however, was not captured

by the VecTor2 models; neither SDEM nor VEM exhibited a long yield plateau after yielding of the longitudinal reinforcement. Similarly, Beams B18-2 and B27-5 also exhibited ductile behaviour that was not captured by VecTor2.

The shear stresses for the experimental result and the VecTor2 simulated results are calculated for each specimen using Equation 6.7:

$$\tau = \frac{V}{bd} \tag{6.7}$$

where V is the shear force in kN, b is the beam width in mm, and d is the depth of the beam measured from the extreme compression fibre to the longitudinal reinforcement, in mm.

Figure 6.9 shows a plot of shear stress for the average experimental data versus the simulated data using SDEM and VEM. The summary statistics are shown in Table 6.13. The average VecTor2 predicted-to-experiment ratios for SDEM and VEM were 0.91 and 0.93, with a corresponding coefficient of variation of 25% and 26%, respectively. Overall, both models provided comparable accuracy with slightly better results using the VEM. In addition, the majority of the results fall under the equal ratio and thus are conservative predictions of the shear strength.

In comparing the two different sized beams, the mean VecTor2 predicted-to-test ratio for Beam Series B18 is higher than Beam Series B27 (0.95 compared to 0.85 for SDEM and 0.99 compared to 0.86 for VEM). However, Beam Series B27 has a significantly smaller coefficient of variation (16% compared to 29% for SDEM and 17% compared to 30% for VEM) and smaller spread. This suggests that although the B18 beams had a better predicted-to-test ratio, the B27 beam results were better correlated. As such, there may exist a size effect in SFRC beams not previously considered by the current FRC modelling formulations.
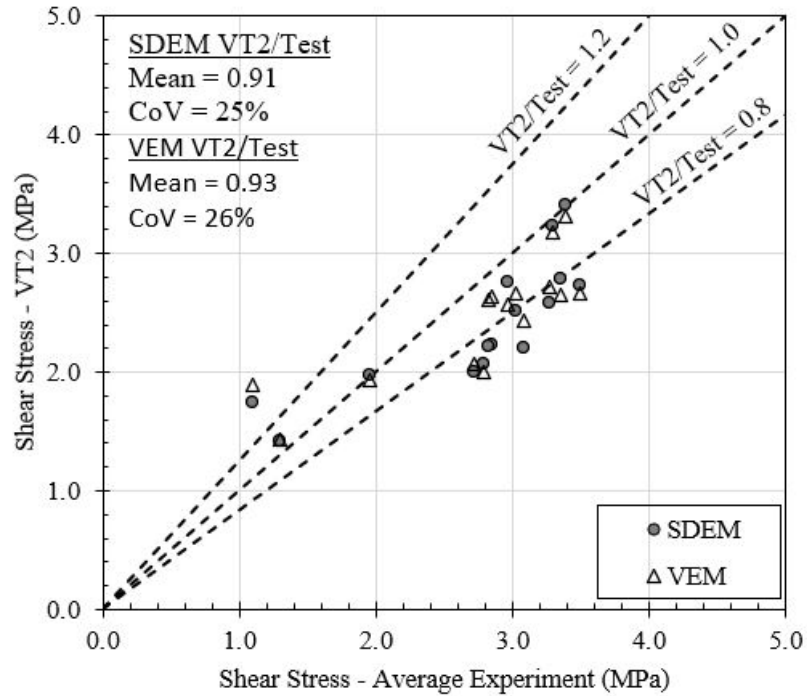
Figure 6.9: Comparison of VecTor2 calculated shear stress and experimental shear stress for SFRC members tested by Dinh (2010).

Table 6.13: Summary statistics of VecTor2 finite element modelling of beams tested by Dinh (2010)

	SDEM	VEM
Beam Series B18		
Mean	0.95	0.99
CoV	29%	30%
Min	0.72	0.79
Max	1.59	1.71
Spread	0.87	0.92
Beam Series B27		
Mean	0.85	0.86
CoV	16%	17%
Min	0.73	0.72
Max	1.09	1.10
Spread	0.36	0.38

6.3.2 UHPFRC Beams

Yang et al. (2010)

Yang et al. (2010) tested two sets of seven simply-supported UHPFRC beams under symmetrical

four-point bending to investigate the effect of low longitudinal reinforcement ratio on flexural behaviour of UHPFRC beams. All beams were of rectangular cross section, 180 mm in width, 270 mm in depth, and contained varying amounts of longitudinal reinforcement. All material properties available from the testing program were used in the finite element models. The beams in this experimental program did not contain transverse reinforcement. The input material properties for the concrete and type of longitudinal reinforcement used for each specimen are shown in Table 6.14 and Table 6.15, respectively. The crack spacing values were taken as twice the maximum fibre length as per Equation 6.4. All other material properties were reported by Yang et al. (2010). The fibre properties are shown in Table 6.16. The yield and ultimate strengths of the longitudinal reinforcement were not reported and, as such, were assumed to be VecTor2 default values of 400 MPa and 600 MPa, respectively.

Table 6.14: Material properties used for finite element modelling of flexural beams tested by Yang et al. (2010)

Specimen	Concrete					Reinforcement		
	f'_c	E_c	a	s_x	s_y	Bottom Bars		
						Type	No. of	A_s
	MPa	MPa	mm	mm	mm		bars	mm^2
NR − 1	196.7	46818	0.5	26	26	-	-	-
R13 − 1,2	192.2	46480	0.5	26	26	D13	3	380.1
R14 − 2	196.1	45530	0.5	26	26	D13	4	506.8

Table 6.15: Longitudinal reinforcement properties. Yang et al. (2010)

| Bar | d_b | E_s | f_y | f_u |
	mm	MPa	MPa	MPa
D13	13	200000	400*	600*

*data unavailable; values assumed.

Table 6.16: Steel fibre properties. Yang et al. (2010)

Fibre Type	V_f %	l_f mm	d_f mm	f_{uf} MPa
Straight	2	13	0.2	2500

Experimental load-displacement results were only available for three beams, and as such, only those three beams were modelled in VecTor2. Figure 6.10 compares the experimental and VecTor2 simulated load-displacement curves for the three specimens considered. SDEM and VEM gave comparable results and both underestimated the ultimate load-carrying capacity of the beams.

This underestimation was most significant in Beam NR, which did not contain any longitudinal reinforcement. The average reported experimental cracking loads for Beams NR, R13, and R14-2 were 62.6 kN, 69.5 kN and 67.8 kN, respectively. The VecTor2 models appear to underestimate these cracking loads for all three beams, as one might expect with the use of a lower-bound estimate for the cracking stress of the concrete. In addition, the change of slope in the experimental load-deflection plots indicates the onset of tensile cracking and the progression of these cracks. In general, the finite element models captured the pre-cracking stiffness well but underestimated the post-cracking stiffness. Lastly, both SDEM and VEM were unable to capture the deformation capacity of the beams.
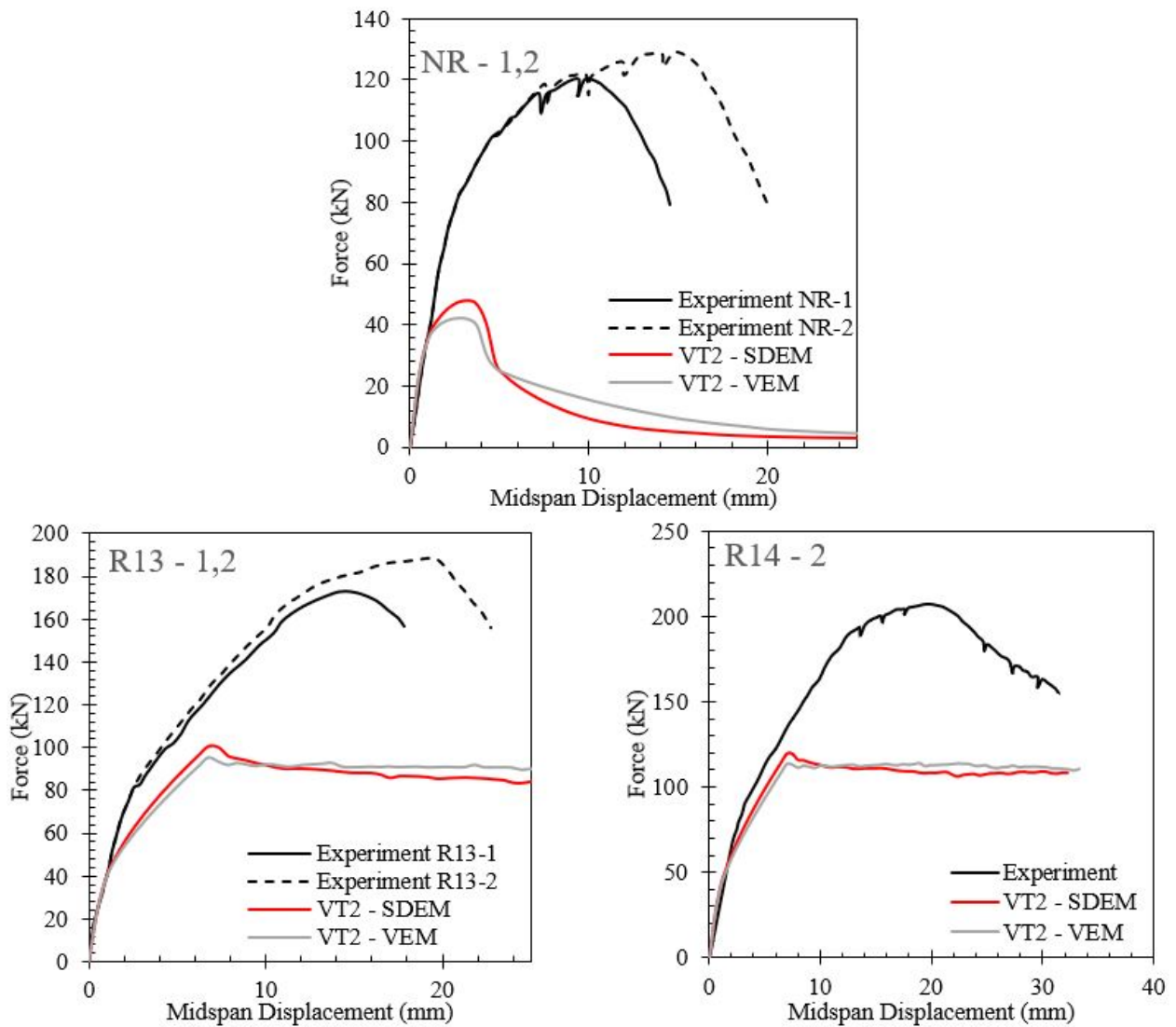
Figure 6.10: Experimental and VecTor2 force-displacement curves of beams tested by Yang et al. (2010).

Yoo and Yoon (2015)

Yoo and Yoon (2015) tested ten large-scale simply-supported UHPFRC beams under symmetrical four-point bending to investigate the effects of type and length of steel fibre on flexural behaviour. All beams were of rectangular cross section, 150 mm in width and 220 mm in depth. Two different longitudinal reinforcement ratios ($\rho = 0.94\%$ and 1.50%), and two different steel fibre types (smooth and twisted) were considered. VecTor2 currently does not have the capabilities to model twisted steel fibres and as a result, Beam T30, which used twisted steel fibres, was not included in this investigation.

All material properties available from the testing program were used in the models. All the beams tested contained D10 closed stirrups at a spacing of 80 mm, which were modelled as smeared vertical reinforcement in the concrete. The input material properties for the concrete, along with the type of longitudinal reinforcement used for each specimen, are shown in Table 6.17. The crack spacing values were taken as twice the maximum fibre length as per Equation 6.4 and as per Equation 6.5 for the specimens without fibres. All other material properties were reported by Yoo and Yoon (2015). The smeared reinforcement and longitudinal reinforcement properties are shown in Table 6.18 and Table 6.19, respectively. The ultimate strength of the longitudinal reinforcement used was not reported, and as such, the VecTor2 default value of 600 MPa was used in the analysis.

Table 6.17: Material properties used for finite element modelling of flexural beams tested by Yoo and Yoon (2015)

Specimen	Concrete						Longitudinal Reinforcement					
	f'_c	E_c	ε_o	a	s_x	s_y	Bottom Bars			Top bars		
							Type	No. of bars	A_s	Type	No. of bars	A_s
	MPa	MPa	x10^{-3}	mm	mm	mm			mm^2			mm^2
NF 0.94	200.9	45365	-	1	220	220	D13	2	253.4	D10	2	142.6
NF 1.50							D16	2	397.2	D10	2	142.6
S13 0.94	211.8	46733	4.53	1	26	26	D13	2	253.4	D10	2	142.6
S13 1.50							D16	2	397.2	D10	2	142.6
S19.5 0.94	209.7	46881	4.84	1	39	39	D13	2	253.4	D10	2	142.6
S19.5 1.50							D16	2	397.2	D10	2	142.6
S30 0.94	209.7	46773	4.58	1	60	60	D13	2	253.4	D10	2	142.6
S30 1.50							D16	2	397.2	D10	2	142.6

Figure 6.11 and Figure 6.12 compare the load-displacement relationship between the experiments to the finite element models using VecTor2. Beams NF – 0.94 and NF – 1.50 contained no fibres, and thus VEM and SDEM gave the same result. In Beam NF-0.94%, which contained a reinforcement

Table 6.18: Smeared reinforcement properties. Yoo and Yoon (2015)

| Specimen | | Fibre | | | | | Stirrup | |
		Type	V_f %	l_f %	d_f mm	f_{uf} MPa	Type	ρ %
NF	0.94	-	-	-	-	-	D10	1.188
	1.50						D10	1.188
S13	0.94	Straight	2	13	0.2	2788	D10	1.188
	1.50						D10	1.188
S19.5	0.94	Straight	2	19.5	0.2	2500	D10	1.188
	1.50						D10	1.188
S30	0.94	Straight	2	30	0.2	2580	D10	1.188
	1.50						D10	1.188

Table 6.19: Reinforcement properties. Yoo and Yoon (2015)

Bar	d_b mm	E_s MPa	f_y MPa	f_u MPa	ε_u x10^{-3}
D16	15.9	200000	510	600*	190
D13	12.7	200000	495	600*	190
D10	9.5	200000	491	600*	200

*data unavailable; values assumed.

ratio of 0.94%, the VecTor2 model overestimated the ultimate capacity of the beams. In contrast, VecTor2 captured well the response of Beam NF-1.50%, which had a reinforcement ratio of 1.50%. Similar to Yang et al. (2010), the SDEM and VEM models gave comparable results for beams with fibres and both underestimated the ultimate load-carrying capacity. In addition, the VecTor2 models appear to better capture the ultimate capacity of beams with a fibre length of 30 mm (S30-0.94% and S30-1.50%) compared to beams with a fibre length of 13 mm (S13-0.94% and S13-1.50%). Unlike the results of Yang et al. (2010), however, the cracking load appears to be captured well by both SDEM and VEM. In general, the VecTor2 models for this experimental response captured the pre-cracking stiffness well but overestimated the post-cracking stiffness. Lastly, both SDEM and VEM captured a ductile response after yielding of the reinforcement. However, both models generally underestimated the ductile capacity of the beams. The SDEM, in particular, underestimated the ductile capacity for most specimens, while the VEM produced slightly better ductility estimates.
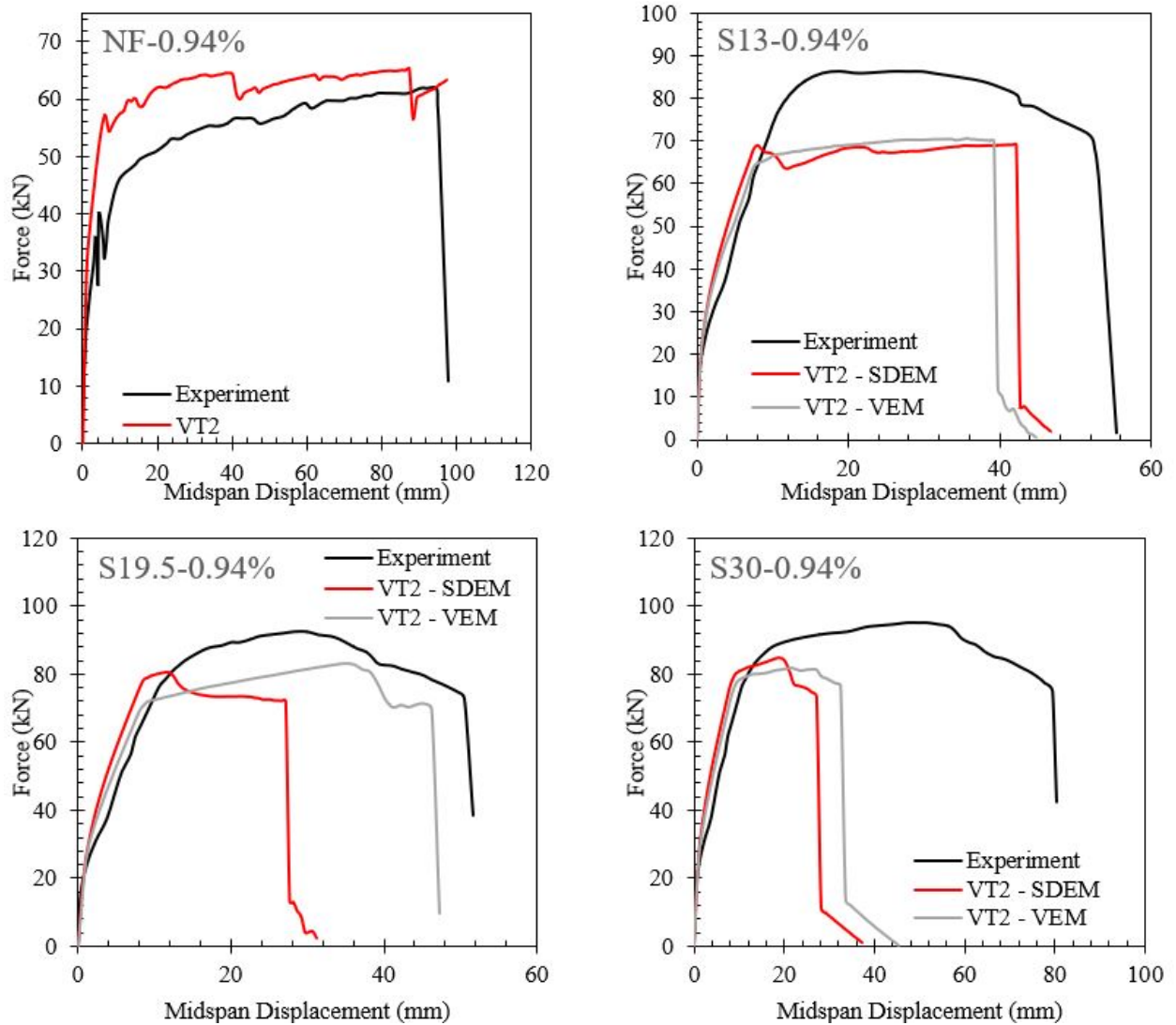
Figure 6.11: Experimental and VecTor2 force-displacement curves of beams tested by Yoon and Yoon (2015) for $\rho = 0.94\%$.
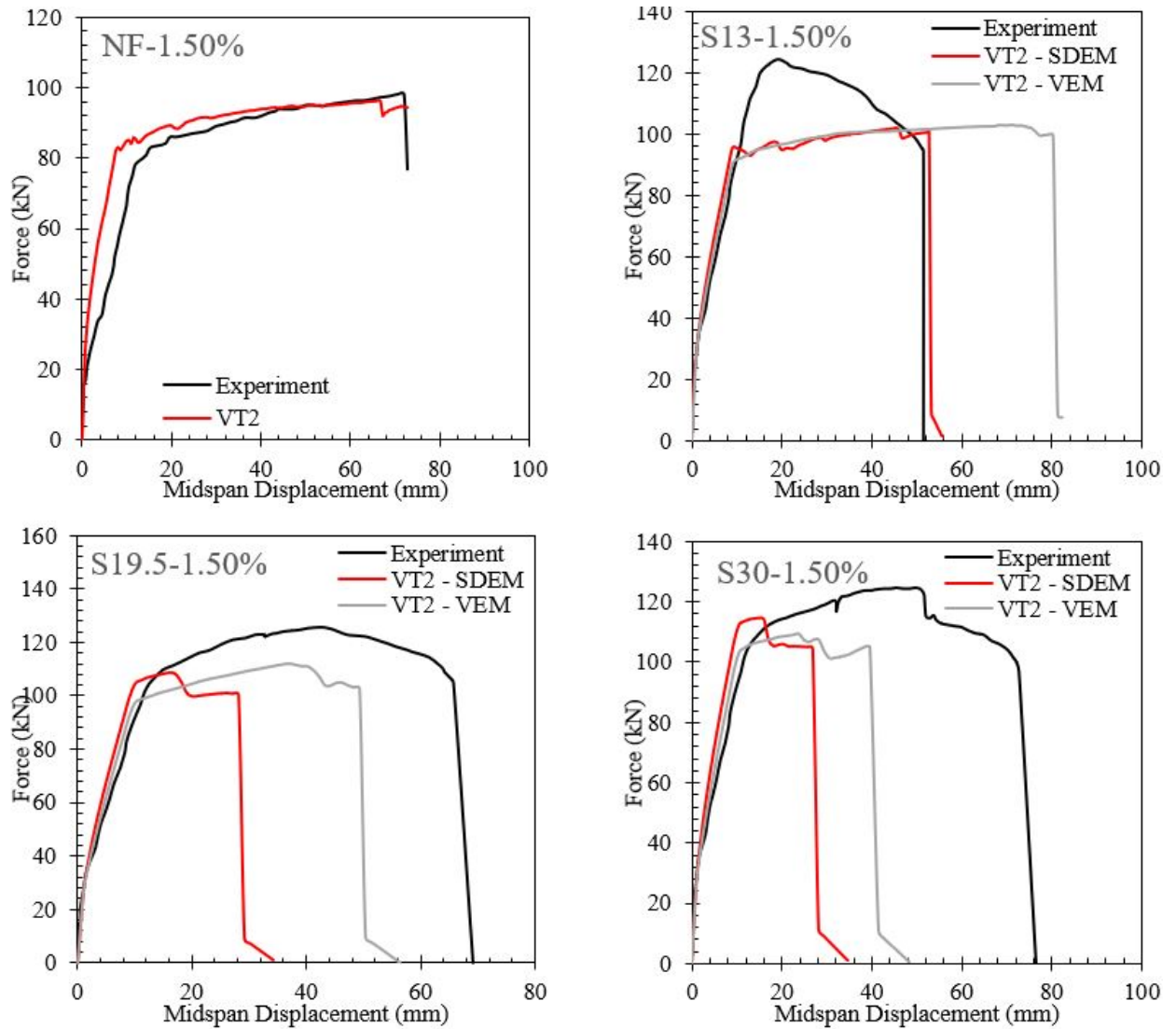
Figure 6.12: Experimental and VecTor2 force-displacement curves of beams tested by Yoon and Yoon (2015) for $\rho = 1.50\%$.

Yoo et al. (2016)

Yoo et al. (2016a) tested four simply-supported UHPFRC beams under symmetrical four-point bending to investigate the effect of longitudinal reinforcement ratio on flexural behaviour. All beams were of rectangular cross section, 200 mm in width, 270 mm in depth, and contained varying amounts of longitudinal reinforcement.

All material properties available from the testing program were used in the models. Longitudinal reinforcement was modelled as truss elements in the concrete, while fibres were modelled as smeared reinforcement. The beams in this experimental program did not contain transverse reinforcement. The input material properties for concrete and type of longitudinal reinforcement used for each specimen are shown in Table 6.20 and Table 6.21, respectively. The crack spacing values were taken as twice the maximum fibre length as per Equation 6.4 for all beams. All other material properties were reported by Yoo et al. (2016a).The fibre properties are shown in Table 6.22.

Table 6.20: Material properties used for finite element modelling of flexural beams tested by Yoo et al. (2016)

Specimen	Concrete						Reinforcement		
	f'_c	E_c	ε_o	a	s_x	s_y	Bottom Bars		
							Type	No. of	A_s
	MPa	MPa	x10^{-3}	mm	mm	mm		bars	mm^2
UH $-$ N	196.7	47800	4.40	0.5	26	26	-	-	-
UH $-$ 0.53%	196.7	47800	4.40	0.5	26	26	D13	2	253.4
UH $-$ 1.06%	196.7	47800	4.40	0.5	26	26	D13	4	506.8
UH $-$ 1.71%	196.7	47800	4.40	0.5	26	26	D13	6	760.2

Table 6.21: Longitudinal reinforcement properties. Yoo et al. (2016)

Bar	d_b	E_s	f_y	f_u	ε_u
	mm	MPa	MPa	MPa	x10^{-3}
D13	12.7	200000	522.7	627.6	164

Table 6.22: Steel fibre properties. Yoo et al. (2016)

| Fibre Type | V_f % | l_f mm | d_f mm | f_{uf} MPa |
| Straight | 2.0 | 13 | 0.2 | 2788 |

Figure 6.13 compares the experimental and VecTor2 simulated load-displacement curves for the four beams considered in this experimental program. Unlike the previous experimental programs,

this set of beams showed a more substantial variance between the results provided by SDEM and VEM. Although both models still underestimated the response, VEM significantly outperformed SDEM in predicting both the overall load-carrying capacity and the deformation capacity of the beams. The VecTor2 models also provided the most accurate predictions for Beam UH-1.71%, which contained the highest amount of longitudinal reinforcement ($\rho = 1.71\%$), and provided the least accurate predictions for Beam UH-N, which contained no longitudinal reinforcement. In this set of beams, the finite element models accurately captured the cracking load as well as accurately captured both the pre-cracking and post-cracking stiffnesses.
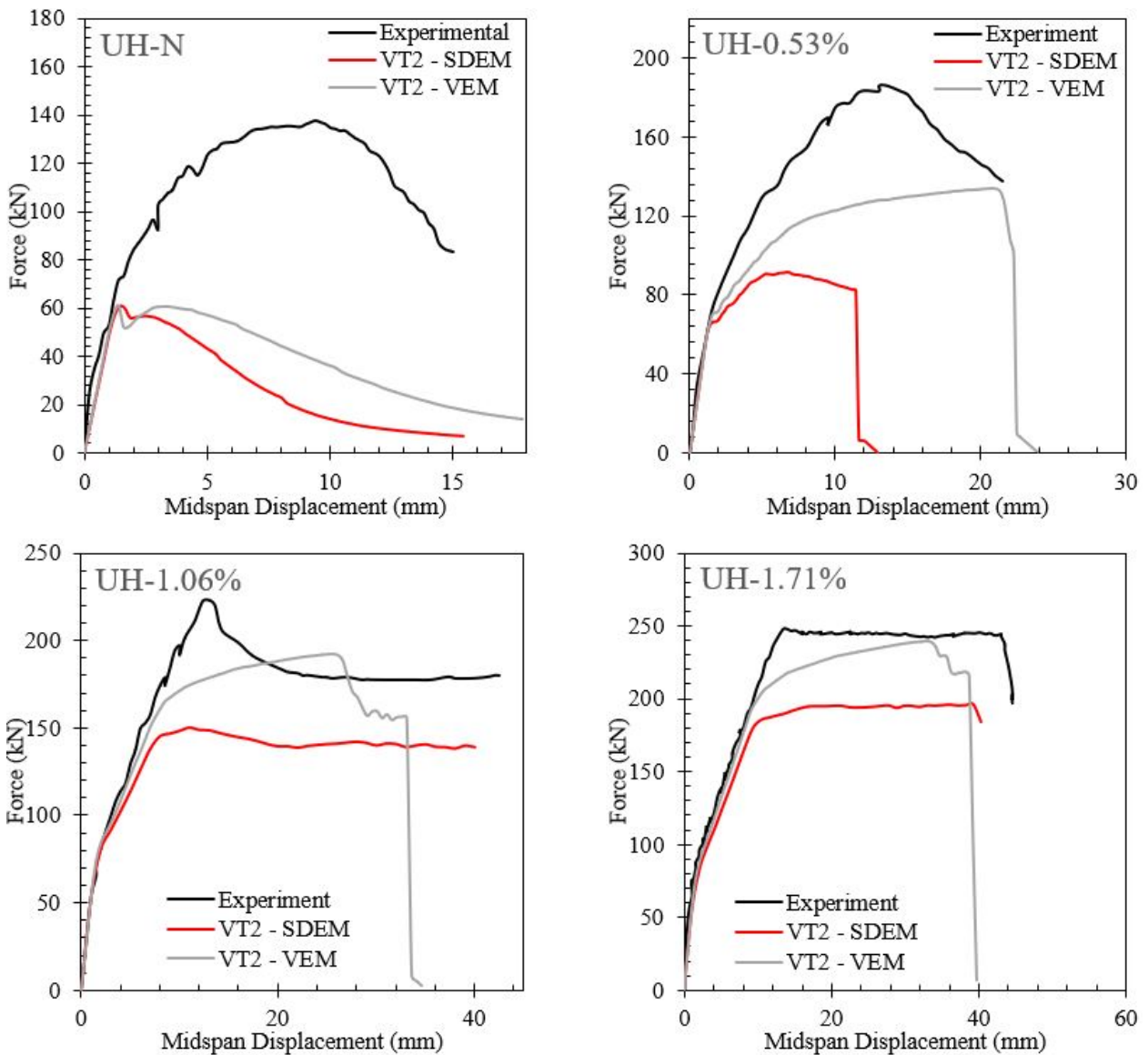

Figure 6.13: Experimental and VecTor2 force-displacement curves of beams tested by Yoo et al. (2016a).

Singh et al. (2017)

Singh et al. (2017) tested four simply-supported UHPFRC beams with varying span lengths and cross sections under different loading conditions. B25 beams were loaded under symmetrical four-point bending while B15 beams were tested under three-point bending. B25-1 and B25-2 were identical, while B15-1 and B15-2 had identical cross sections and reinforcement but differed in effective span lengths. All beams had square cross sections: B25 beams had a side length of 250 mm, while B15 beams had a side length of 150 mm. Using the results from the experimental investigation, Singh et al. (2017) also produced a finite element model using the concrete damaged plasticity model (CDP).

All material properties available from the testing program were used in the models. B15 beams contained D6 (d_b = 6 mm) closed stirrups at a spacing of 90 mm while B25 beams contained D10 (d_b = 10 mm) closed stirrups at a spacing of 90 mm. All transverse reinforcement was modelled as smeared vertical reinforcement within the concrete. The input material properties for concrete, along with the type of longitudinal reinforcement used for each specimen, are shown in Table 6.23. The crack spacing values were taken as twice the maximum fibre length as per Equation 6.4 for all beams. All other material properties were reported by Singh et al. (2017).The smeared reinforcement and longitudinal reinforcement properties are shown in Table 6.24 and Table 6.25, respectively. The yield and ultimate strengths of the D10 and D6 longitudinal reinforcement used were not reported and, as such, VecTor2 default values of 400 and 600 MPa were used in the analysis, respectively.

Table 6.23: Material properties used for finite element modelling of flexural beams tested by Singh et al. (2017)

Specimen	Concrete							Reinforcement					
								Bottom Bars			Top Bars		
	t	f'_c	f'_t	E_c	a	s_x	s_y	Type	No. of bars	A_s	Type	No. of bars	A_s
	mm	MPa	MPa	MPa	mm	mm	mm			mm^2			mm^2
B15 − 1	150	143	5.8	38470	1	70	70	D16	2	402	D16	2	402
B15 − 2	150	143	5.8	38470	1	70	70	D16	2	402	D16	2	402
B25 − 1	250	143	5.8	38470	1	70	70	D20	3	900	D10	2	157

Table 6.24: Smeared reinforcement properties Singh et al. (2017)

| Specimen | Fibre | | | | | Stirrup | |
	Type	V_f %	l_f mm	d_f mm	f_{uf} MPa	Type	ρ %
B15 − 1	End-Hooked	2.25	35	0.55	1100	D6	0.419
B15 − 2	End-Hooked	2.25	35	0.55	1100	D6	0.419
B25 − 1,2	End-Hooked	2.25	35	0.55	1100	D10	0.698

Table 6.25: Truss reinforcement properties Singh et al. (2017)

Bar	d_b mm	f_y MPa	f_u MPa
D20	20	525	625
D16	16	520	705
D10	10	400*	600*
D6	6	400*	600*

∗data unavailable; values assumed.

Figure 6.14 compares the experimental and VecTor2 simulated load-displacement curves for the three beams considered in this experimental program. Both SDEM and VEM models gave comparable results; however, unlike the previous beams, both models overestimated the ultimate load-carrying capacity of the beams. Despite this atypical overestimation, the VEM still provided a better estimate of the beam strength capacity.

Both the SDEM and VEM appear to overestimate the cracking load for all three beams. Although the pre-cracking stiffness was well captured, both the SDEM and VEM significantly overestimated the post-cracking stiffness. In addition, the highly ductile responses observed in the experimental results were not captured by the finite element models; both the SDEM and VEM substantially underestimated the deformation capacity of the beams. Failure in Beam 25-2 was due to the longitudinal D20 reinforcement rupturing at a midspan displacement of 128 mm. In VecTor2, failure was much earlier and was due to crushing of the concrete at midspan.
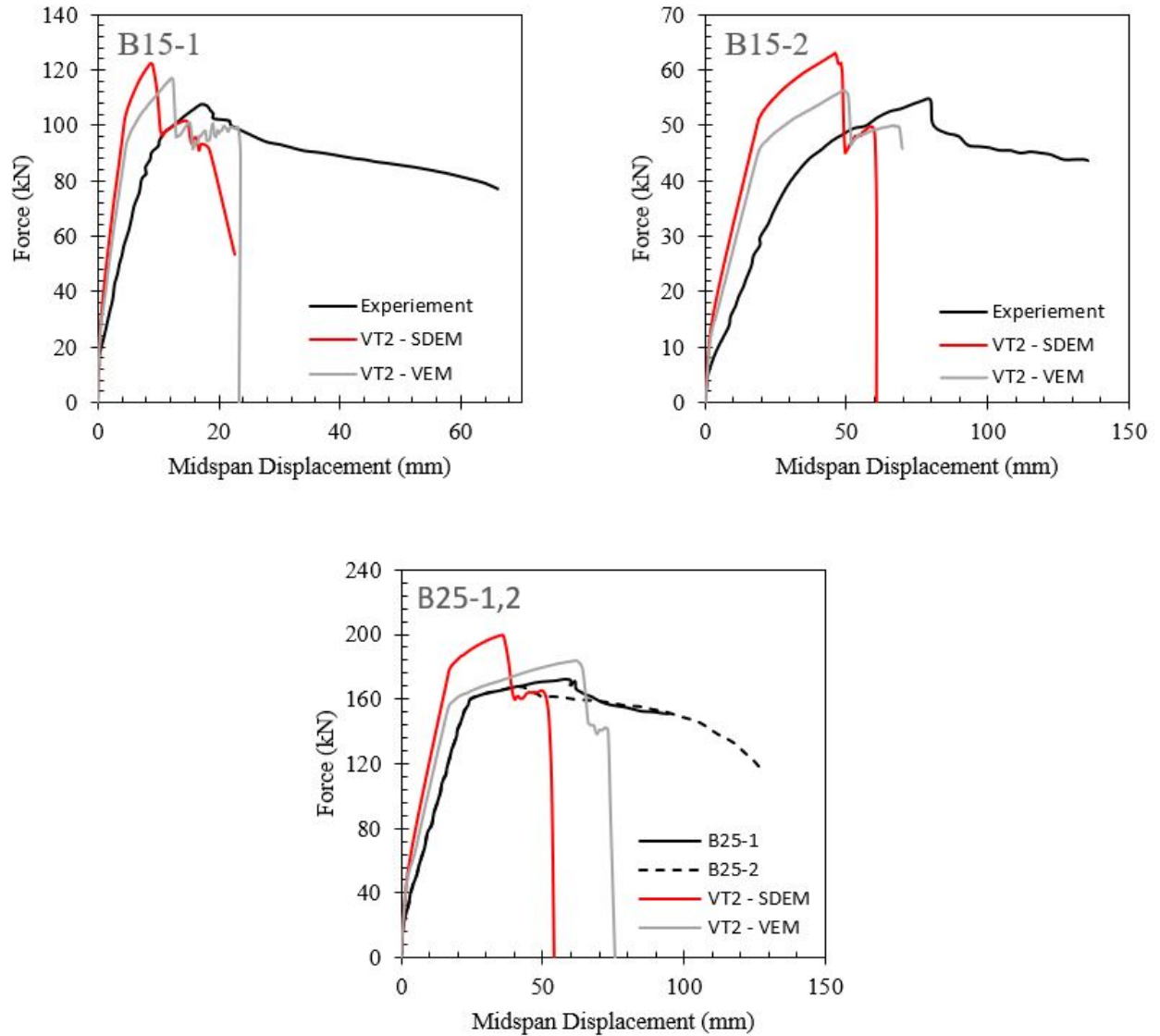
Figure 6.14: Experimental and VecTor2 force-displacement curves of beams tested by Singh et al. (2017).

Kodur et al. (2018)

Kodur et al. (2018) tested four large scale UHPFRC beam under flexural and shear loading. The investigated variables included longitudinal reinforcement ratio and type of loading. Beams U-B3 and U-B5 were tested under flexural loading while Beams U-B4 and U-B5 were tested under dominant shear loading. All beams had rectangular cross sections with an overall beam depth of 270 mm and contained two different amounts of longitudinal reinforcement.

All material properties available from the testing program were used in the models. Longitudinal reinforcement was modelled as truss elements in the concrete, while fibres were modelled as smeared

reinforcement. The beams in this experimental program did not contain transverse reinforcement. The input material properties for concrete and type of longitudinal reinforcement used for each specimen are shown in Table 6.26 and Table 6.27, respectively. The crack spacing values were taken as twice the maximum fibre length as per Equation 6.4 for all beams. All other material properties were reported by Dinh (2010).The fibre properties are shown in Table 6.28.

Table 6.26: Material properties used for finite element modelling of flexural beams tested by Kodur et al. (2018)

Specimen	Concrete						Reinforcement		
	t	f'_c	E_c	a	s_x	s_y	Bottom Bars		
							Type	No. of bars	A_s
	mm	MPa	MPa	mm	mm	mm			mm^2
UB3	180	167	40615	12.7	26	26	D13	3	398
UB4	180	167	40615	12.7	26	26	D13	3	398
UB5	180	167	40615	12.7	26	26	D13	4	531
UB6	180	167	40615	12.7	26	26	D13	4	531

Table 6.27: Longitudinal reinforcement properties. Kodur et al. (2018)

Bar	d_b %	E_s mm	f_y mm	f_u MPa	ε_u x10^{-3}
D13	13	200000	436	696	122

Table 6.28: Steel fibre properties. Kodur et al. (2018)

Fibre Type	V_f %	l_f mm	d_f mm	f_{uf} MPa
Straight	1.5	13	0.2	845

Figure 6.15 compares the experimental and VecTor2 simulated load-displacement response for the four beams considered. Models using SDEM and VEM gave comparable results for the beams tested, and both underestimated the ultimate load-carrying capacity. In Beams U-B3 and U-B5, which were tested under flexural dominant loading, experimental tensile cracking occurred at a load level of 26.2 kN and 28.4 kN, respectively. In Beams U-B4 and U-B6, which were tested under shear dominant loading, experimental tensile cracking occurred at a load level of 39.1 kN and 38.3 kN, respectively. The finite element models appear to capture these cracking loads well. However, when compared to the finite element models, the experimental results showed a more prominent pre-peak stiffness change between the uncracked and cracked response. In general, the finite element models were able to capture the pre-cracking stiffness well but overestimated the

post-cracking stiffness for all four beams tested. Lastly, reinforcement yield was experimentally observed in all four beams. This yielding was captured by both SDEM and VEM in all beams, although at a much lower load level, thus contributing to the lower predicted ultimate load-carrying capacity. After yielding, both SDEM and VEM captured a ductile response; however, neither model accurately captured the beams' deformation capacities. For Beams U-B3 and U-B5, both SDEM and VEM overestimated the deformation capacity, while for Beams U-B4 and U-B6, both models underestimated the deformation capacity. Both finite element models captured the opening of a diagonal shear crack near the loading point in Beams U-B3 and U-B4, which resulted in failure.
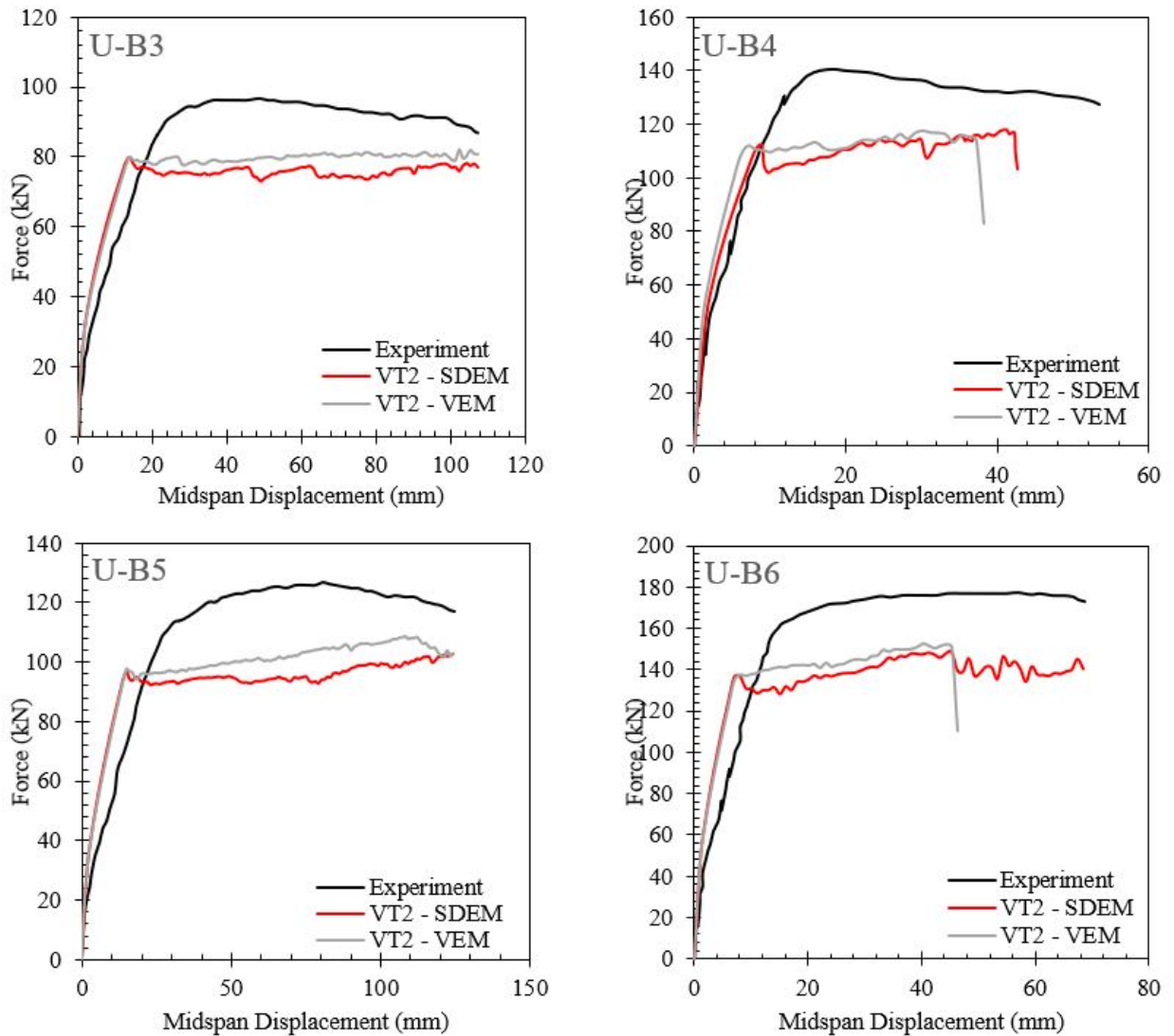

Figure 6.15: Experimental and VecTor2 force-displacement curves of beams tested by Kodur et al. (2018).

Figure 6.16 shows a comparison between the VecTor2 predicted ultimate capacity and the experimental ultimate capacity for all investigated UHPFRC beams. SDEM and VEM models gave comparable results with a mean of 0.83 and 0.84, respectively. VEM results showed a lower CoV of 22% compared to the SDEM CoV of 26%.
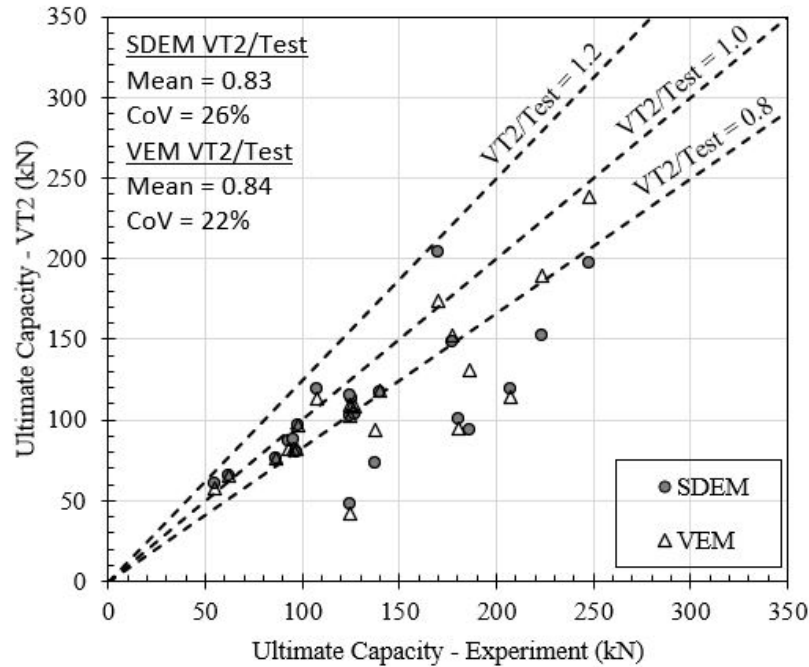
Figure 6.16: Comparison of VecTor2 predicted ultimate capacity and experimental capacity for UHPFRC members.

6.3.3 Multi-Element Modelling

A recurring concern in the VecTor2 analysis of UHPFRC beams tested under flexure and shear was its inability to capture the deformation capacity. A possible explanation could be VecTor2's response to localization for multi-element models. In the finite element algorithm, once a member is in the tension softening branch, even the slightest round-off error can result in a significant divergence of results between the individual elements.

To demonstrate this effect, two identical uniaxial tension members similar to those modelled for inverse analysis in Section 6.2.1 were modelled in VecTor2 using the material properties of Panel YS1. One model used a mesh of five identical sized elements, while the other used a single four-node plane stress rectangular element. The support and location conditions were identical to the uniaixal tension members modelled in Section 6.2.1, and are shown in Figure 6.17.

(a) Multi-element FormWorks model.

(b) Single-element FormWorks model

Figure 6.17: FormWorks models of a uniaxial tension member.

In analyzing the responses, the five-element model failed at a significantly smaller horizontal displacement of 15.6 mm, compared to the single-element model of 62.5 mm. Moreover, the effect of localization can be seen in the crack width values at a horizontal displacement of 15.5 mm, as shown in Figure 6.18. At this displacement within the tension softening branch, slight round-off errors can make certain elements appear weaker than the other. In Figure 6.18a, the weakest element is the middle element. This apparent weakness then results in diverging responses as some elements recoil and push the deformation to the middle element. The large concentration of local strains leads to a large crack width and the abrupt failure of the member. In the single element model, this local concentration is not present, and the member continues to strain in a stable manner. This tendency to diverge may explain VecTor2's inability to capture the ductile response of the UHPFRC members.
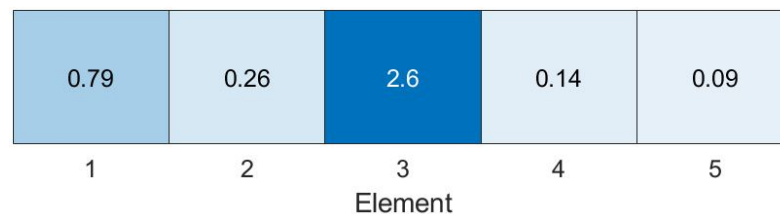
(a) Multi-element model.
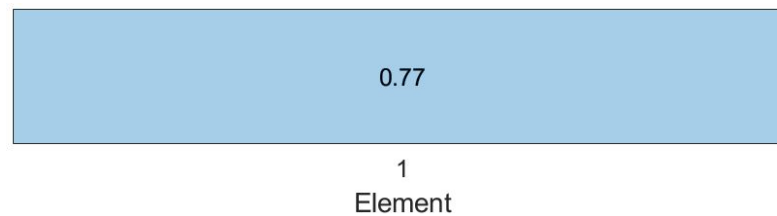
(b) Single-element model.

Figure 6.18: Comparison of crack widths of a multi-element model and single-element model.

6.4   Discussion

In general, the VecTor2 finite element models using SDEM and VEM did not adequately capture the response of UHPFRC pure shear panels, nor SFRC and UHPFRC beams tested under flexure and shear. When comparing the average predicted to experimental ultimate capacity ratios, VecTor2 models using VEM generally predicted more accurate results than using SDEM. In addition, VecTor2 models more accurately predicted the behaviour of SFRC members compared to UHPFRC members. This is expected since the existing constitutive models that account for the contribution of fibre reinforcement were developed based on the behaviour of SFRC and not adjusted to model UHPFRC. In predicting the response of UHPFRC pure shear panels, SDEM overestimated the ultimate shear capacity with a mean predicted to test ratio of 1.17, compared to the VEM mean predicted to test ratio of 1.00. In predicting SFRC beams tested under shear dominant loading, both SDEM and VEM underestimated the shear capacity, with predicted to test ratios of 0.91 and 0.93, respectively. Lastly, in predicting UHPFRC beams tested under flexure and shear loading, both SDEM and VEM underestimated the ultimate load-carrying capacity, with predicted to test ratios of 0.83 and 0.84, respectively. SDEM and VEM produced similar coefficient of variation for predicted to test ratio. The coefficient of variation was lowest for the UHPFRC shear panels and highest for the SFRC beams.

The analysis results indicate that both SDEM and VEM require additional improvements to accurately predict the behaviour of both SFRC and UHPFRC specimens. First, models using SDEM and VEM performed better when the tested specimens contained a higher percentage of conventional reinforcement. In the tests conducted by Yoo and Yoon (2015) and Yoo et al. (2016a), both the SDEM and VEM predicted the response more accurately in beams with higher reinforcement ratios. Moreover, the finite element models were unable to accurately predict the behaviour of UHPFRC pure shear panel YS3 (Yap, 2020), and UHPFRC Beams NR-1,2 (Yang et al., 2010) and UH-N (Yoo et al., 2016a), all of which had no conventional reinforcement. As such, recommendations for future work include further investigations on the effect of conventional reinforcement ratio on modelled behaviour. In particular, both SDEM and VEM require further formulation modifications in order to adequately consider modelled specimens without conventional reinforcement.

In addition, in modelling SFRC beams tested by Dinh (2010), a potential for size effect in modelled behaviour was observed. The B18 Beam Series, which were 455 mm in overall depth, produced higher VecTor2 predicted-to-test ratio than the B27 Beam Series, which were 685 mm in depth. However, a lower CoV was observed in the larger B27 Beam Series. Further investigations are required to validate the presence of this size effect in SFRC beams. In addition, the UHPFRC beams used in this validation study were limited to an overall depth between 150 mm and 270 mm and thus, this observation cannot be validated for UHPFRC specimens. Thus, recommendations for future work can include further experimental and numerical investigations on larger UHPFRC specimens.

Lastly, the presence of multiple close spaced cracks in UHPFRC is responsible for its improved tension stiffening behaviour and large post-yield load-carrying capacity. However, both SDEM and VEM were unable to consistently capture this observed deformation capacity. As seen in Chapter 3, the behaviour of the VecTor2 model is sensitive to the input maximum crack spacing used in the model. As such, the maximum input crack spacing used in this verification study of twice the maximum fibre length requires further scrutiny. While this assumption produced relatively positive results, this crack spacing parameter needs to be further investigated and validated to accurately predict behaviour.

6.5   SDEM/Franssen Modelling

One potential reason for VecTor2's tendency to underestimate both the strength and ductility of UHPFRC beams is that the strain-hardening behaviour may be limited due to the high input cracking strength and low fibre bond strength. To investigate this further, the modified material parameters proposed by Franssen et al. (2018) in modelling UHPFRC-strengthened members were investigated for their applicability in modelling UHPFRC beams.

The UHPFRC beams from Section 6.3.2 were remodelled to include three material input modifications. Specifically, two model parameter adjustments proposed by Franssen et al. (2018) were adopted in this investigation. First, in the SDEM, the bond strengths for straight and end-hooked fibres are defined as $\tau_{f,max} = 0.396\sqrt{f'_c}$ and $\tau_{f,max} = 0.429\sqrt{f'_c}$ MPa, respectively. Franssen et al. (2018) proposed an increase of this bond strength to $\tau_{f,max} = 0.75\sqrt{f'_c}$ MPa to account for the high density and high cement content of the UHPFRC matrix. Franssen et al. (2018) also incorporated a simple expression for the crack spacing using $s_{cr} = 0.75l_f$ mm, which

was shown to produce adequate results in modelling UHPFRC specimens.   In addition, the concrete cracking strength input for all UHPFRC beams was reverted to the default VecTor2 cracking stress of $f'_t = 0.33\sqrt{f'_c}$ MPa to further ensure a strain-hardening response after cracking. The UHPFRC beams were reanalyzed using the SDEM combined with these adjusted material inputs, and the results are described in the following sections. Overall, the modifications to the fibre bond strength and crack spacing significantly improved the post-cracking response of the UHPFRC beams.

Yang et al. (2010)

Figure 6.19 shows a comparison between the experimental and SDEM/Franssen VecTor2 model responses for beams tested by Yang et al. (2010).   Although the SDEM/Franssen model underestimated the strength capacity and overestimated the ductility of the beams, modifying the fibre bond strength and crack spacing resulted in significant improvements to the modelled behaviour, compared to the SDEM and VEM. Both the post-cracking stiffness and the strength capacity of the SDEM/Franssen model responses matched the experimental results more closely. Similar to the SDEM and VEM, the SDEM/Franssen grossly underestimated the strength capacity of Beam NR, which contained no conventional longitudinal reinforcement. Since Yang et al. (2010) did not report experimental cracking strengths for the beams tested, the SDEM/Franssen model predicted the same cracking loads as the SDEM and VEM.

Figure 6.19: Experimental and VecTor2 force-displacement curves of beams tested by Yang et al. (2010) using modified material parameters.

Yoo and Yoon (2015)

Compared to the SDEM and VEM, the SDEM/Franssen model showed an increase in load-carrying capacity for beams tested by Yoo and Yoon (2015). As shown in Figure 6.20, however, the SDEM/Franssen model overestimated the strength capacity for all beams except for Beam S13-1.50%. Beams NF-0.94% and NF-1.50% did not contain any fibre reinforcement, and thus, the SDEM/Franssen model produced no changes in modelled behaviour. Additionally, compared to the SDEM and VEM, the SDEM/Franssen model captured the ductility response better in Beams S30-0.94% and S30-1.50%, which contained 30 mm long fibres, but worsened the response in Beams S13-0.94% and S13-1.50%, which contained 13 mm long fibres. Again, since Yoo and Yoon (2015) did not report cracking strengths for the beams tested, the SDEM/Franssen

model predicted the same cracking loads as the SDEM and VEM.

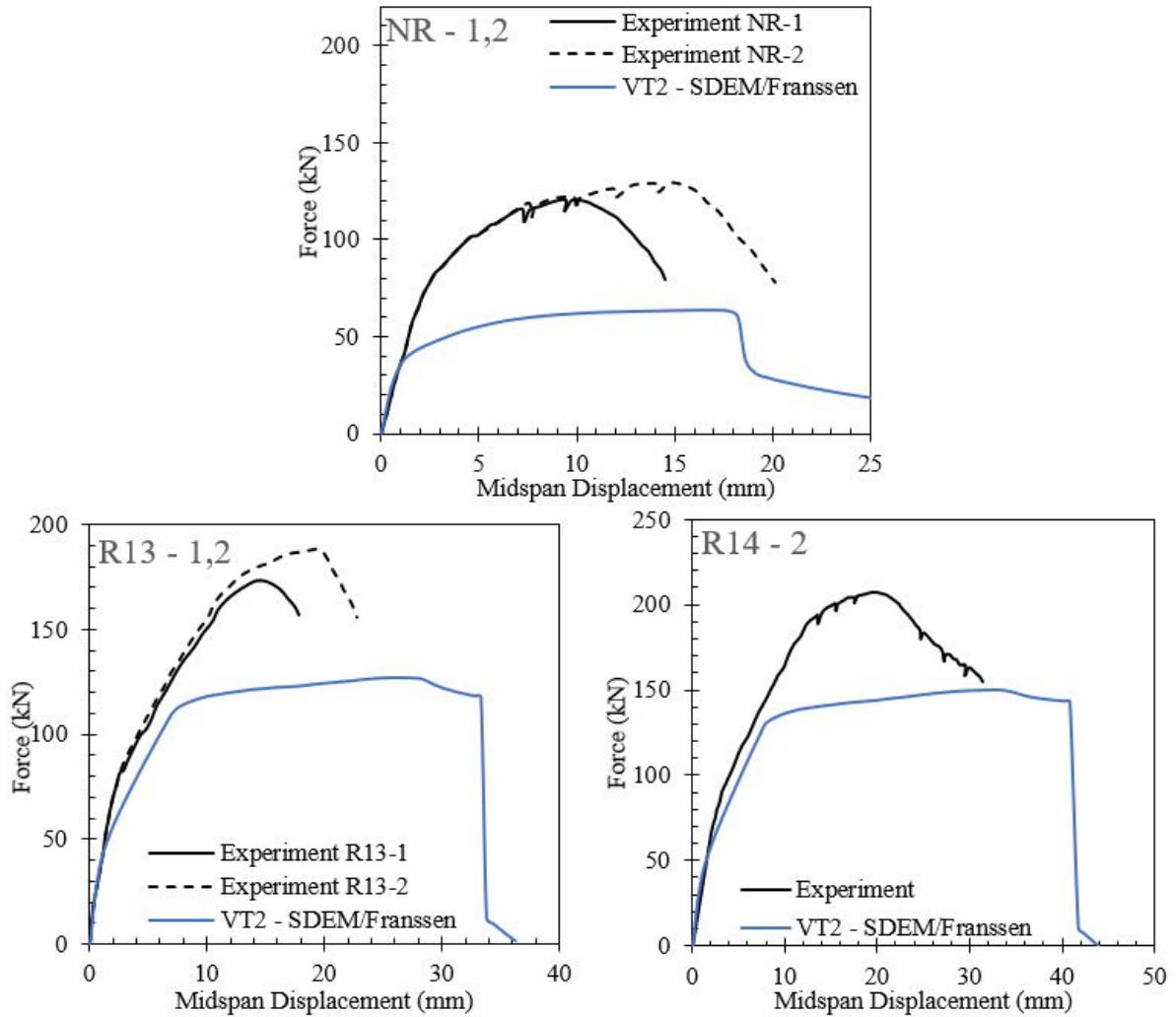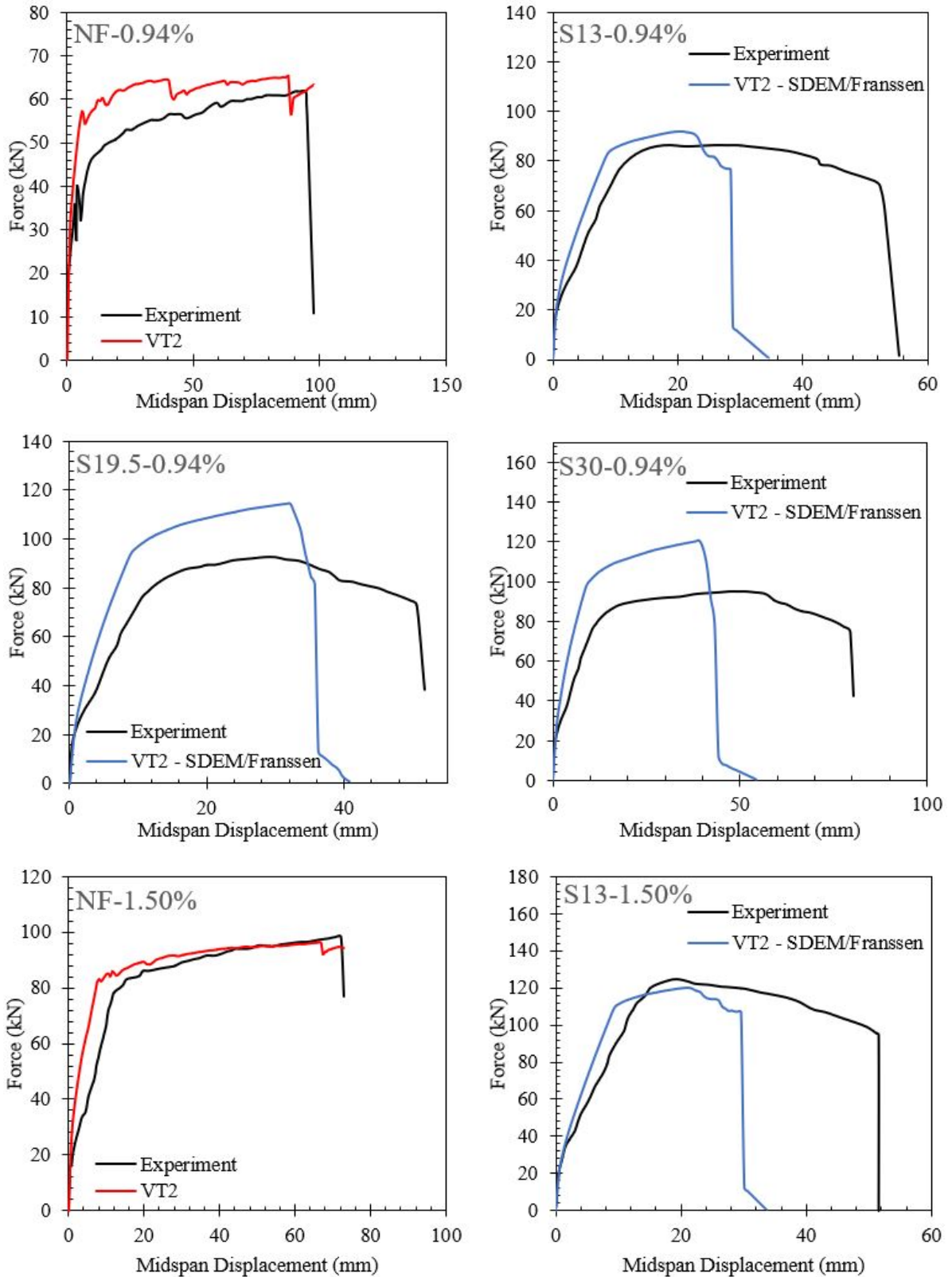Figure 6.20: Experimental and VecTor2 force-displacement curves of beams tested by Yoo and Yoon (2015) using modified material parameters.

Yoo et al. (2016)

In beams tested by Yoo et al. (2016a), modifying the fibre bond strength and crack spacing resulted in significant improvements to the modelled behaviour. Compared to the SDEM and VEM, the SDEM/Franssen models better captured both the ultimate strength capacity and the beams' ductility. In particular, the SDEM/Franssen model response best matched the experimental results for Beam UH-1.71%. In contrast, the SDEM/Franssen model grossly underestimated the strength capacity of Beam UH-N, which contained no conventional longitudinal reinforcement. Lastly, compared to the SDEM and VEM, the SDEM/Franssen also underestimated the cracking load, as expected with the use of the lower-bound default VecTor2 cracking strength.

Figure 6.21: Experimental and VecTor2 force-displacement curves of beams tested by Yoo et al. (2016a) using modified material parameters.

Singh et al. (2017)

In beams tested by Singh et al. (2017), as shown in Figure 6.22, the SDEM/Franssen model underestimated the ductility and overestimated both the post-cracking stiffness and the ultimate strength capacity. Compared to the SDEM, modifying the fibre bond strength and crack spacing resulted in only minor improvements to the modelled behaviour. The SDEM/Franssen model also slightly better captured the beams' cracking loads with the use of the default VecTor2 cracking strength. Overall, the VEM response best matched the experimental results in this set of beams.
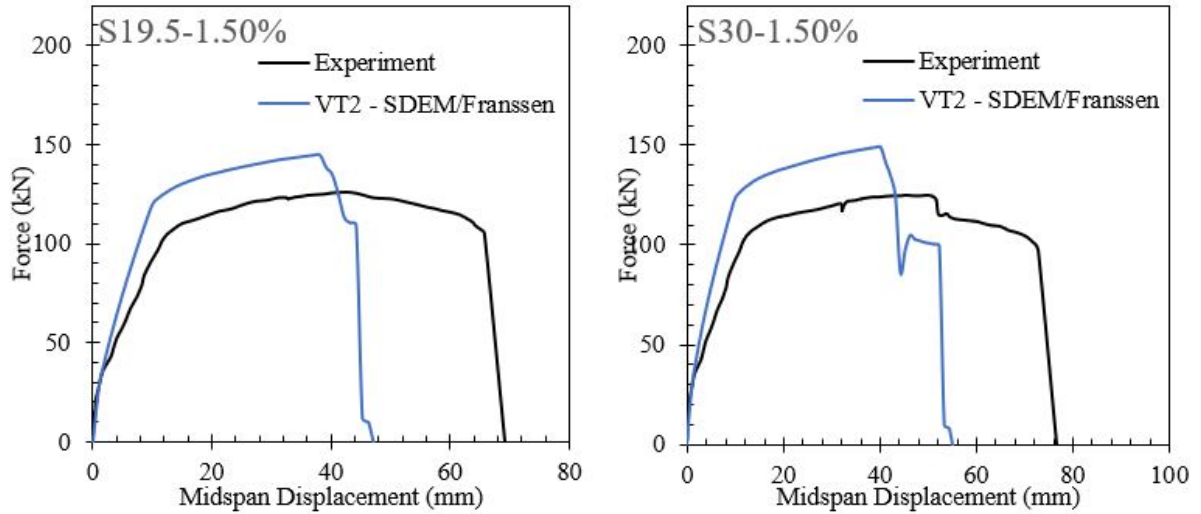
Figure 6.22: Experimental and VecTor2 force-displacement curves of beams tested by Singh et al. (2017) using modified material parameters.

Kodur et al. (2018)

In beams tested by Kodur et al. (2018), modifying the bond strength and crack spacing resulted in significant improvements to the modelled response. Compared to the SDEM and VEM, the SDEM/Franssen model results much more closely matched the experimental strength capacity for all four beams. The SDEM/Franssen model appears to slightly overestimate the strength capacity of the beams tested under flexure (U-B3 and U-B5), compared to those tested under shear (U-B4 and U-B6). Lastly, since Kodur et al. (2018) did not report cracking strengths for the beams tested, the SDEM/Franssen model predicted the same cracking loads as the SDEM and VEM.
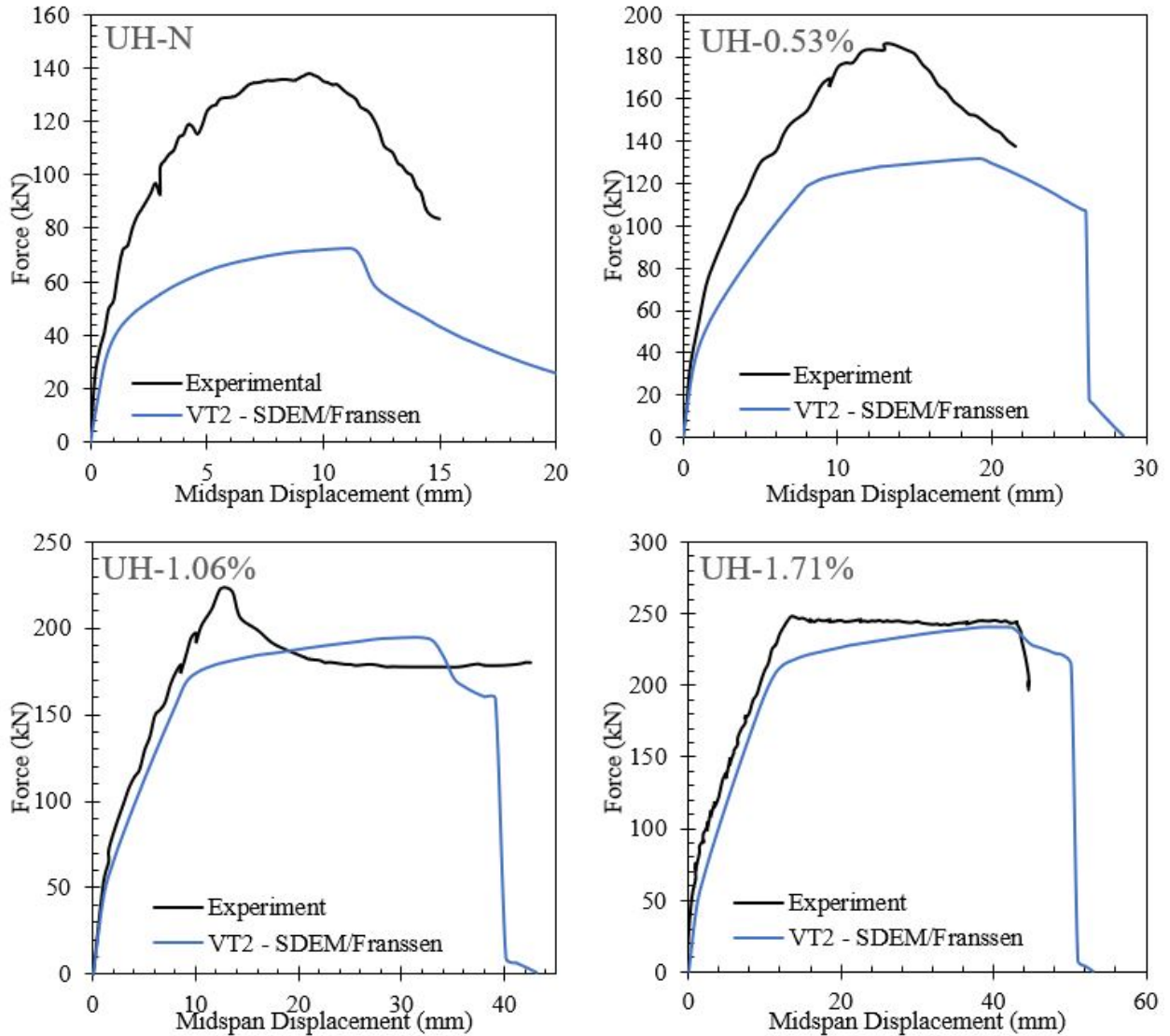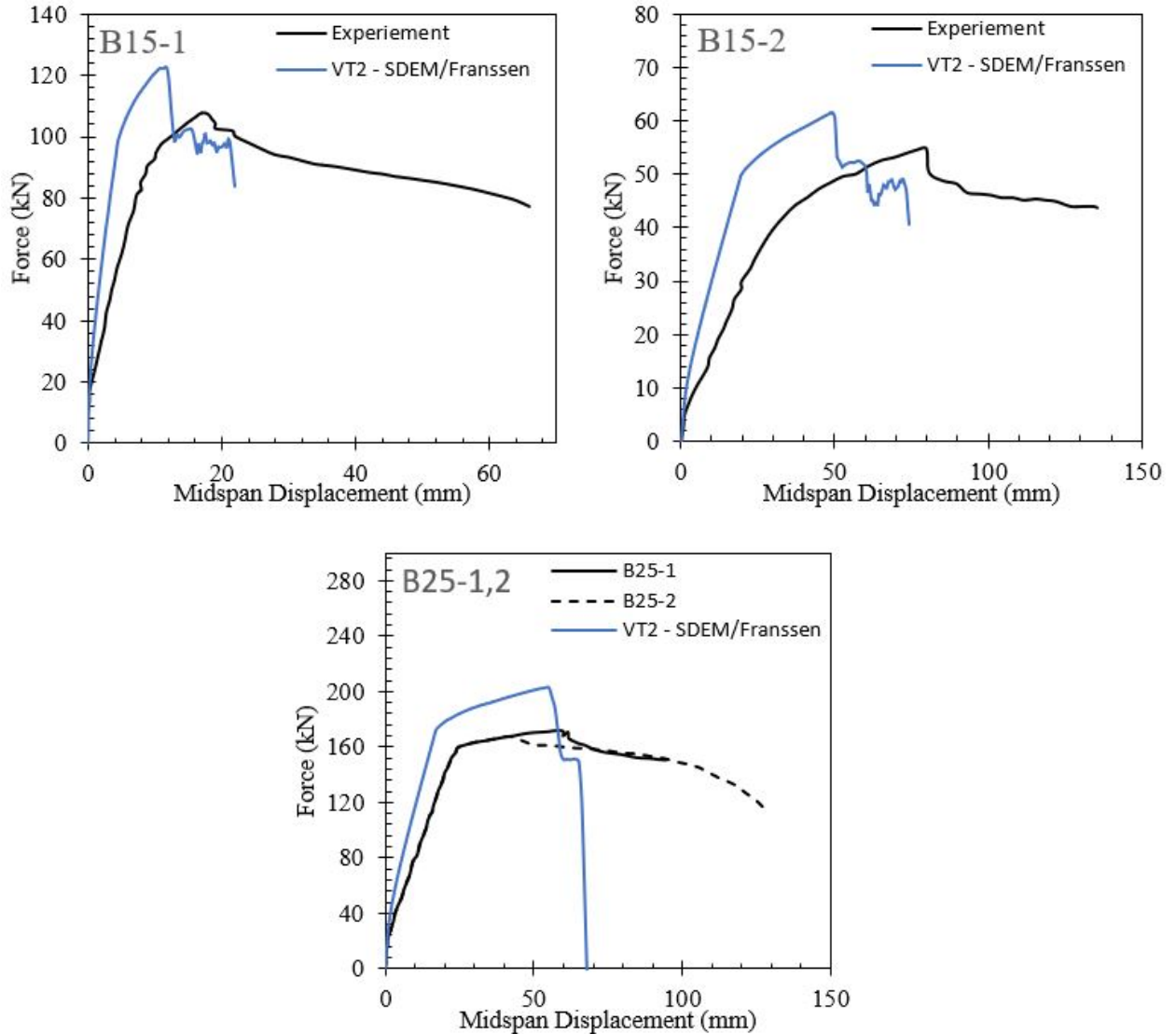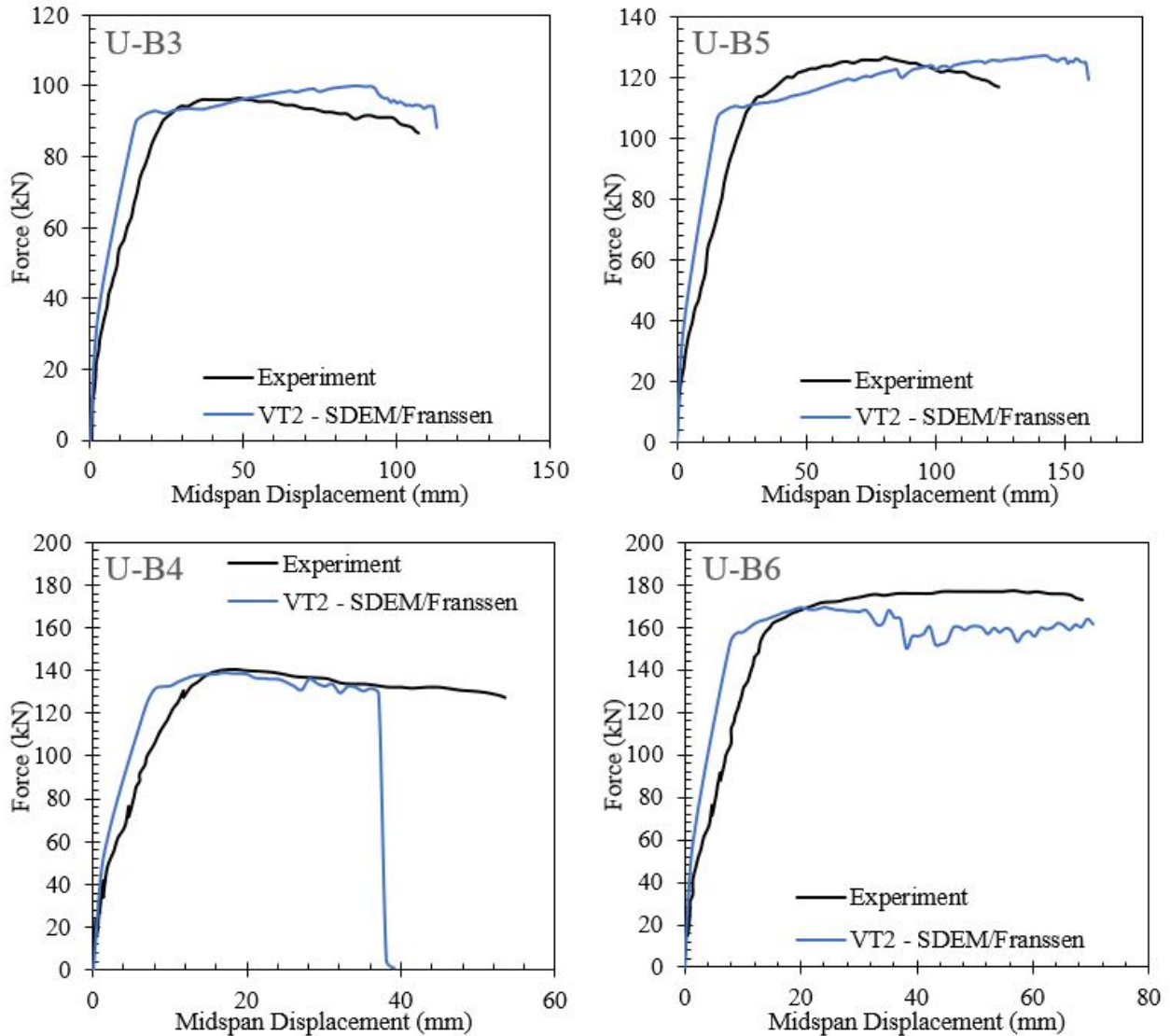
Figure 6.23: Experimental and VecTor2 force-displacement curves of beams tested by Kodur et al. (2018) using modified material parameters.

Table 6.29 and Figure 6.24 show the comparison between the experimental peak load, $P_{u,EXP}$, and the VecTor2 peak load using the SDEM/Franssen model parameters, $P_{u,SDEM/Franssen}$. The average VecTor2 calculated-to-experimental ultimate capacity ratio was 0.97, significantly higher than the ratios produced by the SDEM and VEM of 0.83 and 0.84, respectively. The SDEM/Franssen results also showed a lower coefficient of variation of 22% compared to the SDEM CoV of 26%. This suggests that when compared to the SDEM, the modified parameters both improved the accuracy of the results as well as reduced the variability in predicted responses. As a result, both higher bond stresses and lower crack spacing values appear warranted for UHPFRC.

Although both the increase in bond strength and decrease in crack spacing generally resulted in improved VecTor2 calculated responses, further investigations are necessary to confirm their validity. In particular, the crack spacing input needs to be considered further as the equation $s_{cr} = 0.75l_f$ results in a crack spacing of less than 10 mm for beams containing 13 mm long fibres. Considering the pure shear panels tested by Yap (2020) showed an average crack spacing of approximately 50 mm, a value of this low may be inaccurate. Thus, although reducing the crack spacing improved the response of UHPFRC, further investigations are required.

Table 6.29: Experimental and VecTor2 peak load for various UHPFRC beams tested

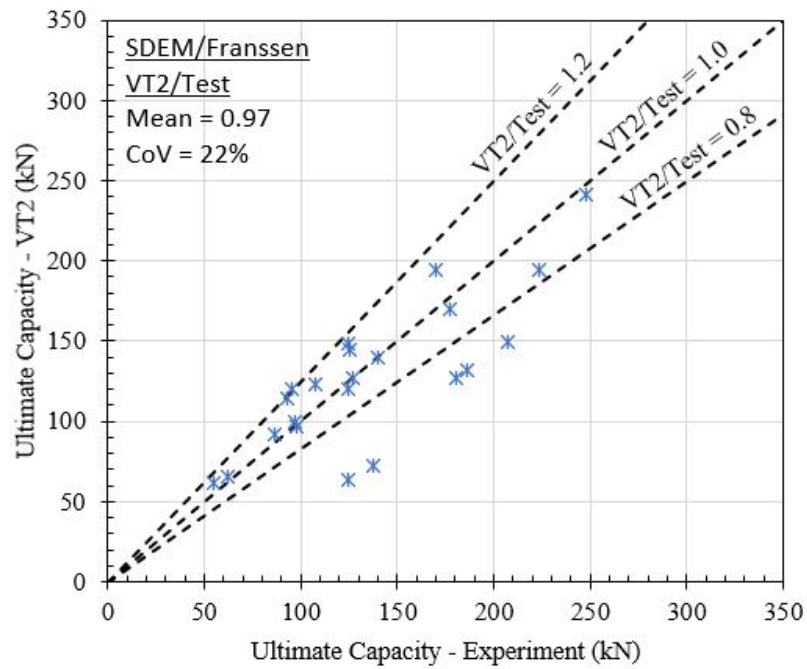| Author	Specimen ID	$P_{u,EXP}$ Experiment (1) kN	$P_{u,SDEM/Franssen}$ SDEM (2) kN	$\frac{P_{u,SDEM/Franssen}}{P_{u,EXP}}$ SDEM/Franssen (2)/(1)
Yang et al. (2010)	R13	181	127	0.70
	R14-2	207	150	0.72
	NR	125	63	0.51
Yoo and Yoon (2015)	NF-0.94	62	65	1.05
	S13-0.94	86	92	1.07
	S19.5-0.94	93	114	1.23
	S30-0.94	95	120	1.26
	NF-1.50	98	96	0.98
	S13-1.50	124	120	0.97
	S19.5-1.50	126	144	1.15
	S30 − 1.50	125	149	1.19
Yoo et al. (2016)	UH − N	138	73	0.53
	UH − 0.53%	186	132	0.71
	UH − 1.06%	223	194	0.87
	UH − 1.71%	248	241	0.97
Singh et al. (2017)	B15 − 1	108	123	1.14
	B15 − 2	55	61	1.12
	B25 − 1,2	170	195	1.15
Kodur et al. (2018)	U-B3	97	100	1.04
	U-B4	140	139	0.99
	U-B5	127	127	1.00
	U-B6	177	170	0.96
			Mean	0.97
			CoV	22%

Figure 6.24: Comparison of VecTor2 predicted ultimate capacity and experimental capacity for UHPFRC members using modified model parameters from Franssen et al. (2018).

Chapter 7

Conclusion and Recommendations

This study's main objective was to investigate, modify, and improve existing finite element analysis models in VecTor2 to extend its capabilities in modelling UHPFRC members. To accomplish this objective, existing constitutive models in VecTor2 were compared and investigated for their applicability in modelling UHPFRC. Using data from five large-scale pure shear tests, a finite element model was developed and validated for its capabilities in analyzing UHPFRC members.

7.1 Conclusion

In light of the analytical work performed, the following conclusions can be made:

- The preliminary parametric studies of a UHPFRC shear panel indicated that the concrete tensile strength, aggregate size, crack spacing, FRC tension model, and element thickness significantly influenced the modelled response. In particular, the default crack spacing formulation within VecTor2 does not represent the material's response well. When modelling UHPFRC in VecTor2, it is recommended where possible that the crack spacing value found through testing be used until more reliable crack spacing formulations are developed.

- A reinforcement rupture formulation developed from a regression analysis improves the prediction of rupture strain in reinforced concrete specimens tested under uniaxial tension. Further research is necessary to expand and validate this formulation for UHPFRC members.

- The FRC constitutive models in VecTor2 can be extended to capture the response of UHPFRC pure shear panels sufficiently well. This improvement was accomplished by including an effective aggregate size formulation and modifying the crack width calculations for UHPFRC. These additions significantly improved the analytical response.

- Using tension softening models derived from the inverse analysis of test prisms can lead to grossly unconservative predictions of strength and ductility. In contrast, using the results from direct tension test specimens in the custom tension softening curve may increase the accuracy

of the finite element models. However, additional experimental and analytical research is required.

- Currently, both the SDEM and VEM can accurately capture the response of strain-softening steel fibre reinforced concrete beams subjected to flexure and shear. Particularly, VecTor2 better captured the response of beams with lower compressive strengths and higher longitudinal reinforcement ratios. Thus, the current VecTor2 stiffness formulation may be more suitable for fibre reinforced concrete with normal compressive strengths. Further optimization is required for high strength fibre reinforced concrete containing low conventional reinforcement.

- Despite the modifications made through this study, the SDEM and VEM, as currently configured and calibrated, still suffer in accuracy when applied to UHPFRC. Although the pure shear UHPFRC panel results were acceptable, the strength and post-cracking stiffness captured in UHPFRC beams were both inaccurate and inconsistent. The VEM performed marginally better than the SDEM in capturing the ultimate strength and deformation capacities of these UHPFRC members.

- As per Franssen et al. (2018), increasing the fibre bond stress and modifying the crack spacing parameter lead to substantially improved results. Thus, the SDEM and VEM may be potentially viable platforms for accurately modelling UHPFRC beams, provided that better models for fibre bond stress and crack spacing are developed.

7.2 Recommendations for Future Work

As a new material, UHPFRC behaviour is complex and merits considerable experimental and numerical investigation. Thus, in light of the conclusions drawn above, limitations and deficiencies were also identified. The following outlines some recommendations for future work to further improve the analytical modelling of UHPFRC members:

- Conduct additional tests to strengthen the conclusions of this work and ensure they are valid under all conditions. Notably, further experimental testing on fibre bond stress, crack spacing, and reinforcement rupture in UHPFRC members is necessary to validate and improve the model formulations made in this research.

- Explore further the potential for size effect in SFRC and UHPFRC beams through additional experimental programs. Consequently, develop a finite element model to consider this effect in modelling members of all sizes.

- Develop standardized testing methods for the input parameters required by VecTor2 to produce accurate finite element models. In particular, it is necessary to develop a standardized testing method for determining the tensile strength of UHPFRC since the default equation $f'_t = 0.33\sqrt{f'_c}$ used for reinforced concrete is an overly conservative estimate of cracking stress for UHPFRC.

- Modify and improve the VecTor2 algorithms to eliminate localization within the tension softening branch. This may involve developing a more sophisticated finite element algorithm.

- Further investigate and develop a suitable fibre bond stress and crack spacing model for UHPFRC. These models should especially consider the effects of its uniquely dense matrix composition and its tendency to form multiple, closely spaced cracks. In addition, further investigations are required to develop a suitable model for UHPFRC without conventional reinforcement.

Ultimately, it is hoped that the research summarized in this thesis may improve the collective understanding of UHPFRC behaviour, and provide a useful tool for the analysis and design of UHPFRC structural members.

References

Bazant, Z. P. (2002). Concrete fracture models : testing and practice. *Engineering Fracture Mechanics*, 69:165–205.

Bentz, E. (2010). Augustus: Post Processor for VecTor2 (Version 5.6.0).

Bentz, E. C. (2005). Explaining the Riddle of Tension Stiffening Models for Shear Panel Experiments. *Journal of Structural Engineering*, 131(November):946–955.

CEB-FIP (1978). *Model Code for Concrete Structures: CEB-FIP International Recommendations.* Comité Euro-International du Béton, Paris.

Chen, L. and Graybeal, B. A. (2011a). Modeling Structural Performance of Second-Generation Ultrahigh-Performance Concrete Pi-Girders. *Journal of Bridge Engineering*, 17(4):634–643.

Chen, L. and Graybeal, B. A. (2011b). Modeling Structural Performance of Ultrahigh Performance Concrete I-Girders. *Journal of Bridge Engineering*, 17(5):754–764.

Collins, M. and Mitchell, D. (1997). *Prestressed Concrete Structures.* Response Publications, Toronto and Montreal, Canada.

Deluce, J. R. (2011). Cracking behaviour of steel fibre reinforced concrete containing conventional steel reinforcement. page 506.

Deluce, J. R., Seong-Cheol, L., and Vecchio, F. J. (2014). Crack model for steel fiber-reinforced concrete members containing conventional reinforcement. *ACI Structural Journal*, 111(1):93–102.

Dinh, H. H. (2010). *Shear behavior of steel fiber reinforced concrete beams without stirrup reinforcement.* PhD thesis.

Fischer, G. and Li, V. C. (2002). Influence of matrix ductility on tension-stiffening behavior of steel reinforced engineered cementitious composites (ECC). *ACI Structural Journal*, 99(1):104–111.

Franssen, R., Guner, S., Courard, L., and Mihaylov, B. (2018). A study on the numerical modelling of UHPFRC-strengthened members. *MATEC Web of Conferences*, 199:09001.

Hoshikuma, J., Kawashima, K., Nagaya, K., and Taylor, A. (1997). Stress-Strain Model for Confined Reinforced Concrete in Bridge Piers. *ASCE Journal of Structural Engineering*, 123(5):624–633.

Hunter, M. D. (2016). *Towards Stochastic Finite Element Analysis of Reinforced Concrete Structures.* Master thesis, University of Toronto.

Kang, S. B., Tan, K. H., Zhou, X. H., and Yang, B. (2017). Influence of reinforcement ratio on tension stiffening of reinforced engineered cementitious composites. *Engineering Structures*, 141:251–262.

REFERENCES

Kodur, V., Solhmirzaei, R., Agrawal, A., Aziz, E. M., and Soroushian, P. (2018). Analysis of flexural and shear resistance of ultra high performance fiber reinforced concrete beams without stirrups. *Engineering Structures*, 174(July):873–884.

Larsen, I. L. and Thorstensen, R. T. (2020). The influence of steel fibres on compressive and tensile strength of ultra high performance concrete: A review. *Construction and Building Materials*, 256.

Lee, S. C., Cho, J. Y., and Vecchio, F. J. (2011a). Diverse Embedment Model for Steel Fiber-Reinforced Concrete Elements in Tension: Model Verification. *ACI Materials Journal*, 108(5):526–535.

Lee, S. C., Cho, J. Y., and Vecchio, F. J. (2011b). Model for post-yield tension stiffening and rebar rupture in concrete members. *Engineering Structures*, 33(5):1723–1733.

Lee, S. C., Cho, J. Y., and Vecchio, F. J. (2013a). Simplified Diverse Embedment Model for Steel Fiber-Reinforced Concrete Elements in Tension: Model Verification. *ACI Materials Journal*, 110(4):403–412.

Lee, S. C., Cho, J. Y., and Vecchio, F. J. (2013b). Tension-stiffening model for steel fiber-reinforced concrete containing conventional reinforcement. *ACI Structural Journal*.

Luo, J. W. (2014). Behaviour and Analysis of Steel Fibre-Reinforced Concrete under Reversed Cyclic Loading. page 315.

Marti, P., Pfyl, T., Sigrist, V., and Ulaga, T. (1999). Harmonized test procedures for steel fiber-reinforced concrete. *ACI Materials Journal*, 96(6):676–685.

Mayer, U. and Eligehausen, R. (1998). Bond behaviour of ribbed bars at inelastic steel strains. *Proceedings of 2nd International Ph. D. . . .*, 10080(January 1998):1–8.

Moreno, D. M., Trono, W., Jen, G., Ostertag, C., and Billington, S. L. (2014). Tension stiffening in reinforced high performance fiber reinforced cement-based composites. *Cement and Concrete Composites*, 50:36–46.

Naaman, A. E. (2008). High Performance Fiber Reinforced Cement Composites: Classification and Applications. In *CBM-CI International Workshop*, pages 389–401, Karachi, Pakistan.

Nguyen, W., Bandelt, M. J., Trono, W., Billington, S. L., and Ostertag, C. P. (2019). Mechanics and failure characteristics of hybrid fiber-reinforced concrete (HyFRC) composites with longitudinal steel reinforcement. *Engineering Structures*, 183(November 2018):243–254.

Richard, P. and Cheyrezy, M. (1995). Composition of reactive powder concretes. *Cement and Concrete Research*, 25(7):1501–1511.

REFERENCES

Singh, M., Sheikh, A. H., Mohamed Ali, M. S., Visintin, P., and Griffith, M. C. (2017). Experimental and numerical study of the flexural behaviour of ultra-high performance fibre reinforced concrete beams. *Construction and Building Materials*, 138:12–25.

Solhmirzaei, R. and Kodur, V. K. (2017). Modeling the response of ultra high performance fiber reinforced concrete beams. *Procedia Engineering*, 210:211–219.

Susetyo, J. (2009). Fibre reinforcement for shrinkage crack control in prestressed, precast segmental bridges. page 502.

Telleen, K., Noshiravani, T., Galrito, R., and Bruhwiler, E. (2010). Experimental investigation into the shear resistance of a reinforced UHPFRC web element. *8th fib PhD Symposium in Kgs. Lyngby, Denmark*, (January 2010).

Vecchio, F. J. (1990). VecTor2 Nonlinear Finite Element Analysis.

Vecchio, F. J. (2000). Disturbed stress field model for reinforced concrete: Formulation. *Journal of structural engineering New York, N.Y.*, 126(9):1070–1077.

Vecchio, F. J. and Collins, M. P. (1986). Modified Compression-Field Theory for Reinforced Concrete Elements Subjected To Shear. *Journal of the American Concrete Institute*, 83(2):219–231.

Voo, J. Y. L. and Foster, S. (2003). Variable Engagement Model for the Design of Fibre Reinforced Concrete Structures. *Advanced Materials for Construction of Bridges, Buildings, and Other Structures III*, pages 1–11.

Voo, J. Y. L., Foster, S. J., and Gilbert, R. (2003). *Experimental Tests of Reactive Powder Concrete Beams failing in Shear*. UNICIV Report R-421, School of Civil and Environmental Engineering, The University of New South Wales.

Voo, Y. L., Poon, W. K., and Foster, S. J. (2010). Shear Strength of Steel Fiber-Reinforced Ultrahigh- Performance Concrete Beams without Stirrups. *Journal of Structural Engineering*, 136(11):1393–1400.

Walraven, J. C. (1981). Fundamental Analysis of Aggregate Interlock. *ASCE Journal of the Structural Division*, 107(11):2245–2270.

Wong, P., Vecchio, F., and Trommels, H. (2013). *VecTor2 & Formworks User's Manual, Second Edition*.

Yang, I. H., Joh, C., and Kim, B. S. (2010). Structural behavior of ultra high performance concrete beams subjected to bending. *Engineering Structures*, 32(11):3478–3487.

Yap, B. (2020). Behaviour of Ultra High Performance Fibre Reinforced Concrete Subjected to Pure Shear. Master's thesis, University of Toronto.

REFERENCES

Yin, H., Shirai, K., and Teo, W. (2019). Finite element modelling to predict the flexural behaviour of ultra-high performance concrete members. *Engineering Structures*, 183(March 2018):741–755.

Yoo, D.-Y., Banthia, N., and Yoon, Y.-S. (2016a). Experimental and numerical study on flexural behavior of ultra-high-performance fiber-reinforced concrete beams with low reinforcement ratios. *Canadian Journal of Civil Engineering*, 44(1):18–28.

Yoo, D. Y., Kang, S. T., and Yoon, Y. S. (2016b). Enhancing the flexural performance of ultra-high-performance concrete using long steel fibers. *Composite Structures*, 147:220–230.

Yoo, D. Y. and Yoon, Y. S. (2015). Structural performance of ultra-high-performance concrete beams with different steel fibers. *Engineering Structures*, 102:409–423.

Yoo, D. Y. and Yoon, Y. S. (2016). A Review on Structural Behavior, Design, and Application of Ultra-High-Performance Fiber-Reinforced Concrete. *International Journal of Concrete Structures and Materials*, 10(2):125–142.